The Dissertation Committee for Sei Young Lee certifies that this is the approved version of the following dissertation:

SIZE AND SHAPE EFFECTS FOR THE NANO/MICRO PARTICLE DYNAMICS IN THE MICROCIRCULATION

Committee:

Mauro Ferrari, Supervisor

Robert Moser, Co-Supervisor

Paolo Decuzzi

Shaochen Chen

Carlos Hidrovo

SIZE AND SHAPE EFFECTS FOR THE NANO/MICRO PARTICLE DYNAMICS IN THE MICROCIRCULATION

by

Sei Young Lee B.S.; M.S.

Dissertation

Presented to the Faculty of the Graduate School of

The University of Texas at Austin

in Partial Fulfillment

of the Requirements

for the Degree of

Doctor of Philosophy

The University of Texas at Austin

August 2010

Dedication

To my family

Acknowledgements

I would like to express my sincere gratitude to my advisor, Dr. Mauro Ferrari for his vision, encouragement, comments, and support. I also would like to thank to Dr. Robert Moser for his guidance and support as a co-supervisor. Without his effort for me, it is not possible to finish all this work. I would like to thank to Dr. Paolo Decuzzi, for his invaluable guidance, comment, support and contribution to this work. I would like to thank to Dr. Shaochen Chen and Dr. Carlos Hidrovo for their comments as committee member. I am very grateful to having worked with nanomedicine group, especially Tong Sun, Jason Sakamoto and all group members, for their support and the wonderful working environment. I would also like to recognize my former mentor Dr. Hyung Hee Cho at Yonsei University who inspired, guided and led me to this interesting field. I sincerely thank my parents for believing me and supporting my pursuit. Last but not the least, I would like thank to my wife, Minyoung Shin, who believes in me, encourages me, supports my pursuit and makes this dissertation possible. I cannot express my appreciation to Minyoung with any words.

Sei Young Lee

University of Texas at Austin

Austin, TX

SIZE AND SHAPE EFFECTS FOR THE NANO/MICRO PARTICLE DYNAMICS IN THE MICROCIRCULATOIN

Publication No._____

Sei Young Lee, PhD

The University of Texas at Austin, 2010

Supervisor: Mauro Ferrari

Co-supervisor: Robert Moser

The nano/micro particles have been widely used as a carrier of therapeutic and contrast imaging agents. The nano/micro particles have many advantages, such as, specificity, controlled release, multifunctionality and engineerability. By tuning the chemical, physical and geometrical properties, the efficacy of delivery of nano/micro particle can be improved. In this study, by analyzing the effect of physical and geometrical properties of particle, such as, size, shape, material property and flow condition, the optimal condition for particle delivery will be explored.

The objectives of this study are (1) to develop predictive mathematical models and (2) experimental models for particle margination and adhesion, and (3) to find optimal particle geometry in terms of size and shape to enhance the efficiency of its delivery. The effect of particle size expressed in terms of Stokes number (St_a) and shape, namely, spherical, ellipsoidal, hemispherical, discoidal and cylindrical particle on the

particle trajectory is investigated. For discoidal and cylindrical particles, the effect of aspect ratio is also considered.

To calculate particle trajectory in the linear shear flow near the substrate, Newton's law of motion is decomposed into hydrodynamic drag and resistance induced by particle motion. The drag and resistance is estimated through finite volume formulation using Fluent v6.3. Particle behavior in the linear shear flow does strongly depend on Stokes number St_a. Spherical particle is transported following the streamline in the absence of external body force. However, non-spherical particles could across the streamline and marginate to the substrate. For non-spherical particles, the optimal St_a in terms of particle margination is observed; $St_a \approx 20$ for ellipsoidal, hemispherical and discoidal particle; $St_a \approx 10$ for cylindrical particle. For discoidal particle with $\gamma_d=0.2$ shows fastest margination to the substrate. The effect of gravitational force is also considered with respect to the fluid direction. When the gravitational force is applied, mostly, gravitational force plays a dominant role for particle margination. However, using small particle aspect ratio ($\gamma_d=0.2$ and 0.33), spontaneous drift induced by particle-fluid-substrate interaction could overcome gravitational effect in some cases ($St_a=10$, $G=0.1$).

In addition the adhesion characteristic of spherical particle has been studied using *in vitro* micro fluidic chamber system with different particle size and flow condition. The experimental results are compared to the mathematical model developed by Decuzzi and Ferrari (Decuzzi and Ferrari, 2006) and *in vivo* test (Decuzzi et al., 2010). The optimal particle size for $S=75$ and 90 is found to be 4-5μm through the *in vitro* non-specific interaction of spherical particle on the biological substrate. The suggested mathematical model has proven to be valid for current experimental condition. At the end, the mathematical model, *in vitro* flow chamber results and *in vivo* test have been compared and the scaling law for particle adhesion on the vessel wall has been confirmed.

Table of Contents

List of Tables

List of Figures

Chapter 1: Introduction

1.1 Rational design of micro/nano particle

According to the Center for Disease Control and Prevention (CDC), the leading causes of death in the United States are heart disease (about 0.61 million), cancer (about 0.56 million)and stroke (about 0.14 million) in 2006 (Heron, 2010). Also, according to the American Cancer Society (ACS), in the United States, over 1.5 million new cancer cases are expected in 2010 and about 0.57 million are expected to die of cancer (American cancer society, 2010). Even though cardiovascular disease and cancer are the most frequent causes of death, there is no standardized treatment method. Therefore, it is required to find effective treatment options.

The most challenging obstacle in treating cardiovascular disease is that it is extremely difficult to localize the therapeutic or imaging agents to the targeted vasculature. In addition, in case of cancer, due to the existence of over 100 different variations of cancer, it is hard to find a standard method to treat all these kinds of cancer. Therefore, the most fundamental and important aspect of cardiovascular disease and cancer treatment is the successful delivery of the drug molecule and/or drug carrier loading therapeutic and imaging agent to the targeted vasculature. Recently, scientists have explored the possibility of using the particulate drug delivery system as the primary carrier in treating cardiovascular disease or cancer. Furthermore, diverse particles, with different size, shapes and surface properties have been developed for the effective delivery of drug molecules and/or imaging agent loaded in the particulate system.

In recent decades, the development of nanotechnology, especially, nano-/micro sized particle fabrication techniques enabled the development of various new particles including, but not limited to the liposome, polymeric particles (Champion and Mitragotri,

2006; Rolland et al., 2005; Charoenphol et al., 2010), gold nanoparticle (Duncan, 2003; Hirsch et al., 2003), silicon based meso-porous particles (Tasciotti et al., 2008; Serda et al., 2009), carbon nanotube (CNT) based carrier (Li et al., 2010; Mahmood et al., 2009), and adeno-associated virus phage (AAVP) (Allen et al., 2002; Hajitou et al., 2006; Levy-Nissenbaum et al., 2008). These newly developed particles vary in size (from a few tens of nanometers to a few microns), shapes (from sphere, hemi-sphere, disc, cylinder, conical, rod to even arbitrary shape), and surface functionalizations (ranging from wide range of electrostatic charge, conjugation of antibody, ligand, peptide to polymeric functionalization). Therefore, new experiments with these different mechanical, electrostatic, biological and physiological properties enabled the creation of unprecedented number of possible combination variations of nano/micro particle types for specific purposes.

The nano/micro particle carrier as therapeutic and/or imaging agent can be subdivided into three categories (Godin et al., 2010). The first generation of nano/micro carrier delivers the nano/micro particles to the targeted region using the passive approach: Liposomes, FDA approved drug carrier, deliver the particle mainly through the enhanced permeation retention (EPR) effect (Hashizume et al., 2000); EPR, property by which certain sizes of molecules, typically liposomes or macromolecular drugs, tends to accumulate in tumor tissues much more than they do in normal tissues. Furthermore, to enhance the circulation time and prevent any unnecessary absorption into the reticulo endothelial system (RES), the surface of particle carriers can be treated with polyethylene glycol (PEG).

The second generation nano/micro drug carrier has additional function to the first generation, with enhanced searching ability of the targeted region. The conjugation of the antibody to the first generation particle will increase the possibility of localizing the drug

carrier onto the diseased site. However, further studies are required to guarantee optimal binding affinity. If binding affinity is too high, that is, too high concentration of antibody on the particle surface, it creates a favorable environment for the localization and the delivery to the targeted cell, such as, tumor vasculature and hematological malignancies. However, this process is less desired from the aspect of penetration and diffusion into the extracellular matrix since excessive binding between the particle and the surface of the cell may prevent particles from internalizing. On the other hand, if the surface density of the antibody is too low, it becomes difficult for the particle to localize on the desired site.

Finally, the third generation of drug carrier is the multi functional nano/micro particle. These particles not only deliver the drug or imaging agent, but also have additional functionalities; ability to search the target, enhance the circulation time, release carried molecule in time-controlled way and combine any of the listed functions in multiple ways. While the third generation particles are most desired, the innate complexity resulting from its multi-functionality would require additional new systematic approaches to prescribe these myriad of possible functional combinations.

It is difficult to find the optimum strategy in targeting the inflamed site and designing a particle for this specific purpose. As discussed earlier, we must not forget the existence of large variations of cardiovascular diseases including cancer, increasing the diversity of the possible targeted cells and targeted molecules. To this end, various theoretical and experimental methods have been developed to design the optimal particle property in terms of size, shape and surface property. First, the theoretical prediction of the probability of particle adhesion, based on the kinetics of reaction of particle with substrate, has been analyzed by earlier studies (Hammer and Lauffenburger, 1987, Cozen-Roberts et al., 1990, Piper et al., 1998, Decuzzi and Ferrari, 2006). These approaches in its analysis incorporated the ligand-receptor interaction as the primary

adhesion mechanism and hydrodynamic interaction as the detachment mechanism. As a more realistic approach, several groups have tried to model the transport of nano/micro sized particle with authentic vasculature (Bazilevs et al., 2006, Bazilevs et al., 2008, Calo et al., 2008). In solving advection-diffusion-reaction problem for particle delivery, the most important aspect is the boundary condition of the reaction wall. Although it is possible to deduce several variables from the theoretical predictions of the particle mentioned above, it is still insignificant to predict the characteristics of particle adhesion, requiring further studies in the proper boundary condition of the reaction boundary. Another challenge in solving advection-diffusion-reaction problem in authentic vasculature is its complex geometry. Due to the complexity of the vascular network surrounding the tumor, it is almost impossible to employ an analytical solution. Instead, numerical studies based on the 'Finite Volume Method,' and the 'Finite Element Method' have been employed in trying to solve the problem. These approaches can provide valuable insight into the particle adhesion behavior in the flow as well as great guidelines in designing possible experimental directions, alleviating the burden of time constraints from experimenting with the sheer volume of possible cases (Ferrari, 2008).

However, theoretical approach has apparent limitations; without the help of experiment, it is simply not feasible to determine the characteristics of near infinite number of possible variables. Many research groups have conducted numerous experiments to characterize the particle adhesion and related variables. Among the many system approaches employed, the most commonly incorporated system in characterizing the particle of cell attachment and/or detachment is the □-fluidic chamber, which is relatively simple to operate and gives great insight in terms of the interaction of particle or cell with the substrate. For example, Decuzzi and colleagues (Gentile et al., 2008, Decuzzi et al., 2007) have rigorously investigated the effect of shape on particle adhesion

of fluorescent microsphere to the endothelial cell layer grown on the glass substrate under flow. The Eniola-Adefeso group (Charoenphol et al., 2010) studied the effects of hemodynamics, channel size and particle size on the specific adhesion in the same system. Furthermore, other researchers have also investigated the effect of size in specific interaction with relatively large sized microsphere coated with recombinant P-Selectin glycoprotein ligand-1 (Shinde Patil et al., 2001). In addition to these experiments focusing on adhesion characteristics, numerous techniques have been newly developed and employed to measure the size and shape of the particle, density, porosity, surface charge, solubility and stability (Godin et al, 2010, Mitragotri and Lahann, 2009).

The ultimate purpose of the development and application of mathematical prediction and experimental approaches described above is to design optimal physical and physiological properties of the particle. Current advancements in nano technology have enabled the development of more complex and multifunctional drug carriers, such as, third generation particles as well as the characterization of complex particle properties. Therefore, integrating the benefits from these technological developments to the newly devised experimental methods discussed in this paper can not only provide feasible opportunities in the designing of optimal geometrical and physiological characteristics but also maximizing the delivery efficiency of the particle to the targeted cell.

1.2 Multi-stage drug carrier over biological and physiological barriers

A multitude of barriers along the circulatory system prevent therapeutic molecules, tracers used in imaging and nano-sized particulate (NP) systems from reaching their target in the desired mass fractions, thus reducing the therapeutic and

imaging efficacy. These are barriers of different nature. Physiological barriers as (i) the spatially and temporally heterogeneous blood flow in tumors (Jain, 2001) due to hyper-permeable blood vessels with fenestration (Hashizume et al, 2000) and to a lack of a functional lymphatic system; (ii) the increased interstitial fluid pressure that may reduce transvascular and interstitial transport of free molecules within the extracellular matrix (Decuzzi et al, 2006); (iii) the highly intricate extracellular matrix (ECM) constituting an additional barrier to the delivery and transport of drugs (Netti et al, 2000). Biological barriers as (iv) the reticular endothelial system, constituted by phagocytes, specialized cells lining the liver, spleen, bone marrow, and lymphatic tissue, which recognizes external molecules and remove them from the circulation (Aberts et al, 2002); (v) the insufficient expression of receptors on the membrane of the target cells, making more unlikely the specific recognition of the target cell by the imaging tracers or the therapeutic molecules (Aberts et al, 2002). There is a dramatic need to increase the mass fractions of therapeutic agents and imaging tracers at the biological target in order to improve the effectiveness of the therapy and the spatial resolution of the imaging techniques. The use of NP system for the early detection and delivery of imaging and therapeutic agent has been recognized as a powerful and promising tool that can change dramatically everyday clinical practice (Ferrari 2005, LaVan et al. 2003).

The power of intravascularly injectable NPs over free molecules administration lies in their multifunctionality and engineerability. The use of NP delivery affords substantial advantages including (i) the specific biomolecular targeting through one or more conjugated antibodies or other recognition molecules (ligands) that increases selectivity and reduces side effects; (ii) ability to carry one or more therapeutic agents that improves the therapeutic efficacy and allows for a patient dedicated therapy and can lead to develop new therapies; (iii) increase of the number of drug molecules that can be

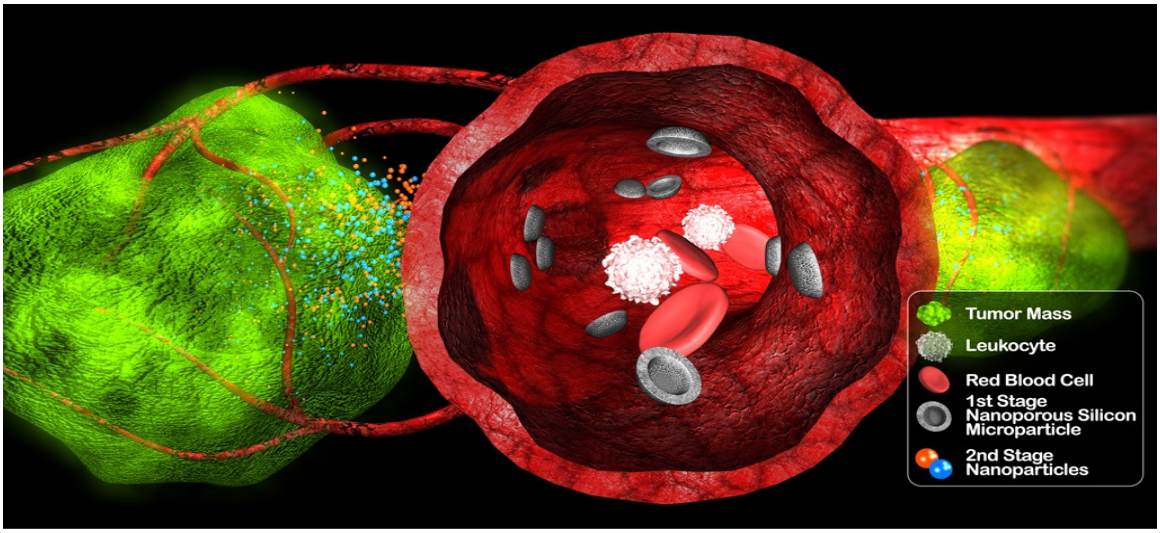

Fig. 1: Multi-Stage System for Targeted Drug Delivery (from Sakamoto et al., 2007)

released at the target site; (iv) signal amplification for imaging through co-encapsulated contrast agents that allows to follow the cancer lesion during its evolution, (iv) tuning of the physico-chemical and geometrical properties of the NPs that favors avoidance of biological and physiological barriers and improve the recognition of the target cells or microenvironments (Sakamoto et al., 2007). Based on this, differently from freely administrated molecules, the NPs can be designed as a function of the target to improve selectively, therapy effectiveness and signal strength.

Over the past 20 years or so, a large number of particulate systems with different physico-chemical properties have been synthesized and fabricated. Recently the notion of multi-stage delivery systems has been introduced and developed within the Nanomedicine group, lead by Dr. Ferrari (Sakamoto et al., 2007; Tasciotti et al., 2008). This is associated with the idea that a systemic delivery system for intervascular injection must be capable of performing multiple sequential tasks, including the ability to interact successfully with biophysical and biological barriers. The strategy is based on vectors (Stage 1 NanoParticles or S1NP) that carry one or more types of Stage 2 NanoParticles

(S2NP) which themselves can carry active agents, or higher-stage particles. The S1NP are rationally designed to provide optimal transport of the pay-load across the vascular three to the target vasculature, while avoiding enzymatic degradation and RES uptake. Once they reach the vasculature, they could release agents that enhance extravasation, together with active principles or carrier nanoparticles that have the ability to transport the S2NP to target cells or subcellular structures (Fig.1).

1.3 Fabrication of particle with different size and shape

The progress of nano/micro technology enables to development various size and shape of nano/micro particle. One of the major advantages in using the particle as drug and/or imaging agent carrier is the engineerability, that is to say, it is possible to fabricate the particle whatever particle size and shape we want to make even though there are some technical limitation. For example, Mitragotri group (Champion et al., 2007) made polymeric micro-nanoparticles of complex shapes by stretching polystyrene microsphere. They made more than 20 different shapes with characteristic size ranging from 60 nm to 30 μm. DeSimone group (Rollando et al, 2005 and Gratton et al., 2008) also fabricated various shape of particle by PRINT (Particle Replication In Non-wetting Templates) technique with wide range in size (sub-200 nm to complex micron scale). More recently, Ferrari group (Tasciotti et al., 2008) proposed porous silicon particle with quasi hemispherical shape. Different from solid silicon particle, porous silicon particle is biodegradable and biocompatible. Thus, porous silica particle can be easily conjugated with any biological and chemical molecule to load therapeutic molecule and to enhance the specific recognition of target cell. These features make porous silica particle to be one

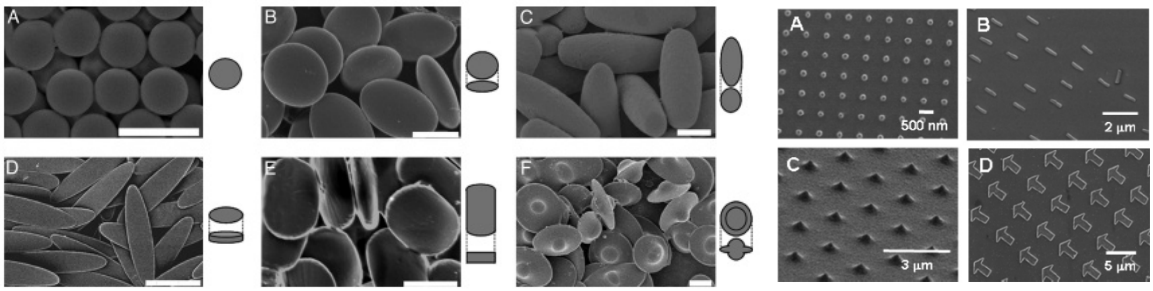

(a) (b)

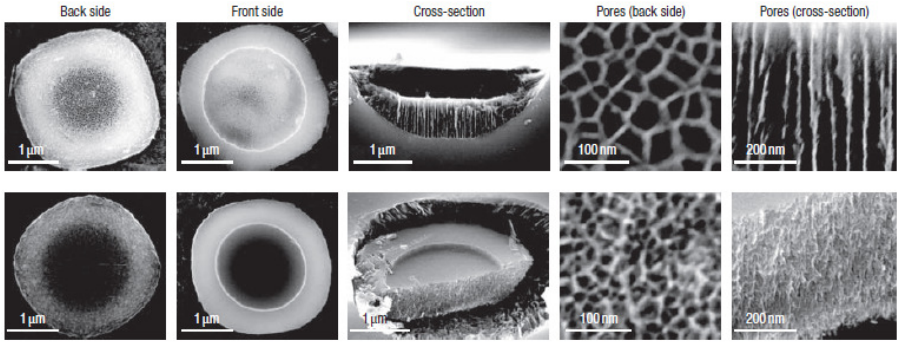

(c)

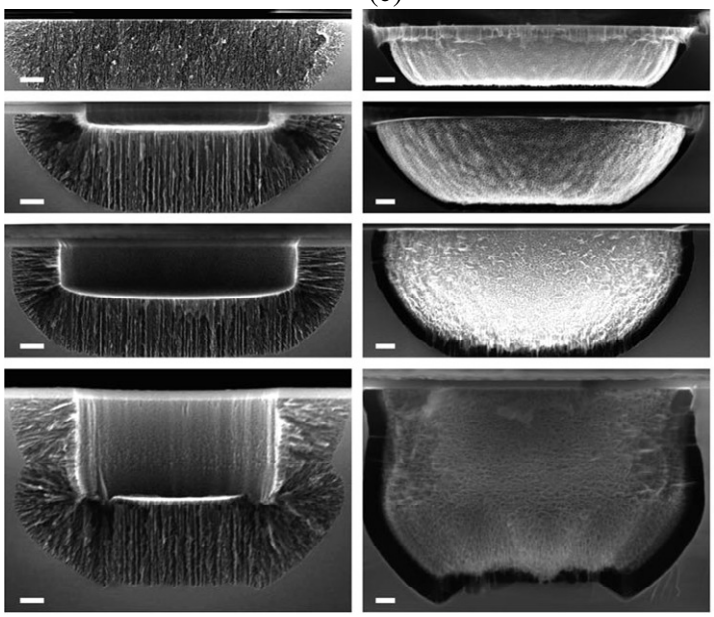

(d)

Fig. 2: Non-spherical particles fabricated from different groups; (a) Mitragotri group (from Champion et al., 2006), (b) DeSimone group (from Rolland et al., 2005), (c) Ferrari group (from Tasciotti et al., 2008, Cohen et al., 2003) and (d) (from Chiappini et al., 2010)

of the strongest candidates for the next generation particle material for drug delivery. Additionally, by controlling physical characteristics through electrochemical etching of patterned silicon trenches, Ferrari group also fabricated different shape of particle from tubular to discoidal to hemispherical (Chiappini et al., 2010); (1) flat-disk (2) discodial particle (3) hemispherical particle (4) tubular particle in Fig. 2(d).

1.4 Motivation and scope of the study

This study focuses on the development of mathematical tools and in-vitro testing assays for developing S1NP targeted to the diseased vasculature. Assuming linear shear flow, which is valid in the proximity of vessel wall, particle trajectory with different shape and flow condition will be investigated using analytic and numerical approach. The effect of external body force will also be considered. The adhesion of particulate system will be predicted by mathematical modeling. The *in-vitro* experiments will be employed to refine and validate the predictive mathematical results. The results in this study would lead to identify optimal geometry of particulate system to enhance delivery efficiency of particulate system.

Chapter 2: Effect of size and shape on margination dynamics

2.1 Introduction

The particle behavior is one of the most interesting topics not only for biological application but also for diverse engineering problems, such as, air pollution, combustion, air conditioning, ash deposition in gas turbine, and etc. However, one of the most interested areas of particle deposition is the biomedical application, regulating the delivery of the drug to the specific targets. Particulate system injected in the blood stream experiences external force generated by hydrodynamic interaction. The drag force on the freely moving spherical particle in viscous flow with very low Reynolds, commonly referred as the Stokes flow, can be estimated by employing the Navier-Stokes equation ($D=6\pi\mu VR$, where, D is drag on the sphere, is viscosity, V is centerline velocity and R is particle radius). In the microcirculation, it is very important to evaluate the particle-wall interaction and hydrodynamic forces on the particle since the ultimate objective of using particulate system as a molecule carrier is to deliver the particle to the wall or endothelium. When the particle moves to the proximity of the wall, the viscous interaction between the particles and the wall greatly influence the particle motion. This interaction in the linear shear flow between the wall and particle motion was originally explained through the asymptotic approach in estimating the drag, lift and torque of the particle (Goldman et al., 1967[a,b]).

The most interesting phenomenon of particle behavior in biomedical application is the Segre-Silberberg effect. In general, a neutrally buoyant particle in a long pipe undergoes a radial migration for finite Reynolds number flows, staying within 0.6R of the pipe. In 1961, Segre and Silberberg performed various experiments on the flow of neutrally buoyant dilute spherical particle in a long circular duct (Segre and Silberberg,

1961). To explain this phenomenon, arbitrary Lagrangian–Eulerian moving mesh technique (ALE) has been developed to solve the particle motion in the Poiseuille flow (Yang et al., 2005, Joseph and Ocando, 2002). According to this study, slip velocity and slip angular velocity discrepancy can be employed to explain any sign changes in the lift force on the sphere to a certain extent. Recently, the Segre-Silberberg effect has been experimentally verified in wide range of Reynolds number (Mattas et al., 2004), showing the location of three-dimensional particles as well as visualizing the structure of the Segre-Silberberg annulus using the digital holographic technique (Choi and Lee, 2010). Furthermore, these findings have shown that microcirculation can be assumed as a type of circular pipe flow with small diameter (few μm ~ few mm). In addition, it is safe to conclude that in general, the target for the drug carrier is the inflamed endothelial cell, assumed to be allocated in the circular capillary. Therefore, it is not easy for the spherical particle to reach the side wall (endothelium) due to the Segre-Silberberg effect.

Non-spherical particle behaves differently from the spherical particle: Particle rotates from the shear flow and the combined effect of the rotation, where the particle non-sphericity creates the unbalanced lift force. The drag, lift and torque on a non-spherical particle was estimated through the works of Jeffrey (Jeffrey, 1922) where he demonstrated the free movement of particles in the linear shear flow. In addition, Gavze and Shapiro (Gavze and Shapiro, 1997) employed the boundary integral method to prolate ellipsoid particles in linear shear flow to estimate the forces on the non-spherical particles near the wall, which can in turn be used to estimate the hydrodynamic force on the non-spherical particle. The unbalance of lift force on the front and rear, due to the non-spherical shape of particle, induces particle margination; drift across the streamline (Gavze and Shapiro, 1998). In a capillary flow, the utilization of particle-wall interaction can be employed to overcome the limitations of particle separation from the walls caused

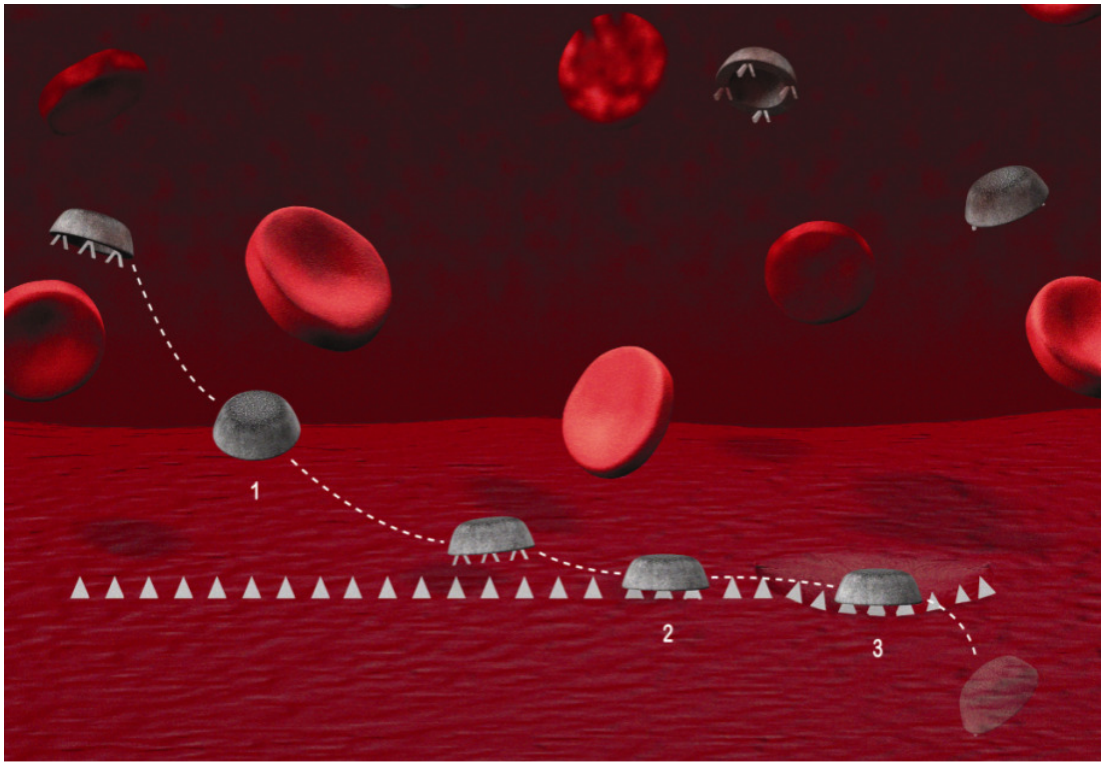

Fig. 3: Three steps particle delivery to target cite (from Decuzzi et al., 2008)

by the Segre-Silberberg effect. The trajectory of particle in the linear shear flow can be easily calculated by solving Newton's law of motion with drag, lift and torque on the non-spherical particle, estimated numerically. However, only ellipsoidal trajectory has been revealed and there is little existing investigation on the trajectory of single particle with different shape in the linear shear flow.

The particles injected into the blood stream experiences three steps of delivery; (1) margination, (2) firm adhesion and (3) internalization (Fig. 3). Definitely, it is very important not only to study interaction between the particle and cell, but also to study particle margination characteristics in the flow. In this chapter, as explained briefly in chapter 1.3, the effect of non-spherical shape on particle-fluid and particle-wall interaction will be discussed. Also, the optimal shape in terms of margination will be explored

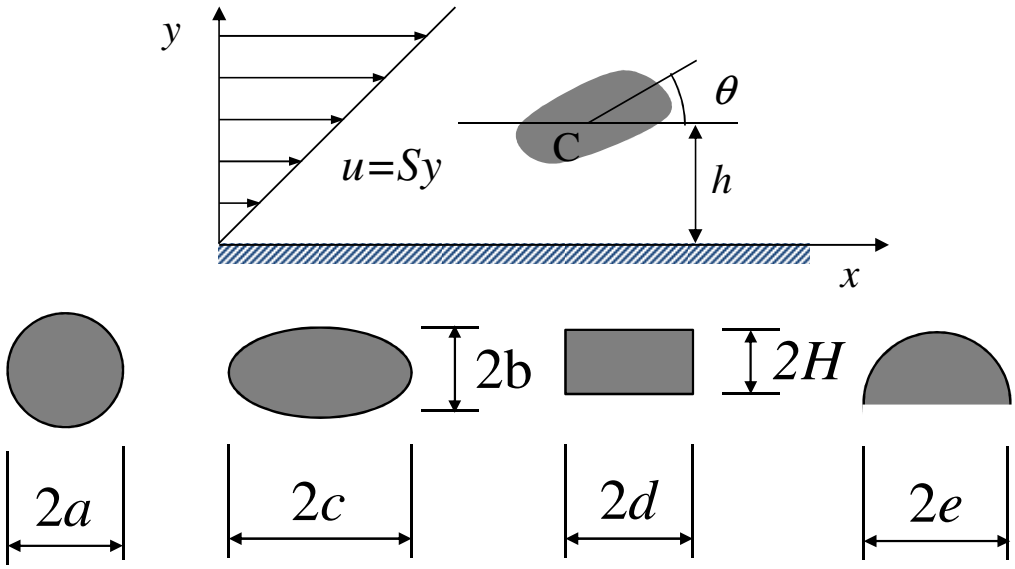

Fig. 4: Schematic representation of an arbitrarily shaped particle in a linear laminar flow in wall proximity. Four particles shapes are considered: spherical, hemispherical, ellipsoidal, discoidal and cylindrical particles ($0.2 \leq \gamma < 2.00$).

2.2 Mathematical modeling of particle in the linear shear flow

The geometry of the problem is presented in Fig 4, where an arbitrary shaped particle is immersed within a linear laminar flow in a semi-infinite three-dimensional region bounded by an infinite flat plane at $y=0$. The flow is in the x direction with a wall shear rate S, the separation distance of the particle centroid from the wall is h in the y direction normal to the flow, and θ is the particle orientation with respect to x. Four different particle shapes are considered, namely a spherical bead with radius a; an ellipsoidal particle with minor and major axis semi-length b and c, respectively, and aspect ratio $\gamma_e=b/c$; a discoidal particle with radius $2d$, height $2H$, and aspect ratio $\gamma_d=H/d$; and a hemispherical particle with radius e. The fluid motion has to satisfy the conservation of mass and conservation of momentum

$$\nabla \cdot \boldsymbol{u} = 0 \tag{1}$$

$$\rho_f \left(\frac{\partial \boldsymbol{u}}{\partial t} + (\boldsymbol{u} \cdot \nabla)\boldsymbol{u} \right) = -\nabla p + \mu \nabla^2 \boldsymbol{u} \tag{2}$$

where u is the fluid velocity vector, ρ_f is the fluid density (aqueous solution 10^3 kg/m^3; air 1 kg/m^3) and μ is the fluid dynamic viscosity (aqueous solution ~10^{-3} Pa sec; air ~10^{-5} kg/m3), and p is the dynamic pressure in the fluid. The particle has to satisfy Newton's law of motion which for a translational motion is described by

$$m_p \frac{d\boldsymbol{U}}{dt} = \boldsymbol{F} \quad \text{and} \quad \frac{d\boldsymbol{X}}{dt} = \boldsymbol{U} \tag{3}$$

being

$$\boldsymbol{F} = \int_{\partial S} \sigma \cdot \boldsymbol{n} dS + (m - m_f)\boldsymbol{g}$$
$$\sigma = -p\boldsymbol{I} + \mu \left[\nabla \boldsymbol{u} + (\nabla \boldsymbol{u})^T \right] \text{ with the unit tensor } \boldsymbol{I} = \begin{bmatrix} 1 & 0 & 0 \\ 0 & 1 & 0 \\ 0 & 0 & 1 \end{bmatrix} \tag{4}$$

where $\boldsymbol{U}$ is the particle velocity vector, $\boldsymbol{X}$ is the position vector of the particle centroid, $\boldsymbol{F}$ is the sum of the hydrodynamic force exerted by the fluid on the particle surface ∂S and the buoyancy force. Also, $\boldsymbol{\sigma}$ is the hydrodynamic stress tensor, $\boldsymbol{n}$ is the unit normal to the particle surface and $\boldsymbol{g}$ is the gravitational acceleration, with m_p the particle mass and m_f the displaced fluid mass. In addition, the particle rotational motion is described by

$$\frac{d(\boldsymbol{L\Omega})}{dt} = \boldsymbol{T} \quad \text{and} \quad \frac{d\vartheta}{dt} = \boldsymbol{\Omega} \tag{5}$$

with

$$\boldsymbol{T} = \int_{\partial S} (\boldsymbol{x} - \boldsymbol{X}) \times (\sigma \cdot \boldsymbol{n}) dS \tag{6}$$

where $\boldsymbol{L}$ is the moment of inertia tensor, $\boldsymbol{\Omega}$ is the angular velocity of the particle, $\boldsymbol{T}$ is the hydrodynamic moment vector, with $\boldsymbol{x}$ the position vector of a point over the particle surface. The problem is closed by imposing the boundary conditions for the fluid as

$$\begin{aligned} \boldsymbol{u} &= \boldsymbol{0} && \text{on the wall (y=0)} \\ \boldsymbol{u} &= Sy\boldsymbol{e}_x && \text{away from the particle in the flow direction} \\ \boldsymbol{u} &= \boldsymbol{U} + \Omega \times (\boldsymbol{x} - \boldsymbol{X}) && \boldsymbol{e}_x = \boldsymbol{x}/|\boldsymbol{x}| \text{ on the particle surface } \partial S \end{aligned} \tag{7}$$

By solving the boundary value problem (1)-(7), the trajectory of the particle within the flow domain can be analyzed as a function of the flow conditions (wall shear rate S) and of the particle properties (size, shape and density relative to fluid); and initial conditions (separation distance h_o, orientations θ_o, and velocities $U_x^o; U_y^o; \Omega$).

The above general formulation can be simplified when the particle is moving within a laminar flow with sufficiently small Reynolds numbers ($\mathrm{Re}_p \leq 0.1$, See Appendix A). Typically, the flow in the blood microcirculation, from arterioles down to small capillaries and venules; and within the small alveoli in the pulmonary airways is characterized by even smaller Reynolds numbers. Under this assumption the particle motion and fluid flow can be decoupled, so that the original formulation by Gavze and Shapiro (Gavze and Shapiro, 1998) is here extended for a particle with an arbitrary shape to give the relation

Table 1. Parameters P and rotational inertia L for the four shapes analyzed, for a fixed particle volume ($L_s = 2ma^2/5$: rotational inertia for a spherical particle).

	γ	L/L_s	P
Sphere	–	1	2/5
Ellipse	$\gamma_e = \frac{b}{c}$	$\frac{(1+\gamma_e^{\,2})}{2\gamma_e^{\,4/3}}$	$\frac{(1+\gamma_e^{\,2})}{5\gamma_e^{\,4/3}}$
Disc	$\gamma_d = \frac{H}{d}$	$\frac{5(3+4\gamma_d^{\,2})}{24(2\gamma_d)^{2/3}}$	$\frac{(3+4\gamma_d^{\,2})}{12(2\gamma_d)^{2/3}}$
Hemisphere	–	0.408	0.163

$$\frac{4\pi}{3} St_a \frac{d}{dt}\begin{bmatrix} U_x \\ U_y \\ P\Omega \end{bmatrix} = \boldsymbol{D} + \boldsymbol{G} - \boldsymbol{R}\begin{bmatrix} U_x \\ U_y \\ \Omega \end{bmatrix} \qquad \text{and} \qquad \frac{d}{dt}\begin{bmatrix} x \\ y \\ \theta \end{bmatrix} = \begin{bmatrix} U_x \\ U_y \\ \Omega \end{bmatrix} \tag{8}$$

where St_a is the Stokes number ($St_a = \rho_p a^2 S/\mu$) for an equivalent radius a and density ρ_p; U_x and U_y and Ω are the translational and angular velocities of the particles. The equivalent radius is defined as the radius of spherical particle which has same volume of non-spherical particle considered. The quantity $\boldsymbol{D}$ and $\boldsymbol{R}$ are the normalized drag vector and resistance matrix given respectively by

$$\boldsymbol{D} = \frac{1}{\mu S a^3}\begin{bmatrix} F_x a \\ F_y a \\ T_z \end{bmatrix}; \quad \boldsymbol{R} = \frac{1}{\mu a^3}\begin{bmatrix} \Phi_{xx}a^2 & \Phi_{xy}a^2 & \Phi_{xz}a \\ \Phi_{yx}a^2 & \Phi_{yy}a^2 & \Phi_{yz}a \\ \Phi_{zx}a & \Phi_{zy}a & \Phi_{zz} \end{bmatrix} \tag{9}$$

and G is the normalized buoyancy force whose modulus is given as $G = (\rho_p - \rho_f)ga/(\mu S)$. In Eq. (8), the coefficient P depends only on the shape of the

particle, as from Table.1. The *i*-th component of the drag vector, D_i, is the normalized force experienced in the *i* direction by a fixed particle immersed within a linear laminar flow; whereas the *ij-th* component of the resistance tensor, R_{ij}, is the normalized force experienced in the *i* direction by a particle moving with unit velocity in the *j* direction within an otherwise quiescent fluid. Notice that the resistance tensor is symmetric (Happel and Brenner, 1983).

As the particle moves, both the drag vector $\boldsymbol{D}$ and the resistance tensor $\boldsymbol{R}$ vary as they depend on the separation distance *h* and particle orientation, θ. For a simple geometry as the sphere, $\boldsymbol{D}$ and $\boldsymbol{R}$ can be analytically determined, as shown in Goldman et al. (Goldman et al, 1968[a,b]), and take the form

$$D_x = \frac{F_x a}{\mu S a^3} = 6\pi F_x^* \qquad \text{and} \qquad D_z = \frac{T_z}{\mu S a^3} = 8\pi T_z^*$$

$$R_{xx} = \frac{\Phi_{xx}}{a} = 6\pi\mu S a R_{xx}^*; \qquad R_{xz} = \frac{\Phi_{xz} a}{a^3} = 6\pi\mu S R_{xz}^*; \qquad R_{zz} = \frac{\Phi_{zz}}{a^3} = 8\pi\mu S R_{zz}^* \tag{10}$$

where the star terms are constants depending on the separation distance *h* of the sphere center from the wall. For more complex geometries, $\boldsymbol{D}$ and $\boldsymbol{R}$ can be determined by using any computational fluid mechanics software and following the above definitions. In the present case, the commercial fluid flow calculation software FLUENT v6.3 and Gambit v2.1 has been employed calculating D_i and R_{ij} for 4 different separation distances and every 15° with respect to the flow direction. Polynomial fitting is employed to map $\boldsymbol{D}$ and $\boldsymbol{R}$ on the $y\theta$-plane. Once $\boldsymbol{D}$ and $\boldsymbol{R}$ are known, the particle trajectory can be derived by integrating Eq. (8) with proper initial conditions. In the present case a Runge-Kutta scheme has been employed in MatLAB with a self-adjusted time interval that ensures numerical convergence.

2.3 Validation of the numerical results

To validate the numerical estimation of forces and torque on the arbitrarily shaped particle, the results are compare to the previous analytical and numerical results. The present formulation has been shown to reproduce with great accuracy the analytical results by Goldman et al. (Goldman et al, 1968[a,b]) for a spherical bead and the numerical results by Gavze and Shapiro (Gavze and Shapiro, 1998) for an ellipsoidal particle as following.

2.3.1 Grid dependency and convergence of fluid field calculation

In calculating Drag vector and Resistance tensor, Fluent Ver. 6.3 and has been used for simulate flow field around the particle and estimate forces on the particle and Gambit Ver. 2.4 has been used for generate particle and linear shear flow geometry and create mesh and give boundary condition of flow domain. Symmetric wall has been defined at the middle of particle to reduce calculation time, assuming that particle is not moving in z-direction. A tet/hybrid mesh is used to discretize the geometry of the problem. To make more accurate calculation around the particle, grid size has been adjusted. For particle, a grid size is 2.5% of characteristic size of particle (equivalent particle diameter), for example, 1μm spherical particle will have 25nm grid size. Also, to give more grids to the flow domain around the particle, grid grading has been used as double sided successive ratio type with ratio of 0.95, which gives more grids at the center of flow domain.

To calculate drag, lift and torque of the particle (drag vector) in the linear shear flow, user defined function (UDF) has been compiled and the combined force of pressure force and viscous force on the particle surface has been calculated. For the resistance tensor, uniform flow velocity or rotational angular velocity has been applied for all

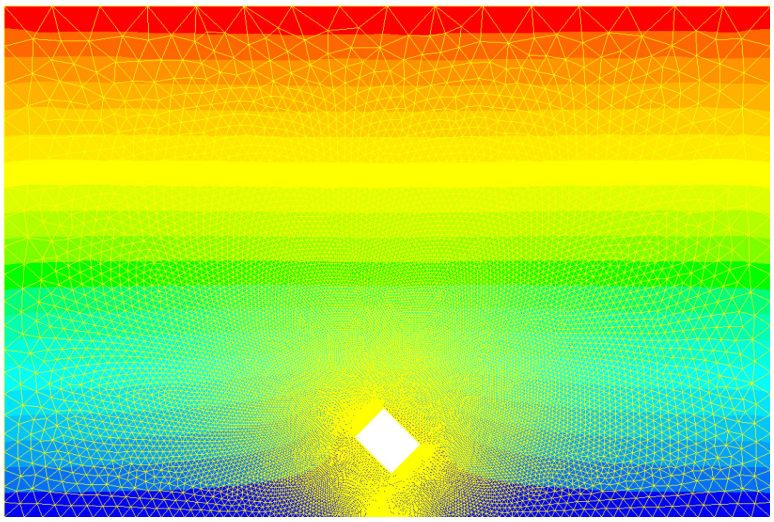

Fig. 5: Grid generation around particle and flow domain

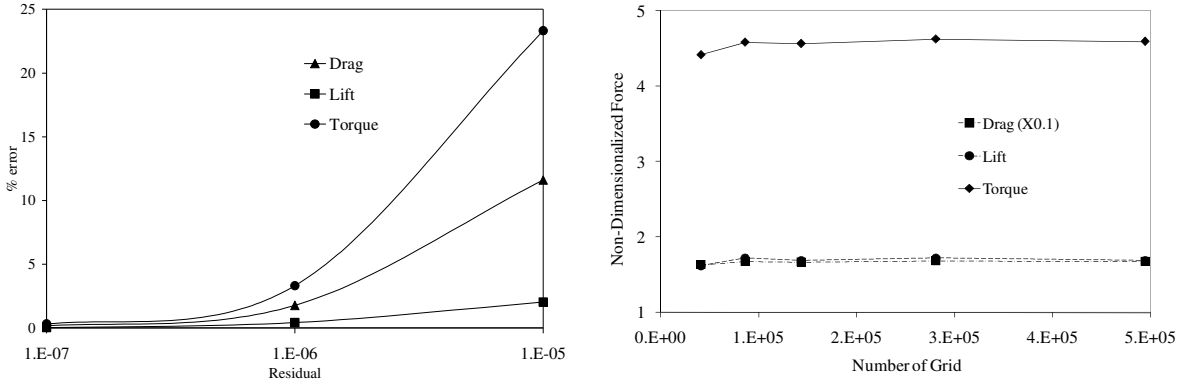

Fig. 6: (a) Percent error of drag, lift and torque with different convergence criteria and (b) non-dimensionalized drag, lift and torque of spherical particle

boundaries except symmetric boundary. Pressure based 3D steady laminar incompressible flow has been assumed for flow field calculation with least square cell based as a gradient option. SIMPLEC for pressure-velocity coupling with relaxation factor of 0.3, 1.0, 1.0 and 0.7 for pressure, density, body force and momentum, respectively as a default has been used. Second order and second order upwind scheme has been used for discretization for pressure and momentum, respectively.

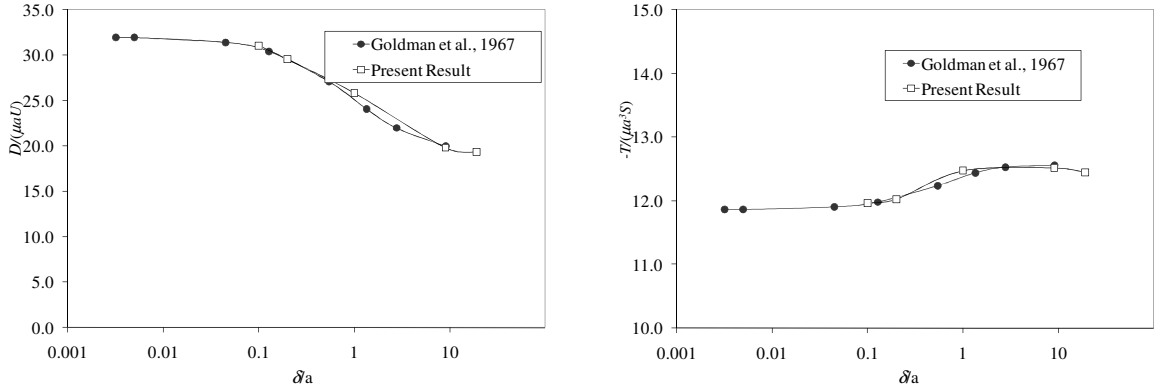

Fig. 7: Comparison of normalized drag force and torque exerted on the spherical particle by hydrodynamic force in the linear shear flow (drag vector) with asymptotic solution by Goldman et al., 1967[a]

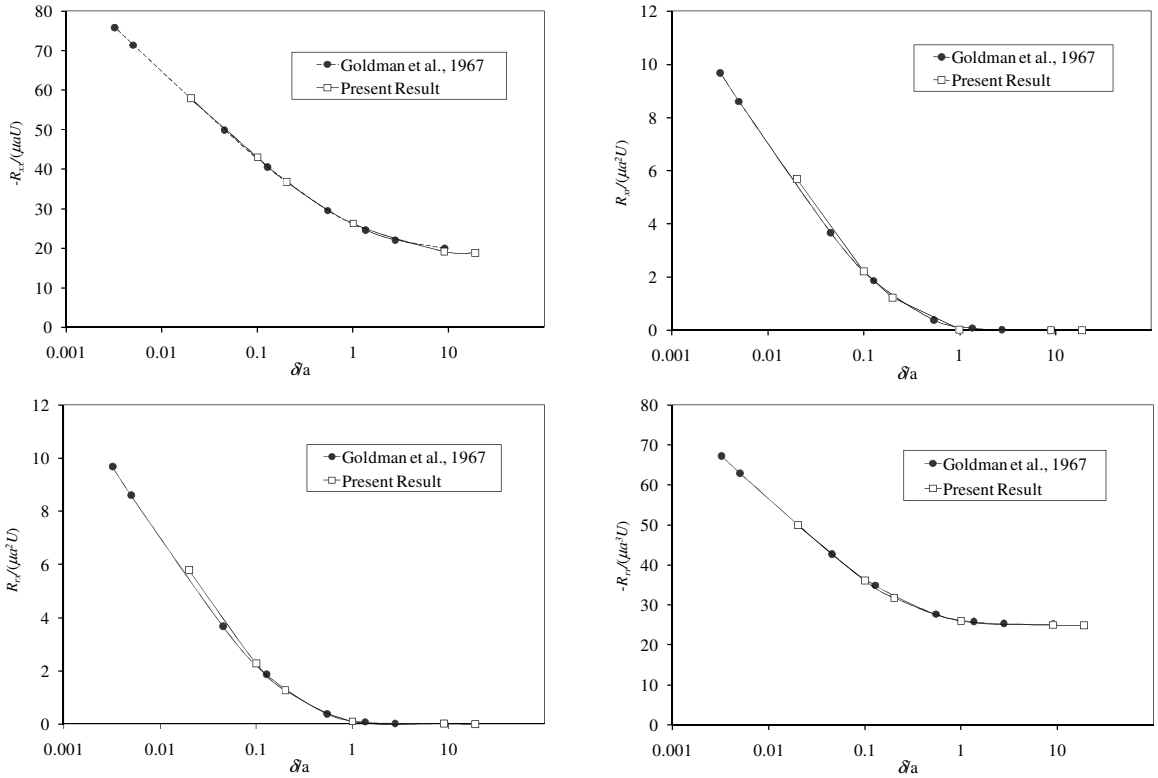

Fig. 8: Comparison of normalized force and torque exerted on the translating and rotating spherical particle (resistance tensor) with asymptotic solution by Goldman et al., 1967[b]

For convergence check, residual of continuity and x, y and z momentum equation has been monitored through calculation. To find out the convergence criteria, drag, lift and torque of spherical particle has been calculated for different residual values (Fig.

6(a)). The error has been estimated for the drag, lift and torque values based on the values calculated based on the residual 10^{-8}. For relatively large residual ($R=10^{-5}$), torque and lift shows very large error (~24% and ~10% error, respectively) but drag shows relatively small error (less than 5%). As decrease the convergence criteria, percentage error is also reduced, namely, with convergence criteria of 10^{-7}, error of all three drag vector components are less than 1%. Based on this, convergence criterion has been chosen to be 10^{-7}.

To check the dependency of grid number, non-dimensionalized drag, lift and torque of spherical particle in the linear shear flow has been compared with different number of grid, ranging approximately from 5×10^4 to 5×10^5. As seen in Fig. 6(b), with number of grid over 10^5, there is no significant difference in terms of normalized drag, lift and torque. Generally, 3×10^5 to 3.5×10^5 grids are used to get rid of grid dependency.

2.3.2 Forces on spherical particle

The forces exerted on the spherical particle by the linear shear flow and by uniform flow have been calculated by Goldman et al. (Goldman et al., 1967[1,2]) using asymptotic approach to solve Stokes flow over the spherical particle near the wall. The forces on the spherical particle by linear shear flow can be defined as drag vector and the forces on the moving sphere can be defined as resistance tensor in this case. Normalized drag vector and resistance tensor over non-dimensional separation distance are plotted in Fig. 7 and 8. Solid circle is coming from the asymptotic solution by Goldman et al. and hollow rectangle is current numerical results. Within the range of interest of separation distance ($0.1<\delta/a<10$), current numerical results are in good agreement with the asymptotic solution by Goldman et al. Small error (less than 0.8%) is shown at $\delta/a\approx1$ in

both cases of drag and torque on the particle caused by the hydrodynamic force in linear shear flow (fig. 7). It is attributed to the number of grid, which is varying according to the separation distance but is still very small. On the other hand, both of calculated and analytically predicted resistance tensor (R_{xx}, R_{xr}, R_{rx} and R_{rr}) are well-matched.

2.3.3 Forces on ellipsoidal particle

Gavze and Shapiro numerically estimated the exerting force on the prolate ellipsoidal particle using boundary element method and subsequently solved trajectory of the particle (Gavze and Shapiro, 1997; 1998). To validate the numerical solution of present result for non-spherical particle, for instance, exerting force on ellipsoidal particle is compared to the previous numerical solution by Gavze and Shapiro, 1997. They proposed correlation formulae for drag vector and resistance tensor component obtained by regression analysis according to the *y*-directional location and angle of ellipsoidal particle. Current results are compared to these approximation formulae at chosen *y*-directional location and particle angle (θ).

Fig. 9 and Fig. 10 shows the comparison between the previous results (Gavze and Shapiro, 1997) and current results of drag vector and resistance tensor for prolate ellipsoidal particle (γ_e=0.5), respectively. In the present result, the drag vector resistance tensor has been estimated for the particle with the semi-minor axis and semi-major axis of particle of b=0.397 μm and c=0.794 μm, respectively, which has same volume of the spherical particle with 1μm in diameter. As shown in the figures, there is relatively small error between the two results. In case of drag vector (Fig. 9), the lift force at h/c=2.5 shows maximum percentage error (about 5.6%). This is due to far separation distance of the particle resulting in less total grid number. When generating the grid, total number of

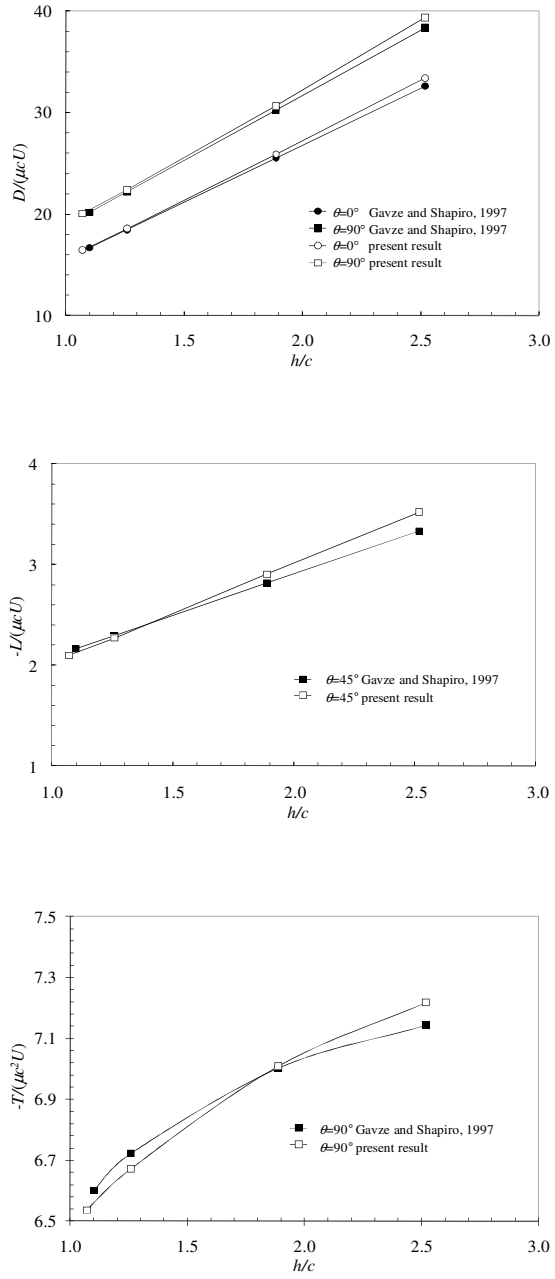

Fig. 9: The normalized forces $D/(\mu cU)$, $L/(\mu cU)$ and torque $T/(\mu c^2 U)$ on an ellipsoidal particle (b=0.397 μm and c=0.794 μm) as a function of the separation distance from the wall in a linear shear flow: comparison between the numerical results by Gavze and Shapiro (1997) and the numerical results retrieved with the present approach.

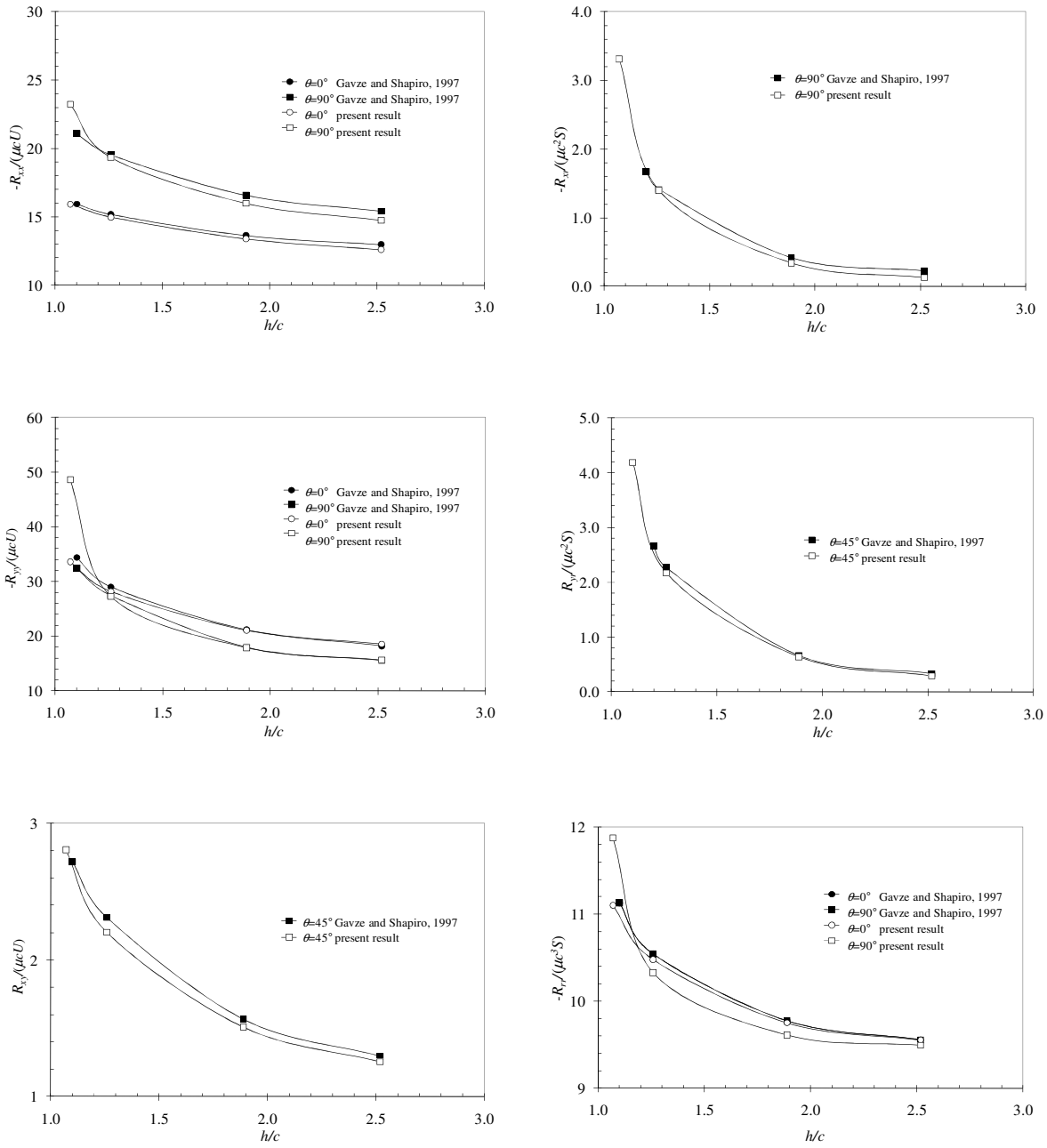

Fig. 10: The normalized Resistance forces $Rxx/(\mu cU)$, $Ryy/(\mu cU)$, $Rxy/(\mu cU)$, $Rxr/(\mu c^2U)$, $Ryr/(\mu c^2U)$ and $Rrr/(\mu c^3U)$ on an ellipsoidal particle (b=0.397 μm and c=0.794 μm) as a function of the separation distance from the wall in a linear shear flow: comparison between the numerical results by Gavze and Shapiro (1997) and the numerical results retrieved with the present approach.

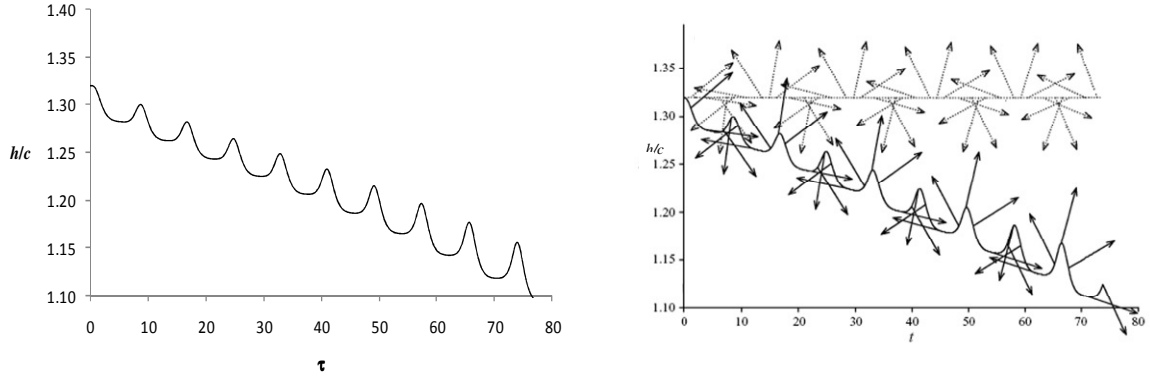

(a) Present study (b)

Fig. 11: Comparison of (a) trajectory of ellipsoid particle (γ_e=0.5) for St_c=25 of current study with (b) previous study (Gavze and Shapiro, 1998)

gird is decreased as the separation distance increases. Since grid information is applied only on the boundary, the space between the particle and the bottom wall in the calculating domain has fewer grids with large separation distance. Other than this point, percentage error is less than 3%. In case of resistance tensor, maximum error is less than 6.7% for R_{rr} at h/c=0.85. From previous result by Gavze and Shapiro, it has been assumed that R_{rr} is independent to the particle angle. Actually, the variation according to the particle angle is relatively smaller than the other component of drag vector and resistance tensor. However, at the proximity of the wall, the variation of R_{rr} cannot be ignored. (Appendix B) In the present study, since all of the drag and resistance tensor was estimated according to every 15° particle angle, the error for R_{rr} is mainly comes from it.

Fig. 11 shows the comparison between the trajectory of prolate ellipsoidal particle (γ_e=0.5) of current study and the previous results by Gavze and Shapiro. To compare with previous result, St_c ($=\rho_p c^2 S/\mu$) is defined based on the major axis of ellipsoid, c. For St_c=25 with initial condition (x_0/c, $u_0/(Sc)$, y_0/c, $v_0/(Sc)$, θ_0, Ω_0/S) = (0, Sc, 1.32, 0, $\pi/2$, -0.5), which is same initial condition used by Gavze and Shapiro, particle trajectory has been calculated. As shown in the Fig. 11, overall trajectory and margination speed is identical.

In both cases, particle reaches to h/c=1.0 at $\tau \approx 75$ and shows similar oscillating characteristics. These results imply that current approach to calculate particle trajectory can be applies with great accuracy with previous prediction.

2.4 Particle margination in the absence of gravitation

2.4.1 Effect of Stokes number

Assuming that the particle volume is fixed and referring to an equivalent spherical bead with radius a_{eq}, the trajectory of non spherical particle has been calculated as a function of Stokes number (St_a), which is measure of inertial force on the particle to the viscous force by the hydrodynamic interaction. Particle Stokes number (St_a) can be induced by non-dimensionalizing Newton's law of motion in Eq. (8). Stokes number for the non-spherical particle is defined as

$$St_a = \frac{\rho_p a_{eq}{}^2 S}{\mu} \tag{11}$$

where a_{eq} is equivalent radius of non spherical particle. Equivalent radius of non-spherical particle can be defined as where V_{ns} is the volume of non spherical particle. As a test case, prolate ellipsoidal particle with aspect ratio γ_e=0.5 has been chosen to compare to the previous results (Pozrikidiz, 2006 and Gavze and Shapiro, 1997).

$$\frac{4}{3}\pi a_{eq}{}^3 = V_{ns} \tag{12}$$

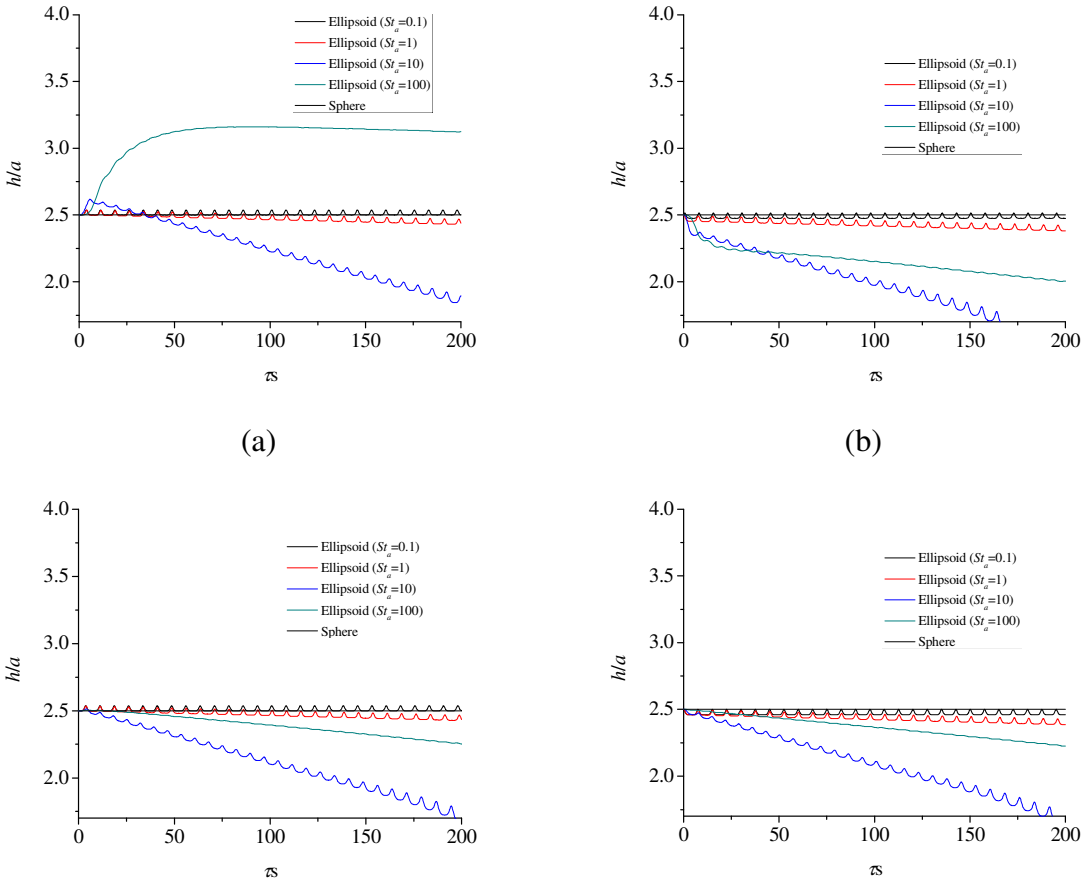

Fig. 12: The trajectory of ellipsoidal particle (γ_e =0.5) with different initial condition
(a) (x_0/a, $u_0/(Sa)$, y_0/a, $v_0/(Sa)$, θ_0, Ω_0/S) = (0, 0, 2.5, 0, 0, 0)
(b) (x_0/a, $u_0/(Sa)$, y_0/a, $v_0/(Sa)$, θ_0, Ω_0/S) = (0, 0, 2.5, 0, $\pi/2$, 0)
(c) (x_0/a, $u_0/(Sa)$, y_0/a, $v_0/(Sa)$, θ_0, Ω_0/S) = (0, Sa, 2.5, 0, 0, -0.5)
(d) (x_0/a, $u_0/(Sa)$, y_0/a, $v_0/(Sa)$, θ_0, Ω_0/S) = (0, Sa, 2.5, 0, $\pi/2$, -0.5)

Stokes number is proportional to the particle density, shear rate and square of particle characteristic length (equivalent radius) and is inversely proportional to the fluid viscosity. Thus, by controlling Stokes number, the effect of size, material density and flow condition can be examined. For example, with fixed flow condition (fixed S and μ) by increasing Stokes number, effect of size can be investigated.

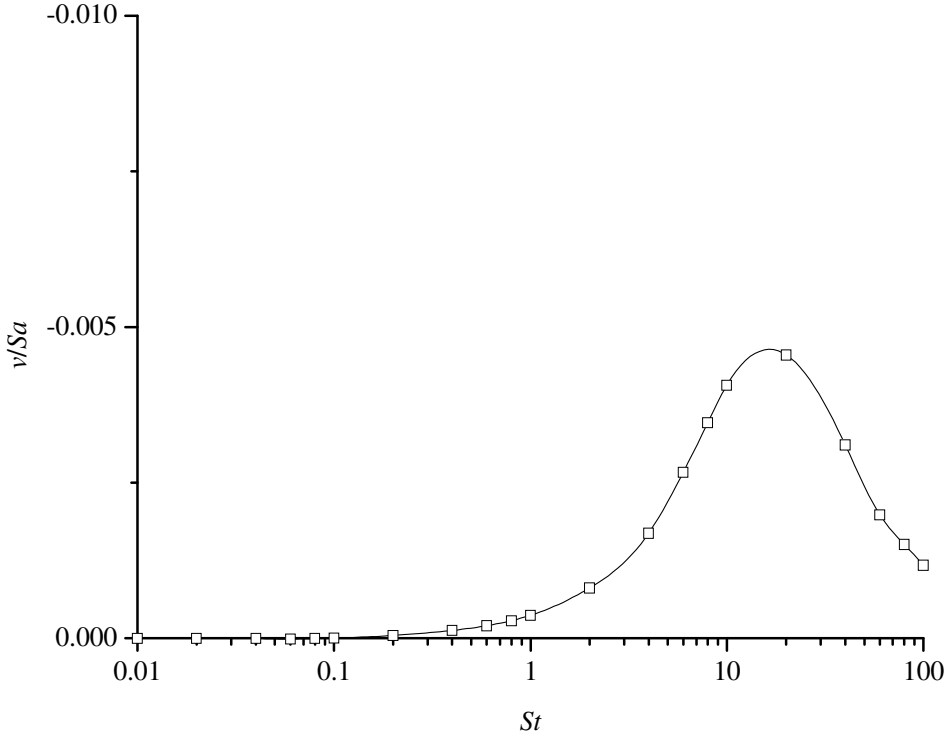

Fig. 13: Normalized drift velocity $v/(Sa)$ of ellipsoidal particle (γ_e=0.5) with initial condition (x_0/a, $u_0/(Sa)$, y_0/a, $v_0/(Sa)$, θ_0, Ω_0/S) = (0, 0, 2.5, 0, $\pi/2$, 0)

To see the effect of initial particle condition, the trajectory of ellipsoidal particle in linear shear flow was examined with different initial condition. Fig. 12 shows the trajectory of ellipsoidal particle (γ_e=0.5). Fig. 12 (a) and (b) are the trajectory of initially stationary ellipsoidal particle (u_0=0, v_0=0 and Ω_0=0) with initial particle angle of 0 and $\pi/2$. Fig. 12 (c) and (d) are initially moving particle which has initial particle velocity same as x-directional flow velocity at initial particle location with initial particle angle of 0 and $\pi/2$. The trajectory of spherical particle is compared to the trajectory of ellipsoidal particle.

Rotating particle makes boundary layer distortion and the difference of upper and lower side boundary layer creates force perpendicular to the flow direction. This is called

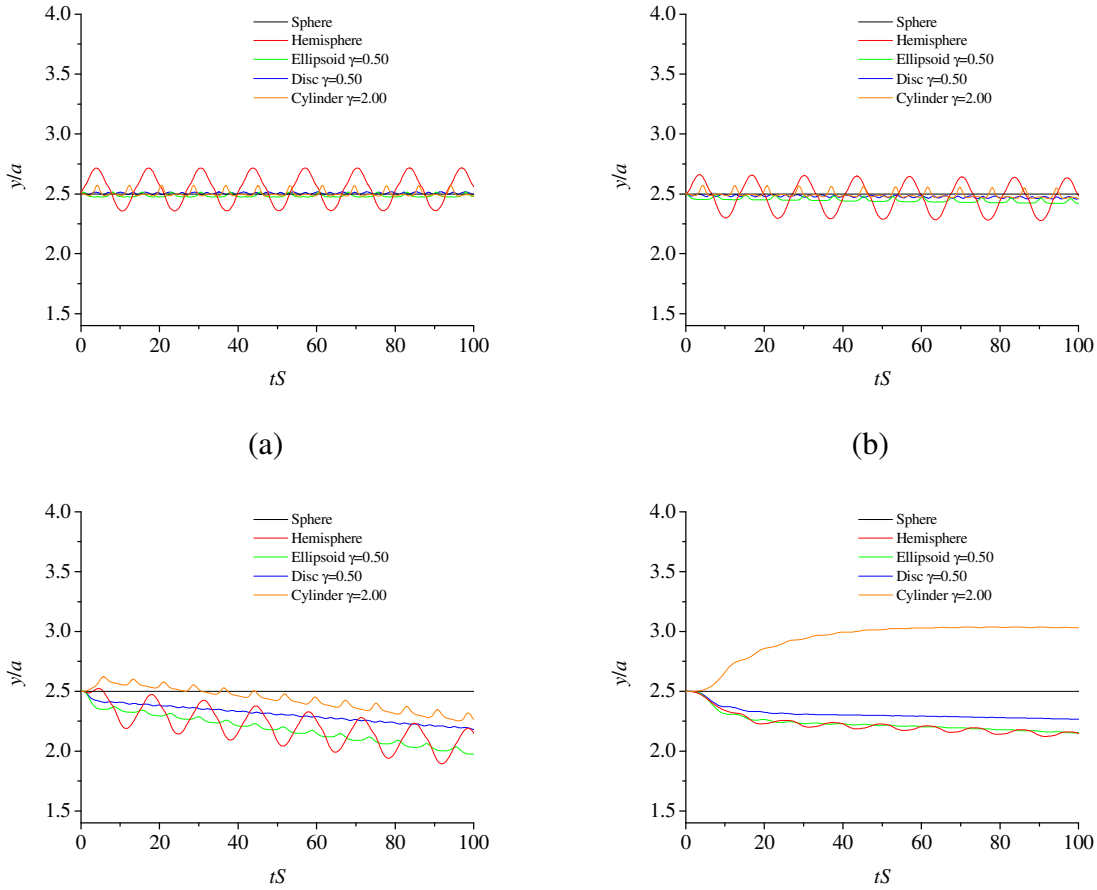

Fig. 14: The trajectory of different shape of particle with initial condition of (x_0/a, $u_0/(Sa)$, y_0/a, $v_0/(Sa)$, θ_0, Ω_0/S) = (0, 0, 2.5, 0, $\pi/2$, 0). (a) St_a=0.1, (b) St_a=1, (c) St_a=10 and (d) St_a=100

Magnus effect. In this study, Magnus effect for rotating particle is neglected. In the linear shear flow, it has been known that positive Magnus effect is valid only when $Re_{shear}^{1/2}$, which is Reynolds number based on the shear rate, is much larger than Re_{slip}, which is Reynolds number based on the slip velocity and negative effect occurs for $Re_{shear}^{1/2} << Re_{slip}$. However, when $Re_{shear}^{1/2} \approx Re_{slip}$, Magnus effect is negligible (McLaughlin, 1991). In the current study, O($Re_{shear}^{1/2}$) is same as O(Re_{slip}) and it has been neglected.

For small St_a, initial condition does not affect much on particle trajectory, that is, particle just follows characteristic oscillating trajectory. It is because of the small characteristic time of small St_a. Characteristic time (τ_{ch}) for this case can be defined as $\rho_p c^2/\mu$ following Gavze and Shapiro (Gavze and Shapiro, 1998). For example, in the physiologically meaningful range of shear rate ($O(10^1)<S<O(10^4)$), St_a=0.1 will give characteristic time of $O(10^{-5})<St_a<O(10^{-1})$, which means that it could catch the characteristic oscillating pattern within very short time. However, for higher St_a, it would take more time because of bigger characteristic time (higher inertia of the particle). For example when St_a=100, characteristic time is $O(10^{-2})<St_a<O(10^2)$. A lateral drift velocity v^d can be calculated by dividing the displacement along y–direction of the particle by the time interval. The normalized lateral drift velocity $v^d/(Sa)$ is plotted in Fig. 14 as a function of the particle shape and Stokes number with initial angle of the particle of $\pi/2$. With small St_a, the ellipsoidal particle does not drift toward the wall. However, when St_a >0.2, the ellipsoidal particle starts to marginate. Drift velocity of particle is increasing until St_a = 20 where the ellipsoidal particle has maximum drift velocity, and then decreases. For St_a > 20, with higher particle inertia (higher St_a), it takes more time to reach to the wall.

2.4.2 Effect of shape

The inertial effect of non-spherical particle makes the particle marginate toward the wall. Then, the question is which shape could be the optimum in terms of margination. In this section, effect of shape change on the particle drift characteristics will be considered. As discussed in the previous section, non-spherical particle drifts toward the wall. However, even though it has been shown that there are various types of

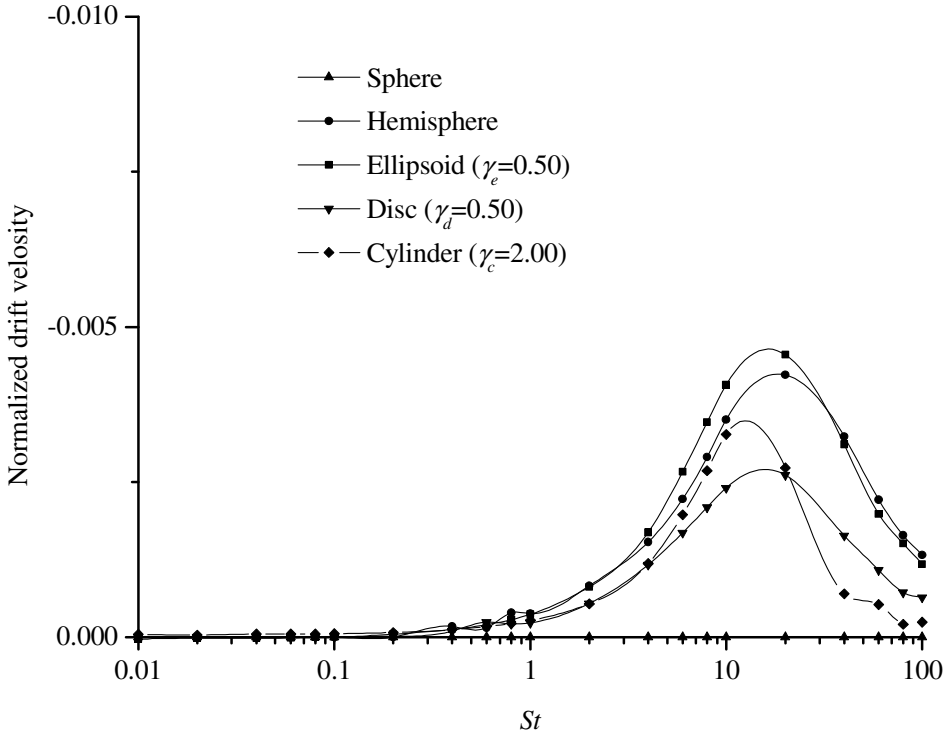

Fig. 15: Normalized drift velocity $v/(Sa)$ of different shape particle (sphere, ellipsoid (γ_e=0.5), disc (γ_d=0.5), cylinder (γ_c=2.00) and hemisphere) with initial condition (x_0/a, $u_0/(Sa)$, y_0/a, $v_0/(Sa)$, θ_0, Ω_0/S) = (0, 0, 2.5, 0,π/2, 0)

particle shape can be fabricated, the optimal particle shape in terms of particle margination has been barely investigated. Following the same procedure, with different particle shape, the particle trajectory and drift velocity will be discussed.

Fig. 14 shows the particle trajectory of different shape (sphere, ellipsoid (γ_e =0.5), disc (γ_d=0.5), cylinder (γ_c =2.0) and hemisphere) of nano/micro particle for St_a=0.1, 1, 10 and 100 with initial condition of (x_0/a, $u_0/(Sa)$, y_0/a, $v_0/(Sa)$, θ_0, Ω_0/S) = (0, 0, 2.5, 0, π/2, 0). With small Stokes number (St_a=0.1), the particle is just oscillating and does not drift across the streamline. However, with higher St_a (St_a=1), ellipsoid (γ_e=0.5) and hemisphere shows small margination. As increase St_a further (St_a=10), all types of

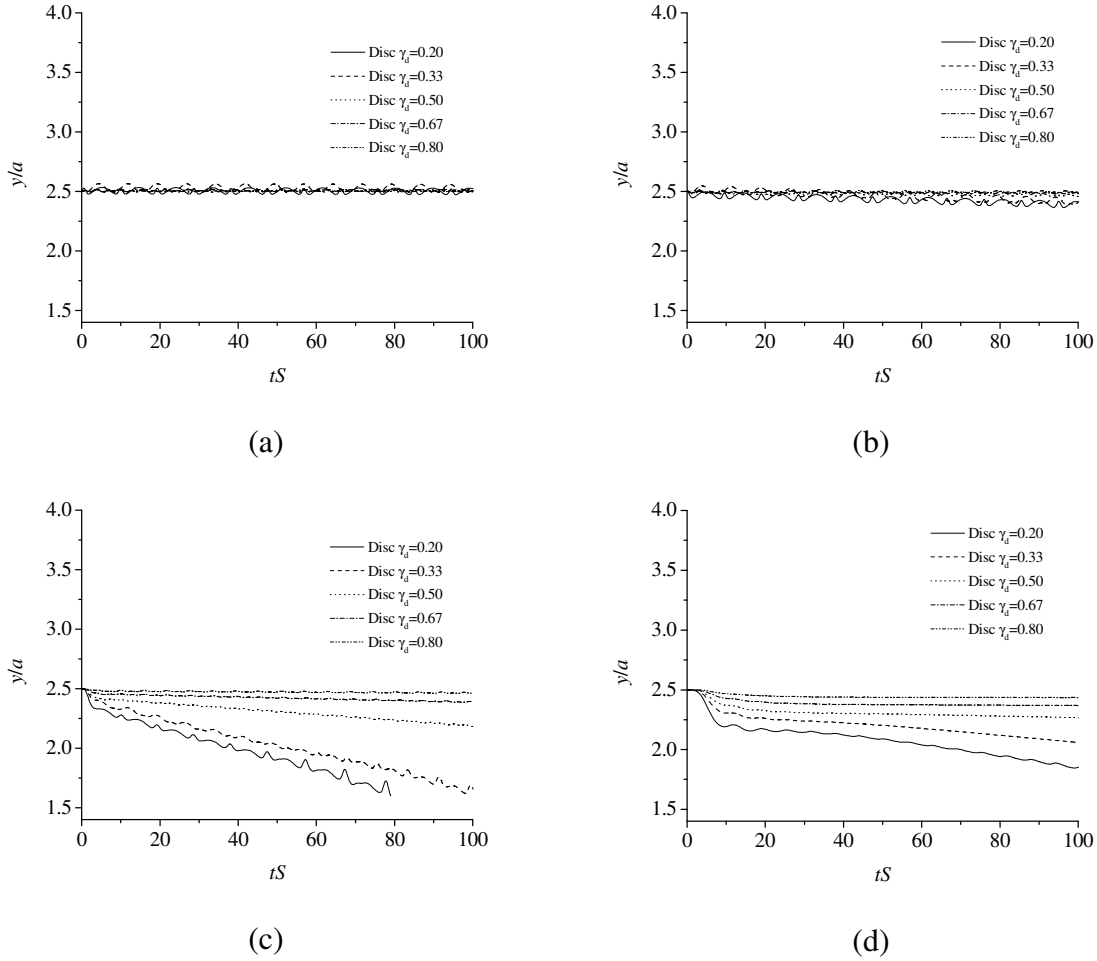

Fig. 16: The trajectory of discoidal particle for different aspect ratio with initial condition of (x_0/a, $u_0/(Sa)$, y_0/a, $v_0/(Sa)$, θ_0, Ω_0/S) = (0,0,2.5,0,π/2, 0). (a) St_a=0.1, (b) St_a=1, (c) St_a=10 and (d) St_a=100

particle drift with relatively higher drift velocity. However, at St_a=100, drift velocity is smaller than St_a=10. When compared for St_a=10, ellipsoidal particle (γ_e=0.5) and hemispherical particle show faster drift than the other types of particle. Hemispherical particle shows larger amplitude than the other types of particle since asymmetric shape of hemispherical particle. Fig. 15 shows drift velocity of different shape of particle according to the wide range of St_a. Spherical particle does not marginate. It is because the shape of the spherical particle is symmetric and then there is no imbalance of viscous

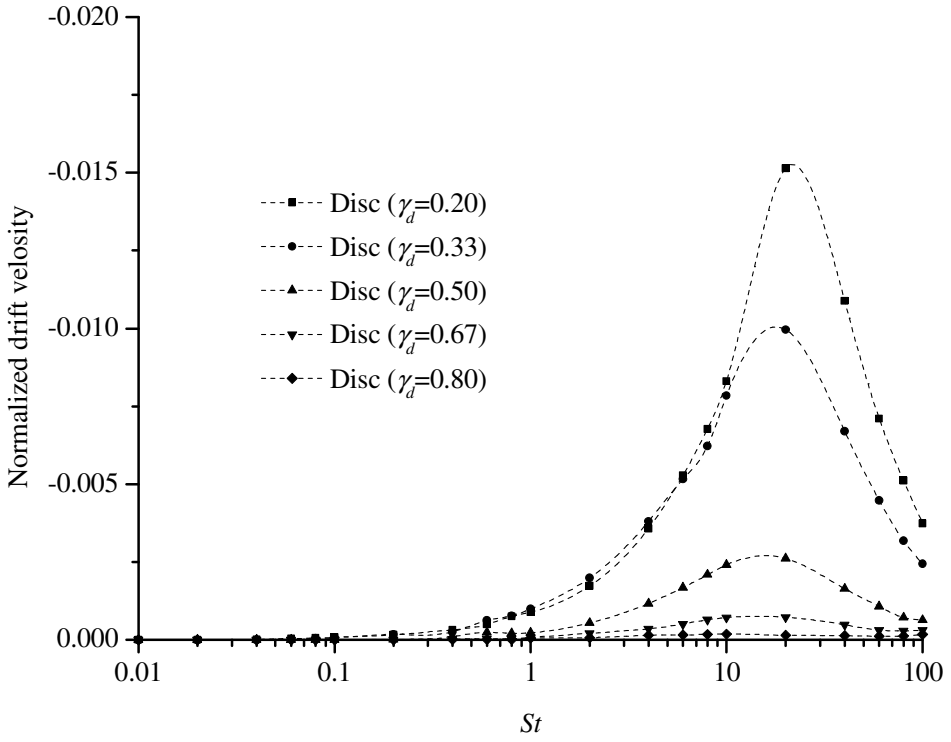

Fig. 17: Normalized drift velocity $v/(Sa)$ of discoidal particle ($0.2<\gamma_d<0.8$) with initial condition (x_0/a, $u_0/(Sa)$, y_0/a, $v_0/(Sa)$, θ_0, Ω_0/S) = (0, 0, 2.5, 0, $\pi/2$, 0)

interaction caused by the linear shear flow. However, similar to the ellipsoidal particle, there exists optimal St_a in terms of particle drift velocity. Maximum drift velocity is at St_a=20 for ellipsoid (γ_e=0.5), disc (γ_d=0.5) and hemisphere. However, cylindrical particle (γ_c=2.0) has maximum drift velocity at St_a=10.

2.4.3 Effect of aspect ratio (Discoidal particle)

With same aspect ratio (γ=0.5, γ=2.0 for cylindrical particle), even though ellipsoidal and hemispherical particle marginates more than disc and cylinder, it is still interesting to see the effect of aspect ratio of discoidal or cylindrical particle. First, in this

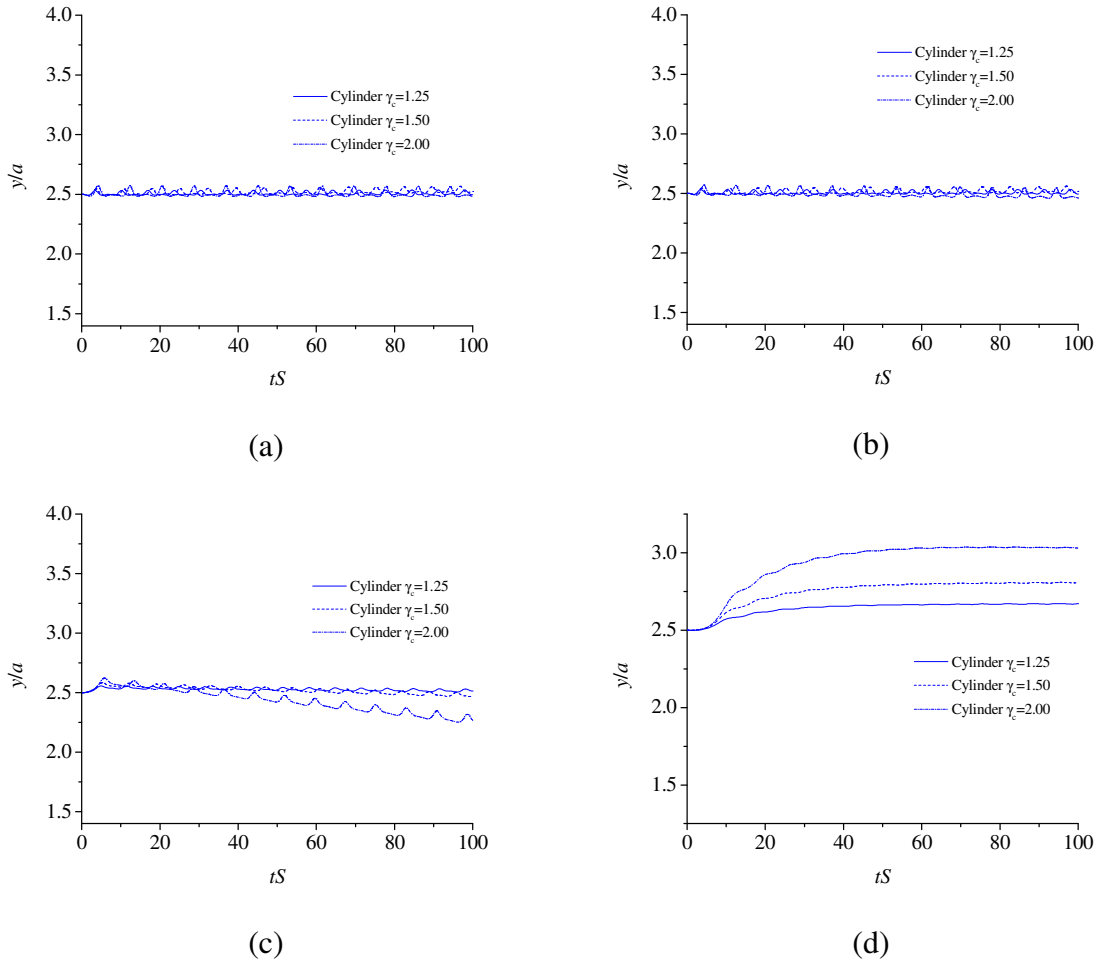

Fig. 18: The trajectory of cylindrical particle for different aspect ratio with initial condition of (x_0/a, $u_0/(Sa)$, y_0/a, $v_0/(Sa)$, θ_0, Ω_0/S) = (0,0,2.5,0,π/2,0). (a) St_a=0.1, (b) St_a=0.1, (c) St_a=0.1 and (d) St_a=100

chapter, the effect of aspect ratio on discoidal particle will be discussed. Considering aspect ratio of disc from 0.2 to 0.8, the particle trajectory of discoidal particle is shown in Fig. 16. Smaller aspect ratio is flat discoidal particle. For St_a=0.1, particle does not marginate by changing aspect ratio. However, for St_a=1, discoidal particle with γ_d=0.2 and 0.33 shows a little margination, which seems not to be apparent in ellipsoidal (γ_e=0.5), discodial (γ_d>0.5), cylindrical (γ_c=2.0) and hemispherical particles (Fig. 16). For St_a=10, the difference of particle trajectory according to the aspect ratio is clearly seen.

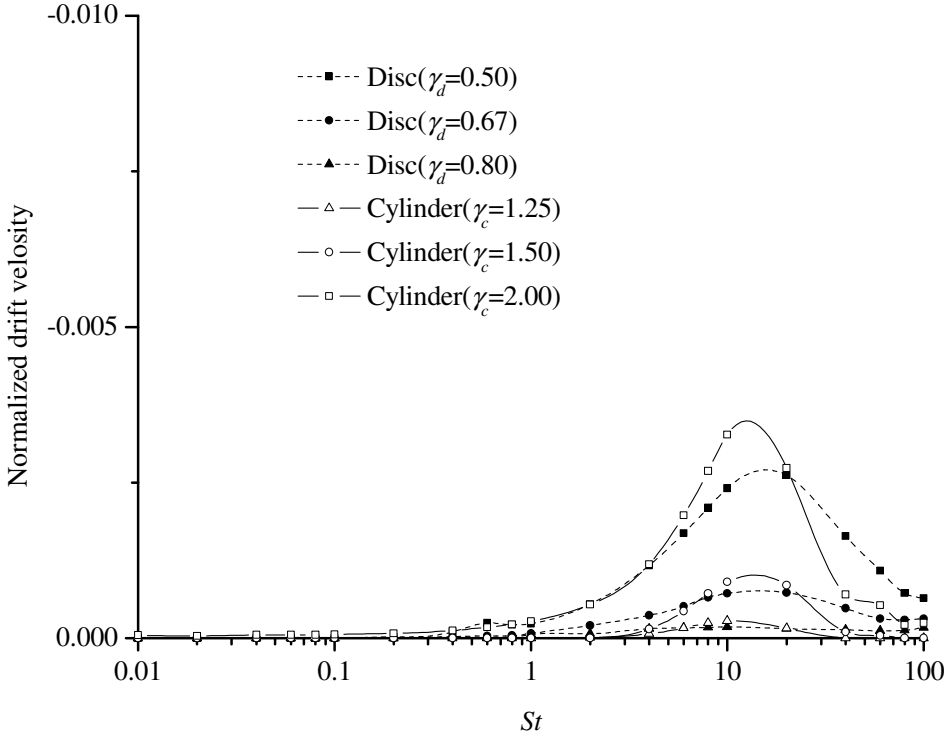

Fig. 19: Comparison of normalized drift velocity $v/(Sa)$ of discoidal ($0.5<\gamma_c<0.8$) and cylindrical particle ($1.25<\gamma_c<2.00$) with initial condition (x_0/a, $u_0/(Sa)$, y_0/a, $v_0/(Sa)$, θ_0, Ω_0/S) = (0, 0, 2.5, 0, $\pi/2$, 0)

As aspect ratio decreases, particle marginates quickly. Indeed, discoidal particle with aspect ratio γ_d=0.2, shows fastest margination among all types of particle compared. Even though discoidal particle with aspect ratio γ_d=0.5 is slower margination than ellipsoidal (γ_d=0.5) and hemispherical particle, the discoidal particle with γ_d =0.2 is much faster than ellipsoidal (γ_d=0.5) and hemispherical particle. This is because of much larger interaction area of discoidal particle. Faster margination characteristics can be clearly observed in Fig. 17 that shows the drift velocity of discoidal particle for different aspect ratio with initial condition of (x_0/a, $u_0/(Sa)$, y_0/a, $v_0/(Sa)$, θ_0, Ω_0/S) = (0,0,2.5,0,$\pi/2$,0) in the absence of gravitational force (no external body force). As described previously, the drift velocity

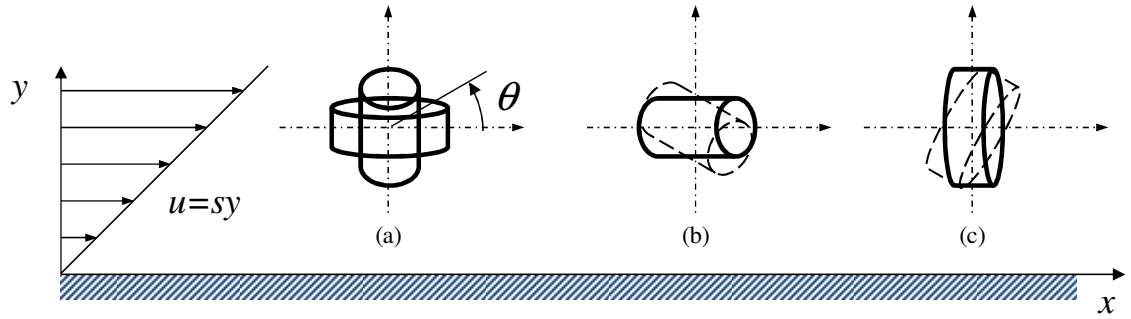

Fig. 20: Schematic of particle orientation (a) definition of particle angle for discoidal and cylindrical particle (θ_0=0), (b) initial orientation (θ_0=π/2) and initial rotating motion (shown in dotted line) of discoidal particle (c) initial orientation (θ_0= π/2) and initial rotating motion of cylindrical particle

of discoidal particle with aspect ratio γ_d=0.2 is the fastest among the aspect ratios compared. As aspect ratio increases, the drift velocity of discoidal particle decreases. The discoidal particle with larger aspect ratio (γ_d>0.5) has margination for St_a>1, but the discoidal particle with smaller aspect ratio (γ_d<0.33) starts to marginate for St_a>0.4. Consequently, as long as vessel size is large enough to pass through, the discoidal particle with smaller aspect ratio, for example, γ_d=0.2 or 0.33, is favorable in terms of margination.

2.4.4 Effect of aspect ratio (Cylindrical particle)

The discoidal particle with aspect ratio that is larger than 1 has cylindrical shape. In this chapter, following the same procedure used in the previous chapters, the trajectory of cylindrical particle (γ_c>1) at the proximity of the wall in linear shear flow and drift velocity will be presented. And the difference of the particle dynamics between discodial and cylindrical particle for corresponding aspect ratio will be compared. The trajectory of cylindrical particle with different St_a for aspect ratio γ_c=1.25, 1.50 and 2.00 is presented in Fig. 18. The aspect ratio of cylindrical particle chosen in this study is reciprocal of the aspect ratio used for discoidal particle. The aspect ratios chosen for cylindrical particle,

γ_c=1.25, 1.50 and 2.00, are corresponding to the aspect ratios for discoidal particle, γ_d=0.8, 0.67 and 0.5, respectively. For small Stoke's number (St_a<1), similarly to the discoidal particle with aspect ratio of γ_d=0.8, 0.67 and 0.5, cylindrical particle with γ_c=1.25, 1.50 and 2.00 does not marginate much. As shown in Fig. 18, the trajectory of cylindrical particle for St_a=0.1 and 1.0 just oscillates following the streamline and does not marginate toward the wall. Interestingly, for St_a=10, initially particle move away from the wall and then drift toward the wall. It is because of the difference of initial orientation of discoidal and cylindrical particle and particle rotation induced by shear flow. The initial condition for particle angle is $\pi/2$. In case of horizontal capillary, the particle is in the linear shear flow as shown in Fig. 20 (b) and (c) and the shear flow create particle rotation in clockwise direction, which makes cylindrical particle move upward but discoidal particle move downward. This initial condition makes different *y*-directional initial particle movement.

2.5 Particle margination in linear shear flow in gravitational field

2.5.1 Effect of gravitational direction on particle trajectory

In this paragraph, the combined effect of the hydrodynamic and buoyancy forces is considered ($G \neq 0$). The trajectory of the particles for different values of the Stokes number St_a and dimensionless buoyancy force G are presented in Fig. 21-24 for different shape of particle , namely, an ellipsoidal (γ_e=0.50), hemi-spherical, discoidal (γ_d=0.50), cylindrical (γ_c=0.50) and spherical particle; in Fig. 25-28 for discoidal particles with different aspect ratios, namely, γ_d=0.20, 0.33, 0.50, 0.67 and 0.80; in Fig. 29-32 for cylindrical particles with different aspect ratios, namely, γ_c=1.25, 1.50 and 2.00. Two different values of the Stokes number, namely St_a=1 and 10, and of the dimensionless

buoyancy force *G*, namely G=0.1 and 1, have been considered. All the four possible orientations of the gravitational force with respect to the fluid direction, namely horizontal capillaries with gravitational force towards and away from the wall; vertical capillaries with gravitational force along and against the flow.

As the Stokes number increases from 1 to 10, the drift velocity increases for a fixed *G*. As the buoyancy force increases, the margination speed increases for horizontal capillaries with *G* pointing to the wall as well as for vertical capillaries, for which the largest drift velocity is achieved in descending capillaries. This trajectory has been observed for all the particles regardless of their shape. It is again confirmed that discoidal particles with low aspect ratio have the highest margination speed even within a gravitational field. Very interestingly, the discoidal particles with γ_d = 0.20 and 0.33 in Fig 24 (b) marginate towards the wall even for a gravitational force pointing away from the wall, showing how for such geometry the particle inertia dominates over gravitation. This has been shown in Fig. 25 (b) (St_a =10 and *G*=0.1) in the case of discoidal particles with the lowest aspect ratio (i.e. largest inertial forces). On the other hand, as the aspect ratio increases (γ_d > 0.50 in Fig. 25 (b)) or the gravitational force grows (*G*=1 in Fig. 25 (a)), even the discoidal particles with the largest aspect ratio have been observed to deviate away from the wall following the direction of the applied gravitational force.

The trajectory of cylindrical particle also shows similar to the discoidal particle with aspect ratio, γ_d = 0.80, 0.67 and 0.50 as shown in the case of the trajectory in the absence of gravitational force. Again, for higher St_a (Sta=10), particle start away from the wall but quickly follow the gravitational direction with oscillating motion. In the current study, because of limitation of numerical domain, only aspect ratio of γ_c = 1.25, 1.50 and 2.00 has been conducted. However, similar particle behavior is expected considering higher aspect ratio.

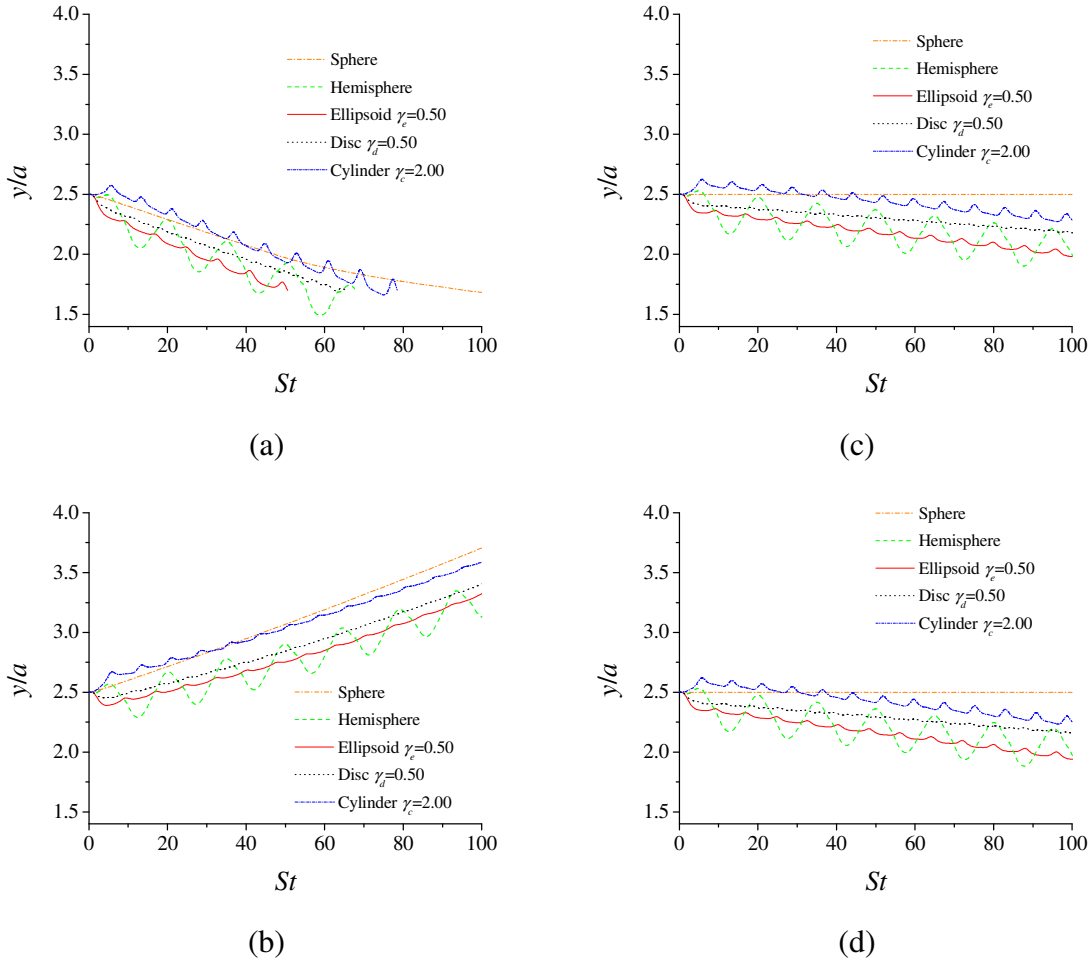

Fig. 21: The trajectory of different shape of particles in a linear laminar flow with initial conditions (x_0/a, $u_0/(Sa)$, y_0/a, $v_0/(Sa)$, θ_0, Ω_0/S) = (0, 0, 2.5, 0, $\pi/2$, 0) for fixed shear rate in the presence of gravitational force (G=0.1, St_a =10)
(a) horizontal capillaries with gravitational force toward the wall
(b) horizontal capillaries with gravitational force away from the wall
(c) vertical capillaries with gravitational force along the flow direction
(d) vertical capillaries with gravitational force against the flow direction

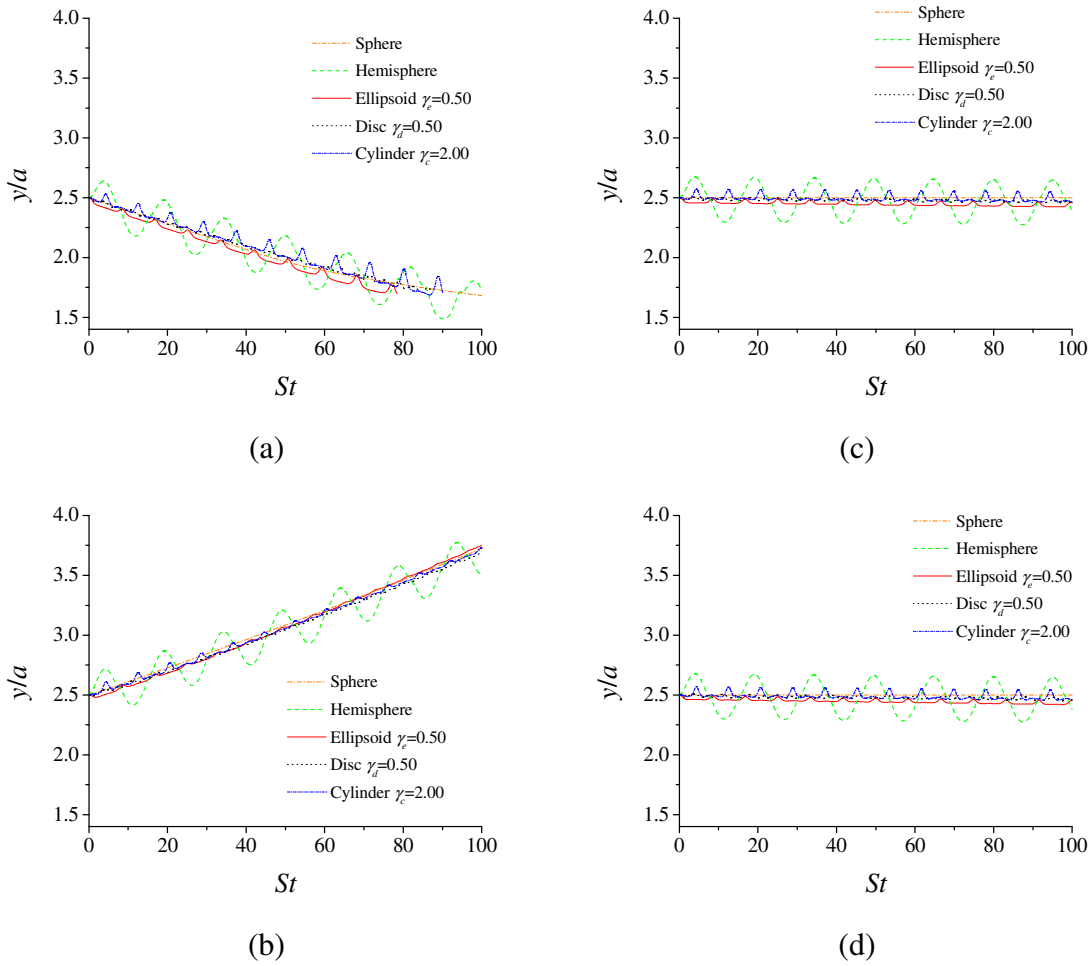

Fig. 22: The trajectory of different shape of particles in a linear laminar flow with initial conditions (x_0/a, $u_0/(Sa)$, y_0/a, $v_0/(Sa)$, θ_0, Ω_0/S) = (0, 0, 2.5, 0, $\pi/2$, 0) for fixed shear rate in the presence of gravitational force (G=0.1, St_a =1)
(a) horizontal capillaries with gravitational force toward the wall
(b) horizontal capillaries with gravitational force away from the wall
(c) vertical capillaries with gravitational force along the flow direction
(d) vertical capillaries with gravitational force against the flow direction

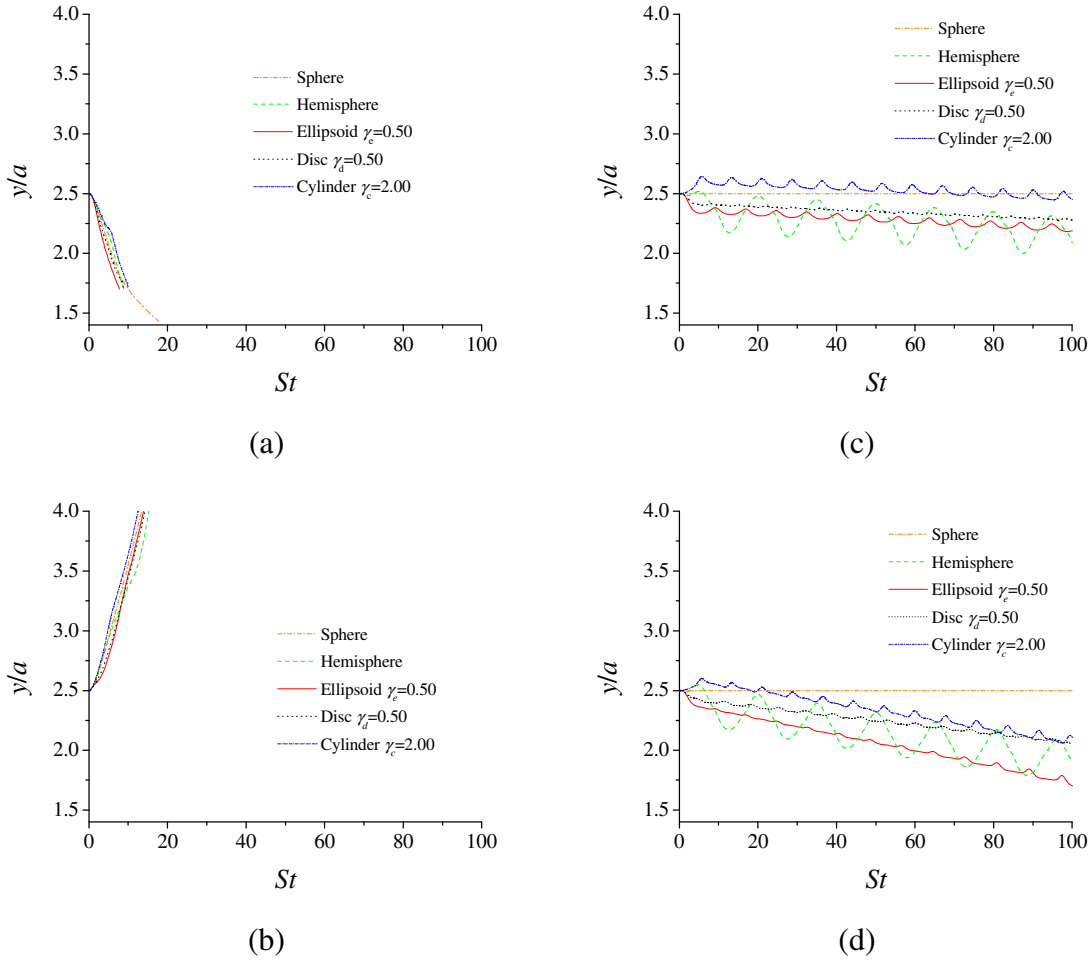

Fig. 23: The trajectory of different shape of particles in a linear laminar flow with initial conditions (x_0/a, $u_0/(Sa)$, y_0/a, $v_0/(Sa)$, θ_0, Ω_0/S) = (0, 0, 2.5, 0, $\pi/2$, 0) for fixed shear rate in the presence of gravitational force (G=1, St_a =10)
(a) horizontal capillaries with gravitational force toward the wall
(b) horizontal capillaries with gravitational force away from the wall
(c) vertical capillaries with gravitational force along the flow direction
(d) vertical capillaries with gravitational force against the flow direction

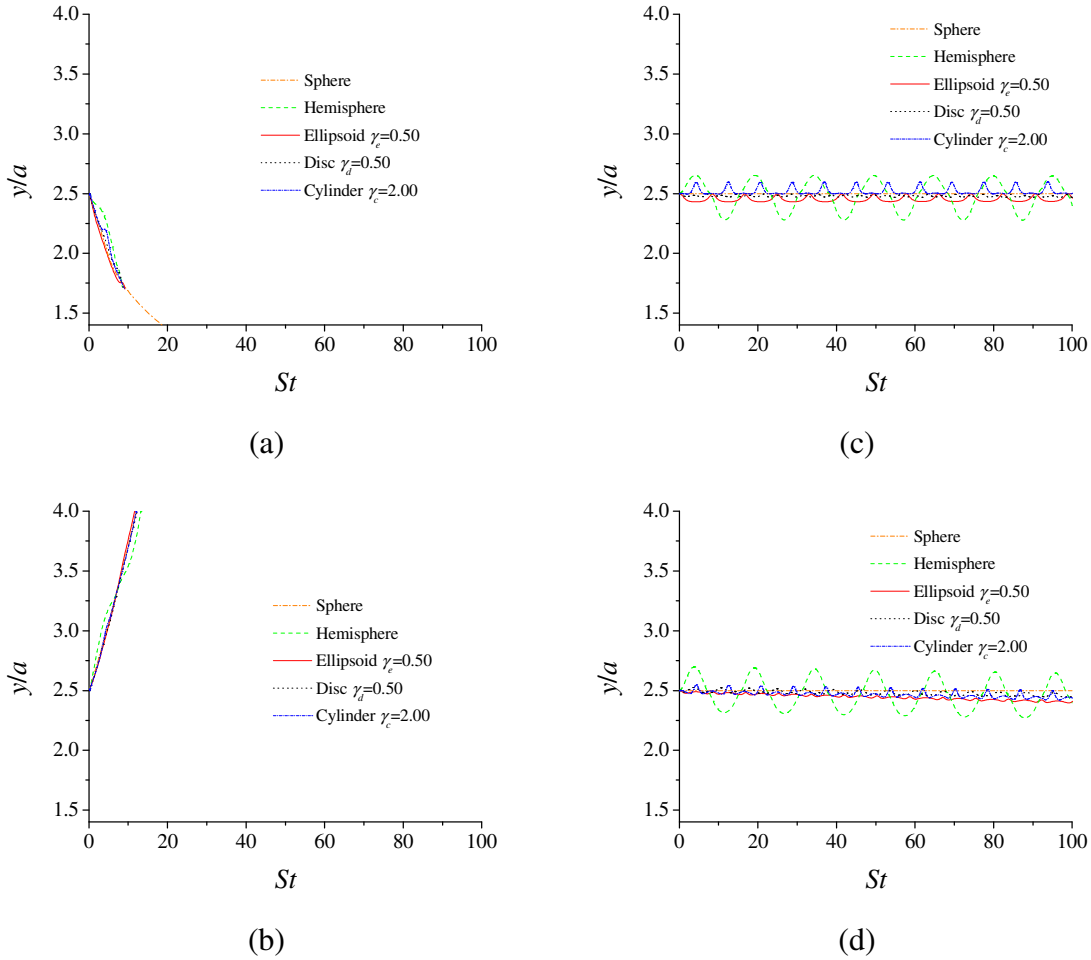

Fig. 24: The trajectory of different shape of particles in a linear laminar flow with initial conditions (x_0/a, $u_0/(Sa)$, y_0/a, $v_0/(Sa)$, θ_0, Ω_0/S) = (0, 0, 2.5, 0, $\pi/2$, 0) for fixed shear rate in the presence of gravitational force (G=1, St_a =1)
(a) horizontal capillaries with gravitational force toward the wall
(b) horizontal capillaries with gravitational force away from the wall
(c) vertical capillaries with gravitational force along the flow direction
(d) vertical capillaries with gravitational force against the flow direction

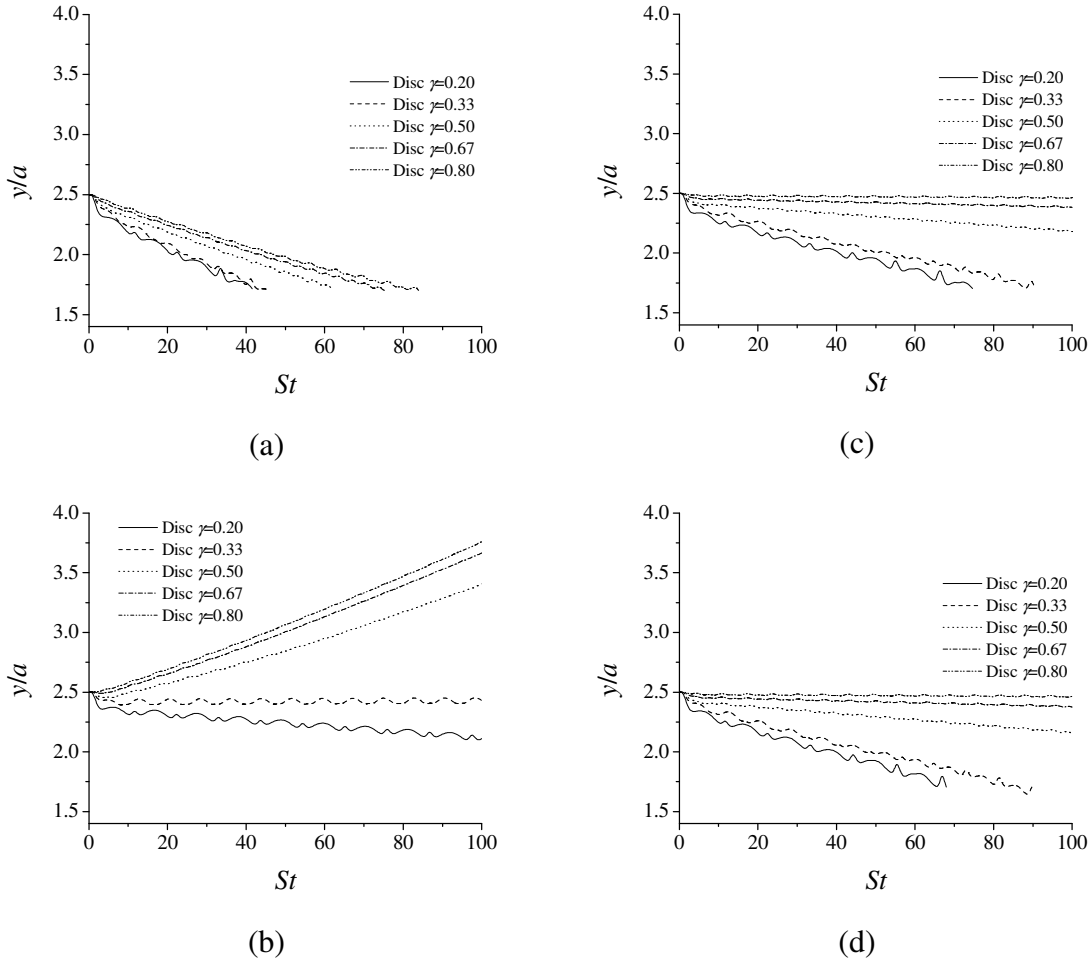

Fig. 25: The trajectory of discoidal particles in a linear laminar flow with initial conditions (x_0/a, $u_0/(Sa)$, y_0/a, $v_0/(Sa)$, θ_0, Ω_0/S) = (0, 0, 2.5, 0, $\pi/2$, 0) for fixed shear rate in the presence of gravitational force (G=0.1, St_a =10)
(a) horizontal capillaries with gravitational force toward the wall
(b) horizontal capillaries with gravitational force away from the wall
(c) vertical capillaries with gravitational force along the flow direction
(d) vertical capillaries with gravitational force against the flow direction

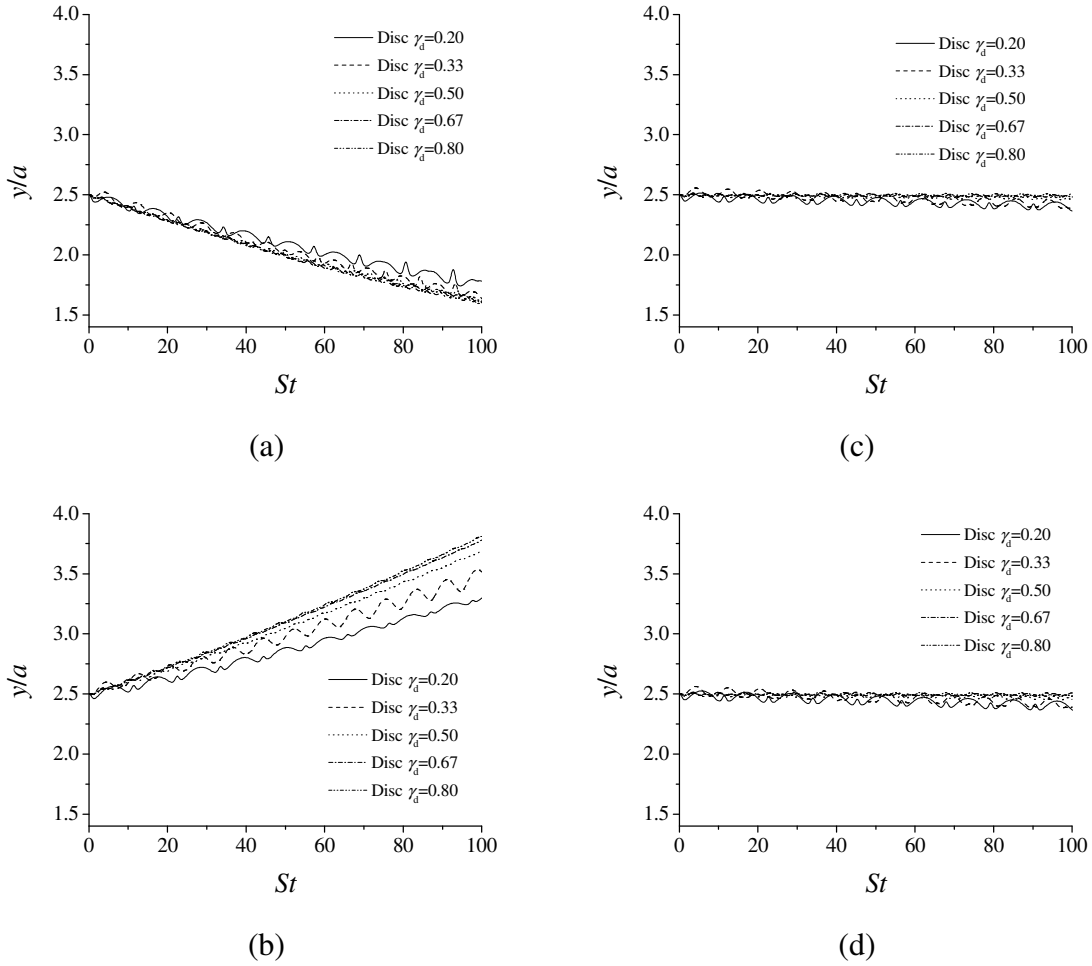

Fig. 26: The trajectory of discoidal particles in a linear laminar flow with initial conditions (x_0/a, $u_0/(Sa)$, y_0/a, $v_0/(Sa)$, θ_0, Ω_0/S) = (0, 0, 2.5, 0, $\pi/2$, 0) for fixed shear rate in the presence of gravitational force (G=0.1, St_a =1)

(a) horizontal capillaries with gravitational force toward the wall

(b) horizontal capillaries with gravitational force away from the wall

(c) vertical capillaries with gravitational force along the flow direction

(d) vertical capillaries with gravitational force against the flow direction

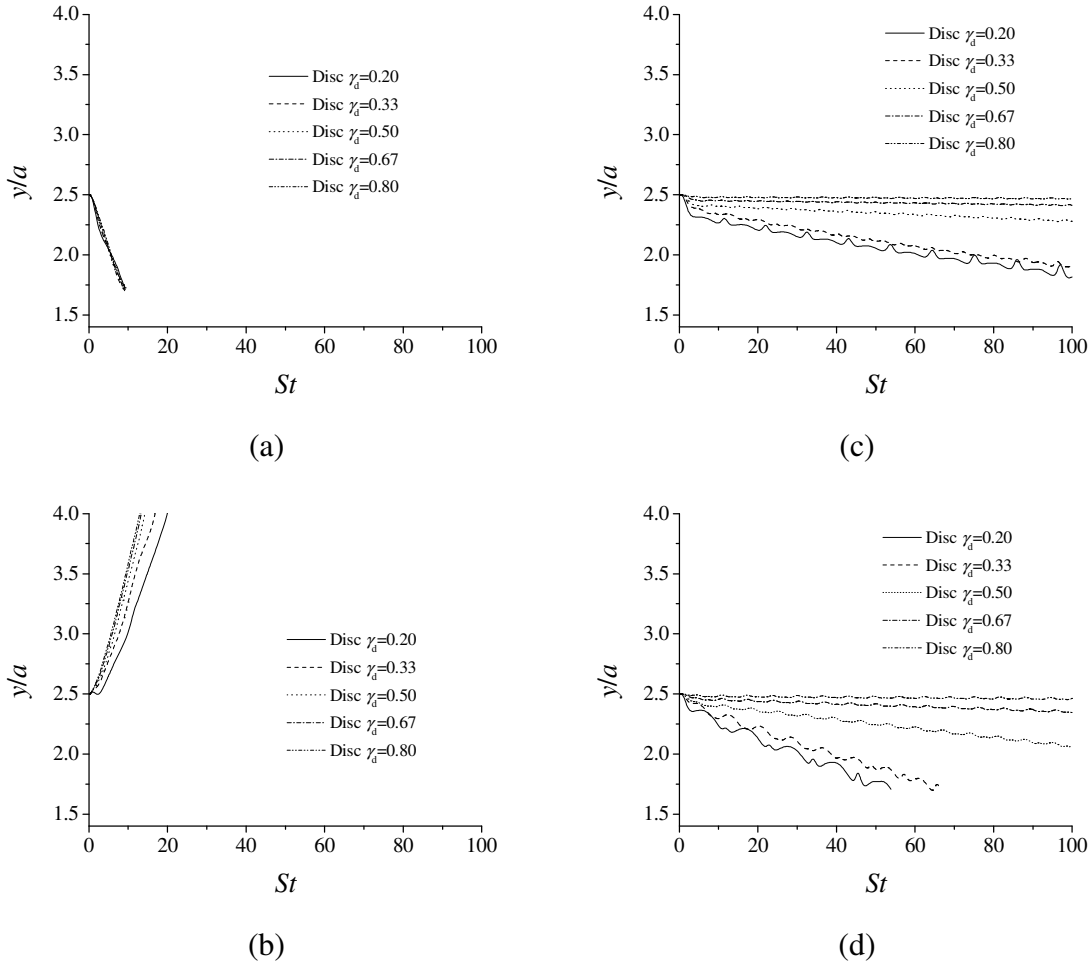

Fig. 27: The trajectory of discoidal particles in a linear laminar flow with initial conditions (x_0/a, $u_0/(Sa)$, y_0/a, $v_0/(Sa)$, θ_0, Ω_0/S) = (0, 0, 2.5, 0, $\pi/2$, 0) for fixed shear rate in the presence of gravitational force (G=1, St_a =10)
(a) horizontal capillaries with gravitational force toward the wall
(b) horizontal capillaries with gravitational force away from the wall
(c) vertical capillaries with gravitational force along the flow direction
(d) vertical capillaries with gravitational force against the flow direction

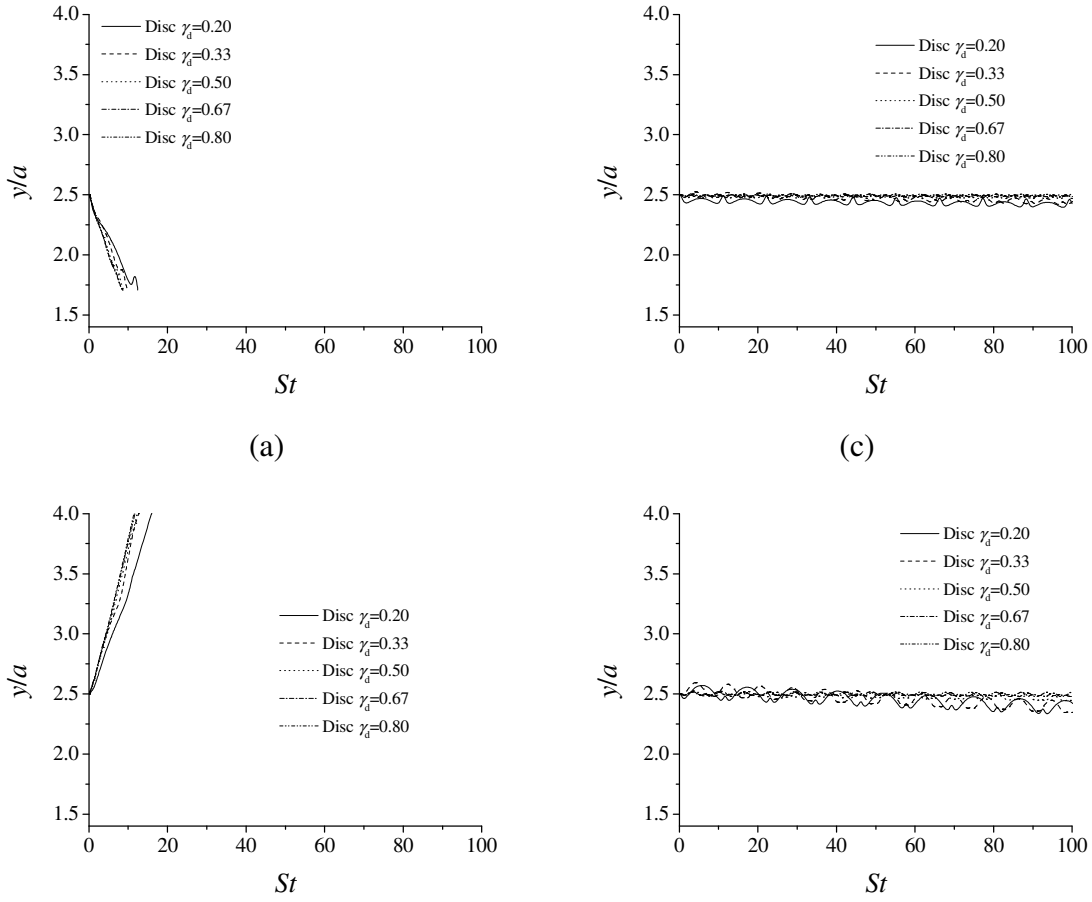

Fig. 28: The trajectory of discoidal particles in a linear laminar flow with initial conditions (x_0/a, $u_0/(Sa)$, y_0/a, $v_0/(Sa)$, θ_0, Ω_0/S) = (0, 0, 2.5, 0, $\pi/2$, 0) for fixed shear rate in the presence of gravitational force (G=1, St_a =1)
(a) horizontal capillaries with gravitational force toward the wall
(b) horizontal capillaries with gravitational force away from the wall
(c) vertical capillaries with gravitational force along the flow direction
(d) vertical capillaries with gravitational force against the flow direction

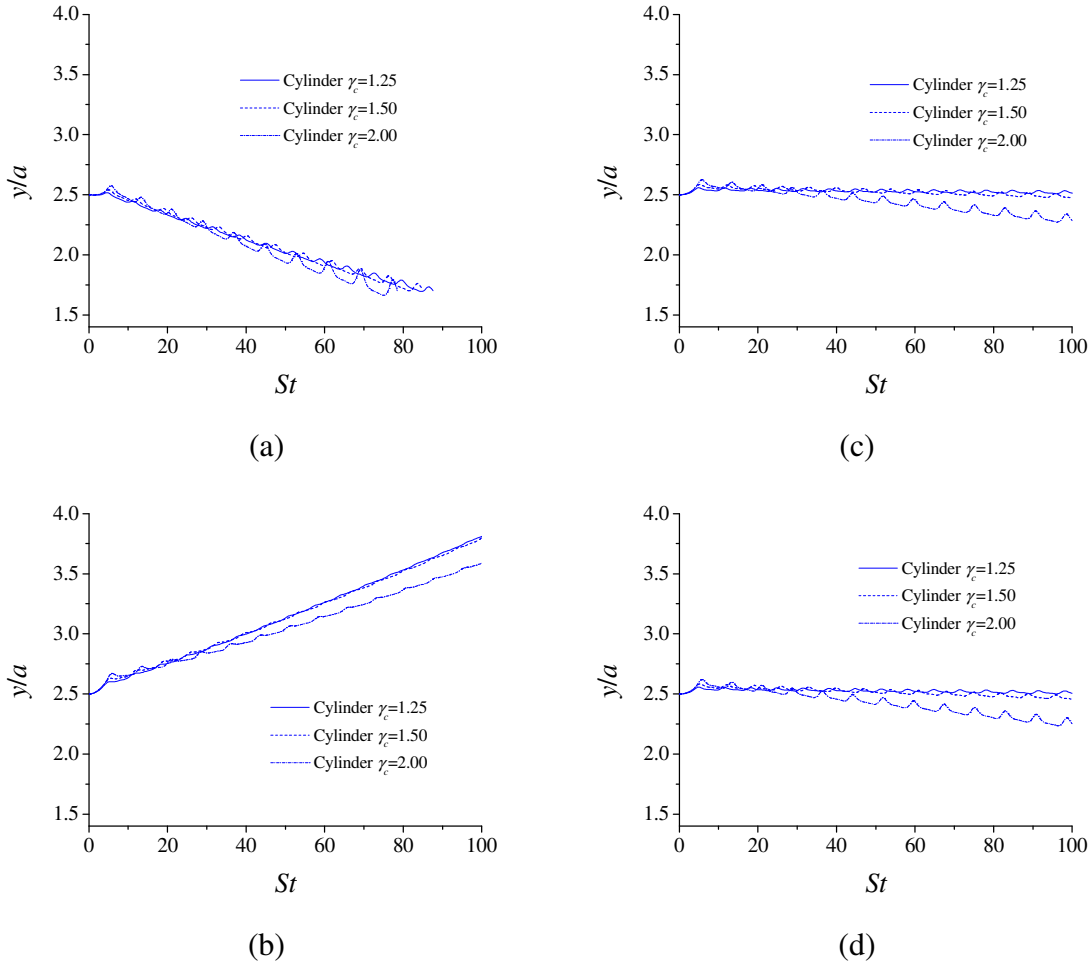

Fig. 29: The trajectory of cylindrical particles in a linear laminar flow with initial conditions (x_0/a, $u_0/(Sa)$, y_0/a, $v_0/(Sa)$, θ_0, Ω_0/S) = (0, 0, 2.5, 0, $\pi/2$, 0) for fixed shear rate in the presence of gravitational force (G=0.1, St_a =100)
(a) horizontal capillaries with gravitational force toward the wall
(b) horizontal capillaries with gravitational force away from the wall
(c) vertical capillaries with gravitational force along the flow direction
(d) vertical capillaries with gravitational force against the flow direction

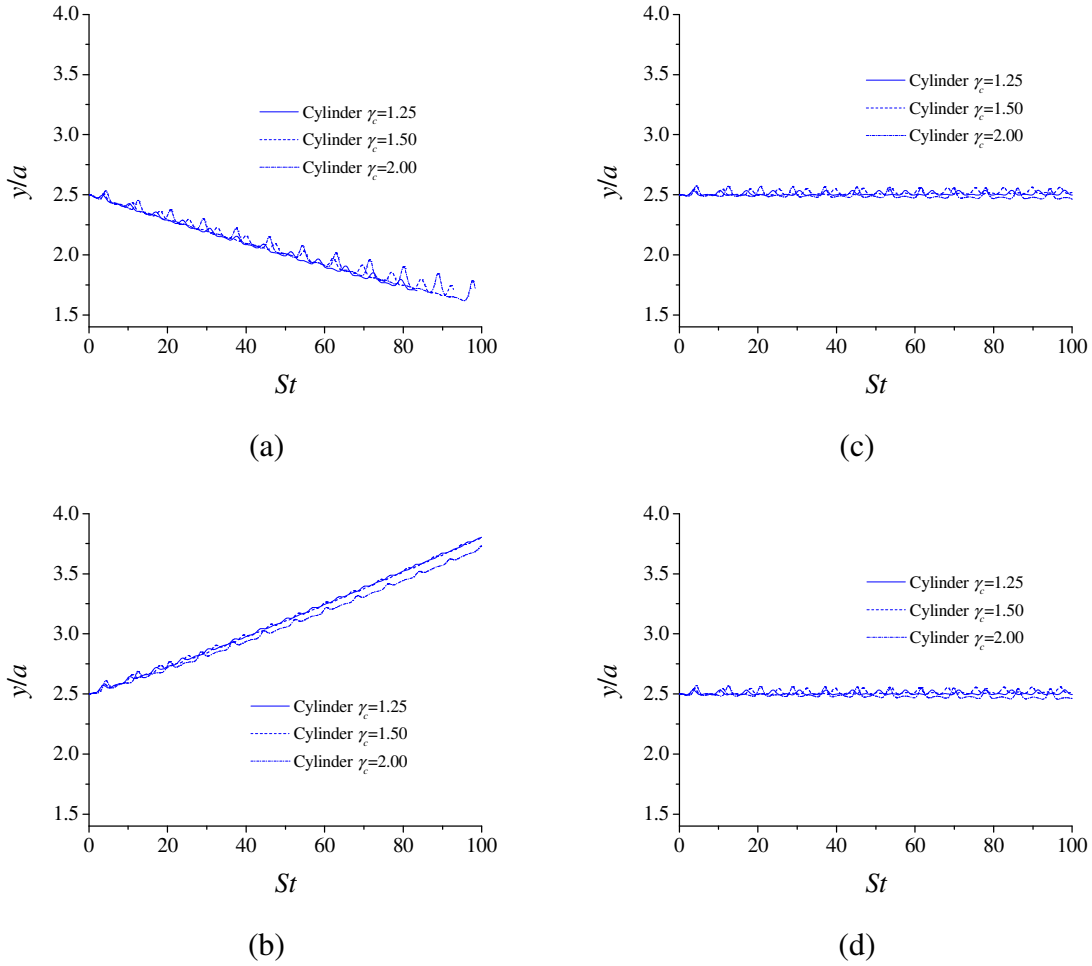

Fig. 30: The trajectory of cylindrical particles in a linear laminar flow with initial conditions (x_0/a, $u_0/(Sa)$, y_0/a, $v_0/(Sa)$, θ_0, Ω_0/S) = (0, 0, 2.5, 0, $\pi/2$, 0) for fixed shear rate in the presence of gravitational force (G=0.1, St_a =1)
(a) horizontal capillaries with gravitational force toward the wall
(b) horizontal capillaries with gravitational force away from the wall
(c) vertical capillaries with gravitational force along the flow direction
(d) vertical capillaries with gravitational force against the flow direction

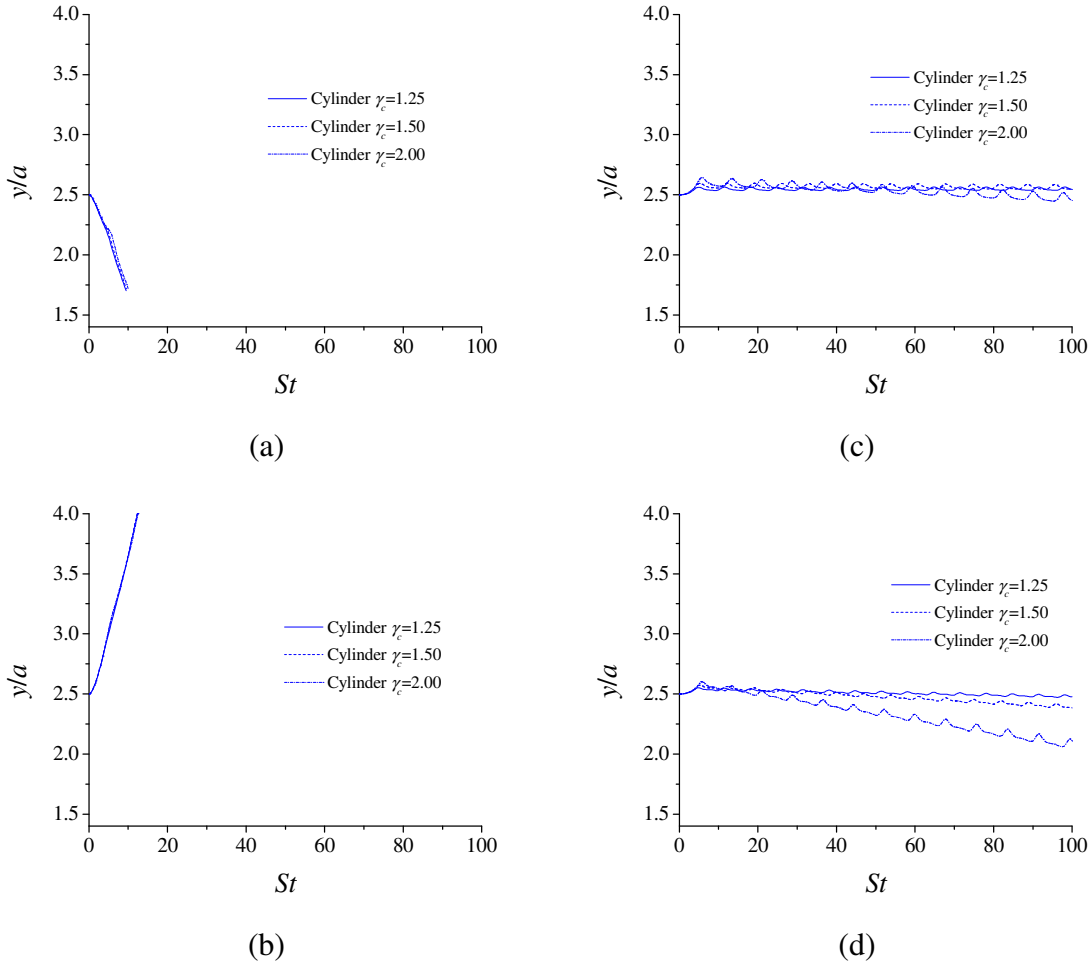

Fig. 31: The trajectory of cylindrical particles in a linear laminar flow with initial conditions (x_0/a, $u_0/(Sa)$, y_0/a, $v_0/(Sa)$, θ_0, Ω_0/S) = (0, 0, 2.5, 0, $\pi/2$, 0) for fixed shear rate in the presence of gravitational force (G=1, St_a =10)
(a) horizontal capillaries with gravitational force toward the wall
(b) horizontal capillaries with gravitational force away from the wall
(c) vertical capillaries with gravitational force along the flow direction
(d) vertical capillaries with gravitational force against the flow direction

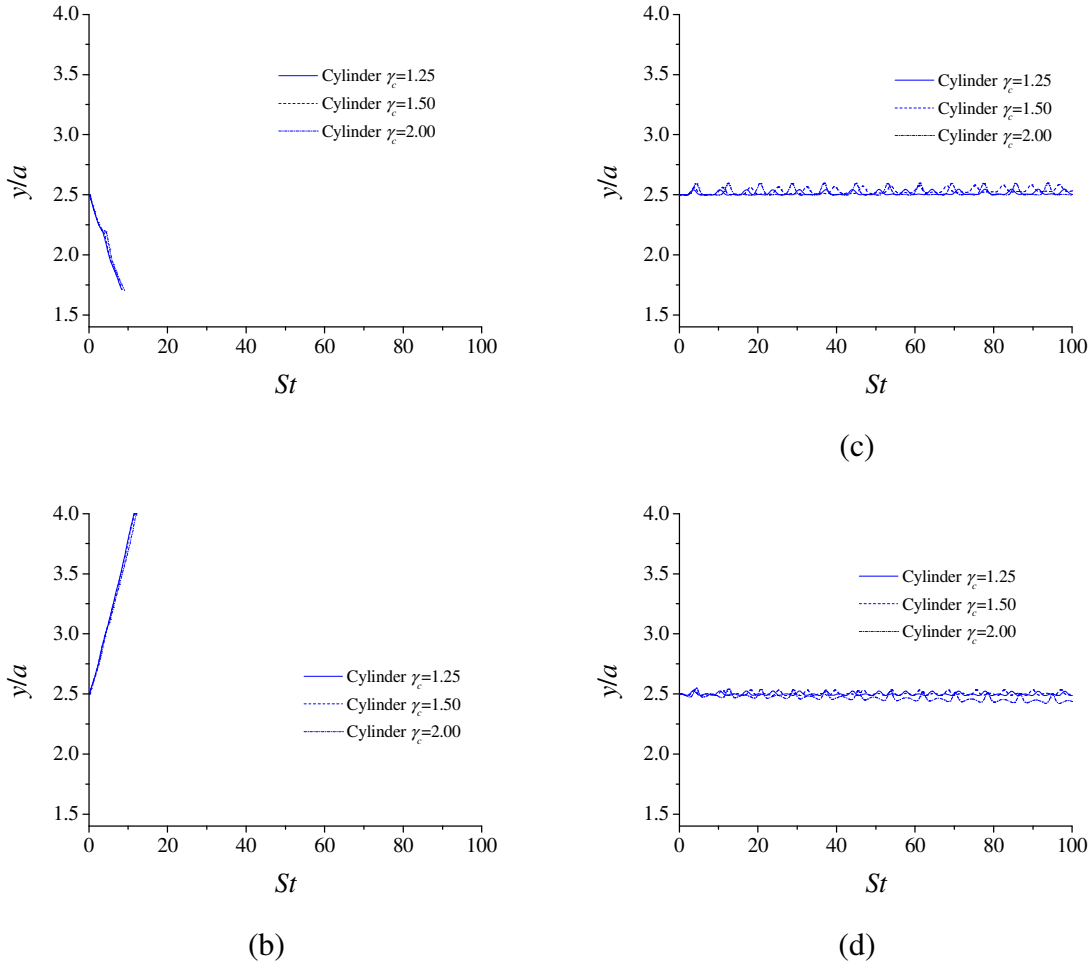

Fig. 32: The trajectory of cylindrical particles in a linear laminar flow with initial conditions (x_0/a, $u_0/(Sa)$, y_0/a, $v_0/(Sa)$, θ_0, Ω_0/S) = (0, 0, 2.5, 0, $\pi/2$, 0) for fixed shear rate in the presence of gravitational force (G=1, St_a=1)
(a) horizontal capillaries with gravitational force toward the wall
(b) horizontal capillaries with gravitational force away from the wall
(c) vertical capillaries with gravitational force along the flow direction
(d) vertical capillaries with gravitational force against the flow direction

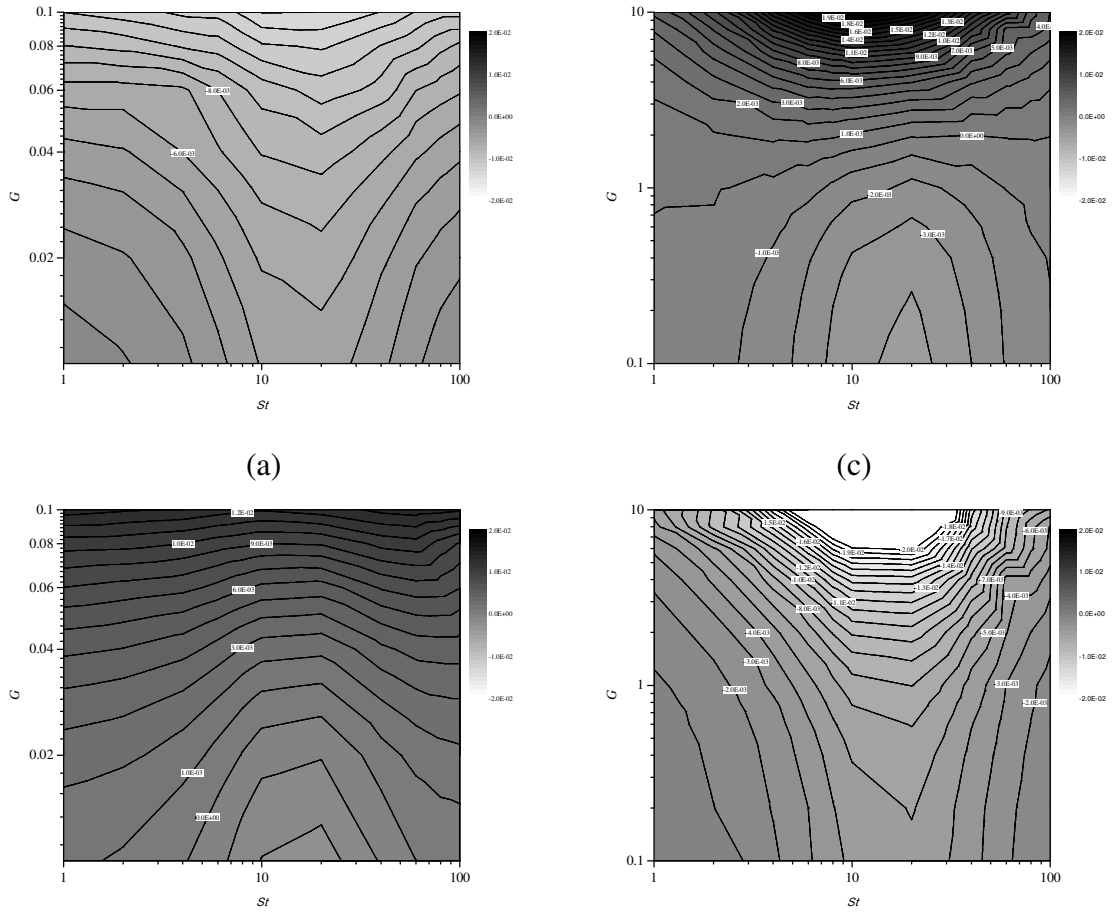

Fig. 33: Contour plots of the normalized drift velocity for ellipsoidal particles (γ_e =0.2) with initial conditions $(x_0/a, u_0/(Sa), y_0/a, v_0/(Sa), \theta_0, \Omega_0/S)$=(0,0,2.5,0,π/2,0). (a) gravitational force to the wall direction, (b) gravitational force out of wall direction, (c) gravitational force toward the flow direction and (d) gravitational force opposite to the flow direction

2.5.2 Combined effect of shape, gravity and Stokes number

Contour plots for the lateral drift velocity have been generated for the ellipsoidal particles with γ_e=0.50 (Fig.33) and the discoidal particles with γ_d=0.20 (Fig 34). For a given Stokes number and dimensionless buoyancy parameter *G*, the drift velocity can be easily derived from the contours as a function of the orientation of the gravitational force

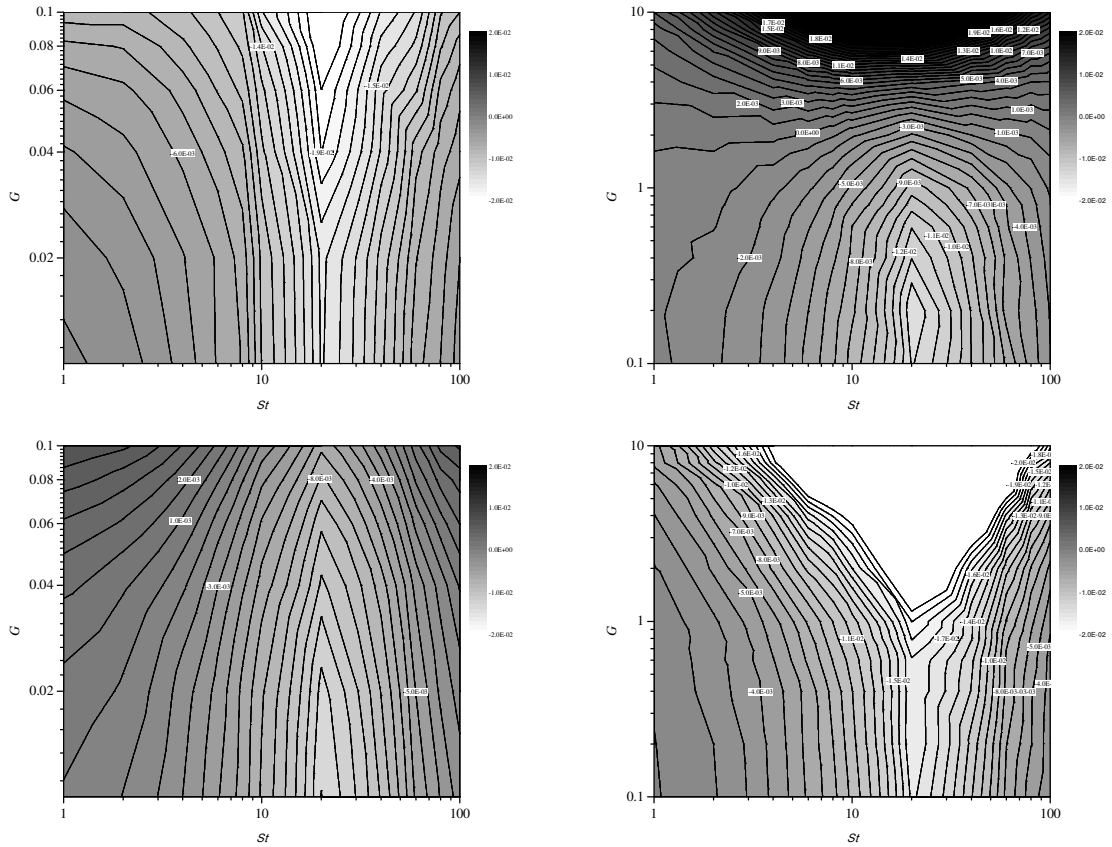

Fig. 34: Contour plots of the normalized drift velocity for discoidal particles (γ_d =0.2) with initial conditions $(x_0/a,u_0/(Sa),y_0/a,v_0/(Sa),\theta_0,\Omega_0/S)$=(0,0,2.5,0,π/2,0). (a) gravitational force to the wall direction, (b) gravitational force out of wall direction, (c) gravitational force toward the flow direction and (d) gravitational force opposite to the flow direction

with the flow. The contour plots clearly show that as St_a and G increase, the drift velocity increases up to a maximum which occurs again for St_a of about 20.

2.5.3 Consideration of actual particle drug carrier

In the gravitational field, the maximum margination velocity occurs for St_a= 10 or 20 depending on the particle shape. Also, for $St_a \leq 0.1$, margination can only be achieved with the external forces. It is then interesting to estimate the characteristic values for St_a and G for different applications and particle types. In the blood microcirculation, platelets

are accumulated within the cell free layer, a region close to the vessel walls where the concentration of red blood cells, the most abundant cells in blood (Aarts et al., 1998). Through intravital microscopy studies it has shown that the thickness of the cell free layer can be up to a few tens of microns in the micro-circulation (Kim et al., 2007). Recently, a computational fluid dynamics simulation revealed that (AlMomani et al., 2008) the platelets accumulation the wall is not mainly due to collision or volumetric exclusion by the red blood cells at the core region but hydrodynamic forces. Considering platelets as a practical example, ellipsoidal particles with aspect ratio 0.50, semi major axis of 5.0 μm (equivalent radius = 4.6 μm), and approximate density of platelets as that of water ($\rho_p \approx$ 1000 kg/m^3), under relatively low wall shear rates condition (S = 0 to 10^3 s^{-1}), the Stokes number would range from St_a = 0.0 to 0.02; at relatively higher wall shear rates (S = 10^3 to 10^4 s^{-1}), the Stokes number would increase to St_a = 0.02 to 0.2; and eventually for pathological levels of wall shear rates ($S > 10^4$ s^{-1}), St_a would be larger than 0.2. For St_a = 0.2 (S = 10^4 s^{-1}), the drift velocity of the platelet would be larger than 1 μm/sec ($v_d/Sa \approx 10^{-4}$). These data supports the hypothesis of AlMomani et al., 2008 where platelets margination has been mainly associated with the hydrodynamic forces exerted over the cells. Also, when considering stenotic vessels with large S ($> 10^0$ s^{-1}), the continuous accumulation of platelets at the vascular striction could be explained within the context of hydrodynamic margination (Nesbitt et al., 2009).

From the definition of the Stokes number ($St_a = \rho_p a^2 S / \mu$), it increases linearly with the particle density ρ_p and wall shear rate S and with the square of the particle size (a^2). Then, for sub-micrometer and nanometer particles, margination within the microcirculation cannot be achieved by changing particle shape in the absence of external forces. Also, it can be easily verified that for silica ($\rho_p \approx$ 2000 kg/m^3), iron oxide ($\rho_p \approx$8000 kg/m^3) and gold ($\rho_p \approx$ 18000 kg/m^3) particles, under normal hemodynamic

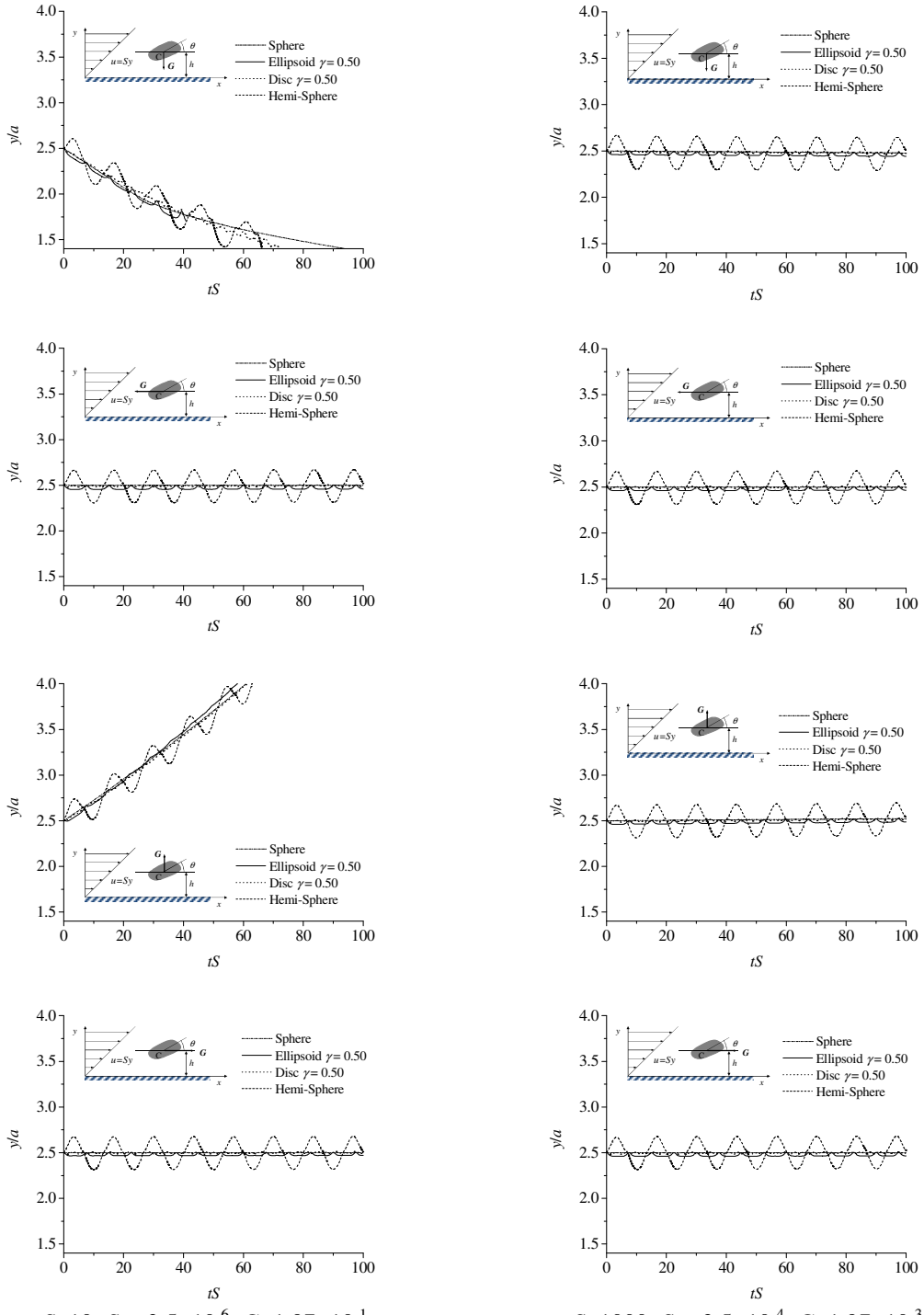

S=10; St_a=3.5×10^{-6}, G=1.97×10^{-1} S=1000; St_a=3.5×10^{-4}, G=1.97×10^{-3}

Fig. 35: The trajectory of silica SiO_2 particles with different shape in a linear laminar flow with initial conditions (x_0/a, $u_0/(Sa)$, y_0/a, $v_0/(Sa)$, θ_0, Ω_0/S) = (0,0,2.5,0,π/2,0) in the presence of gravitational force.(The inset shows the orientation of G with respect to the flow).

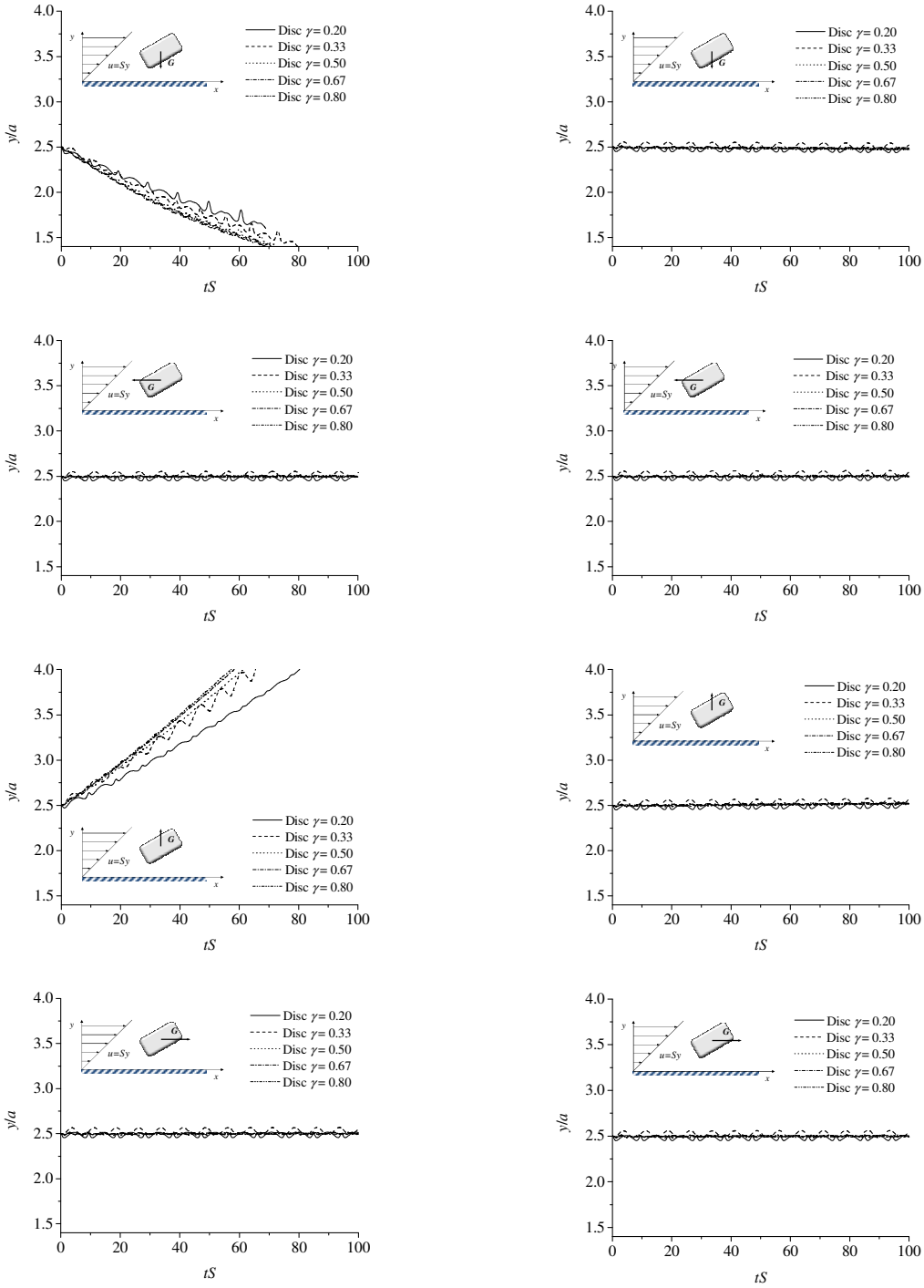

S=10; St_a=3.5×10^{-6}, G=1.97×10^{-1} S=1000; St_a=3.5×10^{-4}, G=1.97×10^{-3}

Fig. 36: The trajectory of discoidal silica SiO2 particles with different γ in a linear laminar flow with initial conditions (x_0/a, $u_0/(Sa)$, y_0/a, $v_0/(Sa)$, θ_0, Ω_0/S) = (0,0,2.5,0,π/2,0) in the presence of gravitational force.(The inset shows the different orientation of G with respect to the flow)

conditions ($S = 10^3$ s^{-1}), the minimum equivalent radius for margination without external forces ($St_a = 0.1$) would be 7, 3.5 and 2 μm, respectively. It can then be observed that, in the microcirculation, non-spherical particles oscillate around their original streamline without a lateral drift.

Porous nano/micro silica particles are one of the strongest candidates for potential drug carrier (Lasic, 1996 and Ren and Tilly, 2007). To see the effect of hydrodynamic condition on the porous nano particle near the wall, in Fig. 35 and Fig. 36, a porous silica particle (ρ_p = 1500 kg/m^3: 50% porosity) with an effective radius of 500 nm in two different hemodynamic conditions is considered: in the physiological shear rates of $S=10^3$ s^{-1}, $St_a= 3.5\times10^{-4}$ and $G=1.97\times10^{-3}$; and in the pathological shear rates of $S=10$ s^{-1}, $St_a = 3.5\times10^{-6}$ and $G=1.97\times10^{-1}$. Under physiological conditions, the effect of the inertial and gravitational forces is negligibly and no lateral drift velocity is observed (no margination). Notice that this characteristic would be even more for lighter particles materials, such as, polymer and lipid based particles. However, under pathological condition as the tumor microcirculation condition, the gravitational effect (G) is dominant over inertial effect, which leads to particle sedimentation, which is not because of inertial drift but of gravitational force. Again, this would be still negligible for lighter particles. These observations confirm that, in the absence of external forces, nanometer sized non spherical particles within the microcirculation can only oscillate around their trajectory, whatever shape it is. However, it should be investigated the effect of size and shape because geometrical factors play an important role in adhesion (Decuzzi and Ferrari, 2006) and internalization (Decuzzi and Ferrari, 2008), which are major procedures in particle delivery, in both of the nano and micro scale.

Within the pulmonary airways, the trajectory of particle is different from the particle behavior in the blood vessel. The flow in the pulmonary has the lower viscosity

($\mu \approx 10^{-5}$ kg/ms) and density ($\rho_f \approx 1$ kg/m^3) compared to aqueous solutions, and has the larger wall shear rate, ranging from $S=10^4$ and 10^5 s^{-1}. These flow properties lead to larger Stokes number. In this case, the minimum equivalent radius R_{eff} for margination, in the absence of external forces, of solid particles with a density, ρ_p = O(3), which is equivalent or larger than water, is about 100 nm for $S=10^5$ s^{-1}. Compared to the blood microcirculation, non spherical particles can marginate more easily. For example, the range of Stokes number of inhaled asbestos fibers (ρ_p = 2500 kg/m^3) in the few micrometers can be between $St_a = O(1) - O(10)$, which is the maximum lateral drift velocity has been predicted. It implies that the margination is one of the important mechanisms for the fibers to adhere to the walls of the alveoli and the subsequent translocation into the pulmonary circulation by crossing the alveolo-capillary membrane (Giddings, 1993).

2.6 Summary

In this chapter, effect of size, flow condition (different St_a), shape (sphere, hemi-sphere, disc and cylinder) and external force (gravitational force) on trajectory of particle in linear shear flow has been discussed. Even in the physiological shear stress rage (0.1-2.0 Pa) (Taylor et al., 2002, Reneman et al., 2008, Stroeva et al., 2007 and Misra et al., 2006), for example, large artery, arota and vein, small particle which has diameter less than 500nm, without external force, it is hard for the particle to marginate with shape effect. To take advantage of inertial margination, particle size should be larger than 2um or density of particle material should be very heavy, for example, iron oxide or gold particle. In terms of flow condition, to see the margination in blood flow, St_a should be larger than, at least, 0.2.

Chapter 3: Particle adhesion dynamics in micro fluidic chamber

3.1 Introduction

Particle or cellular adhesion on the vascular endothelial cell is one of the important processes in cancer metastasis or treatment. Some of famous examples of adhesion are particular adhesion of drug carrier in drug delivery process, leukocyte adhesion on the site of tissue injury, platelet adhesion in the process of atherosclerosis and cancer cell adhesion in metastasis. The size of particle in the above processes is varying in wide range from nanometer scale (nano/micro sized particle delivery for therapeutic and/or imaging application ~10nm-1μm) to a few tens of micrometer scale (platelet ~ 2μm; leukocyte ~7-10μm; metastatic cancer cell ~20μm). The particle under flow experiences series of process called attachment, rolling, firm adhesion and detachment according to the environmental condition of flow. To analyze the theses complex steps of processes, various theoretical and experimental research tools have been utilized to reveal the effect of particle properties, such as, size, shape and surface properties (for example, surface charge, ligand density, PEG coating, etc).

The very fundamental but powerful tool to analyze the complex nature of particular or cellular adhesion is mathematical modeling of the adhesion strength. In 1967, Goldman et al had analyzed the drag and torque on the adhered particle induced by the hydrodynamic interaction in the ideal linear shear flow (Goldman et al, 1967). The particle adhering on the substrate (or endothelium) can be assumed in the linear shear flow because of the small size of particle. The force exerted on the particle can be reasonably assumed to be the dislodging force on the particle. On the other hand, particle should have favorable interacting force, such as, van Der Waals force and ligand-receptor interaction, etc which are the adhesive forces. In the most of targeted drug carrier

delivery, ligand-receptor interactions would play an important role in particle-substrate interaction. For the particle to remain adhered, the adhesive force between the particle and the substrate in the flow should be balanced or stronger than the hydrodynamic dislodging force.

Cozens-Roberts et al. (Cozens-Roberts et al., 1990) and Hammer and Lauffenburger (Hammer and Lauffenburger, 1987) introduced the probabilistic behavior of adhesion between particle (or cell) and surface (or endothelium). Two situations; cell attachment in the absence of fluid stress and cell detachment in the presence of fluid stress were investigated. This work is mathematical prediction of particle adhesion by analyzing the probability of particle-surface interaction based on the interaction mechanisms of hydrodynamic dislodging force and ligand-receptor interaction. Especially, the critical shear rate was introduced to measure the relative strength of adhering force in a flow. The critical shear rate was defined as the shear rate that 50% of adhered particles are detached from the substrate by hydrodynamic force. Shinde Patil et al. has experimentally proven the effect of size on the adhesion mechanism using relatively large size particle (2-20 μm) coated with recombinant P-Selectin under shear flow (Shinde Patil et al., 2001). The effect of size and shape (sphere and oblate ellipsoid) is again confirmed by Decuzzi and Ferrari through their analytical work (Decuzzi and Ferrari, 2006). In their works, it has been shown that the adhesive strength can be expressed as a function of particle size (diameter), shape (aspect ratio) and surface property (ligand density). Also it has been proven analytically that there exists optimal size for every aspect ratio in terms of adhesion probability. Recently, the effect of particle and vessel size, existence hematocrit, that is, hemodynamic effect, has been investigated experimentally using micro flow chamber system (Charoenphol et al. 2010). In the flow with hematocrit, it has been shown that for small size particle, size does not affect

significantly on the adhesion dynamics, however, for relatively large size particle corresponding to the hematocrit size, the number of particle adhering on the substrate is increased due to the exclusion from the red blood cell layer induced by the collision between the particle and red blood cell. Consequently, in case of spherical particle, 2-5 μm in diameter is suggested as the optimal size in terms of adhesion in the presence of hematocrit in the flow.

Most of the previous studies focus on the specific interaction in relatively large shear rate and large particle size as a candidate for the targeted particle delivery on the inflamed cell. In the mathematical modeling, ligand-receptor interaction is assumed as major adhesive interaction mechanism. Especially, the kinetics of probability of adhesion has been estimated based on the ligand-receptor interaction. Also, in the experimental works, the particles were conjugated with certain type of receptor, for example, P-Selectin (Shinde Patil et al., 2001), sialyl Lewis^a (Charoenphol et al. 2010), and the substrate was covered with endothelial cell. In terms of flow condition, particle adhesion is expected to occur at the endothelial cell in a relatively small vessel. In other words, if the particle is designed to target to the cancer cell, the final target for particle to localize would be the newly generated vessel through angiogenesis, which wrap up the cancer cell. Those vessels are relatively small in size and have low flow rate. Therefore, the examination suitable for actual condition should be performed in that smaller characteristic particle size should be studied and wider flow rate range, especially low flow rate, also be considered.

In this study, the effect of particle size in the flow will be investigated in the theoretical and experimental framework. The particle size (d) will be from 0.72μm to 10μm and the shear rate (S) will be from 10 to 100, will be considered. The theoretical

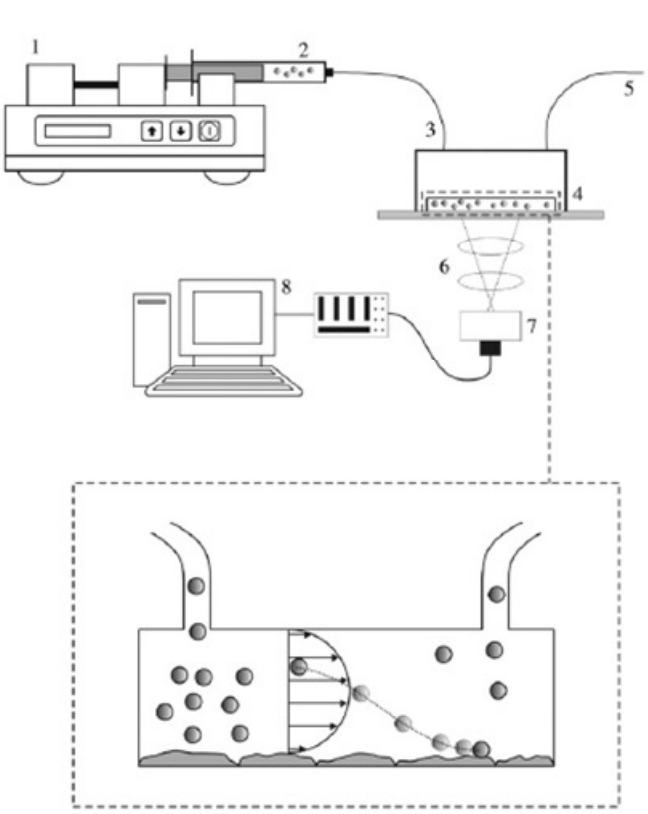

(a)

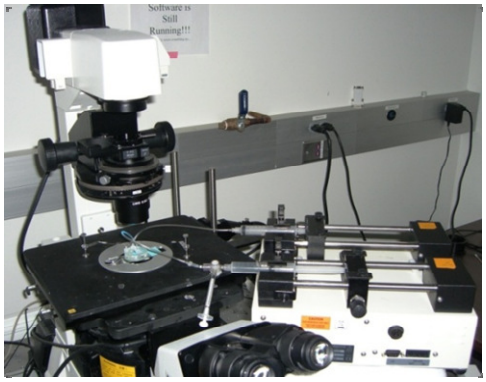

(b)

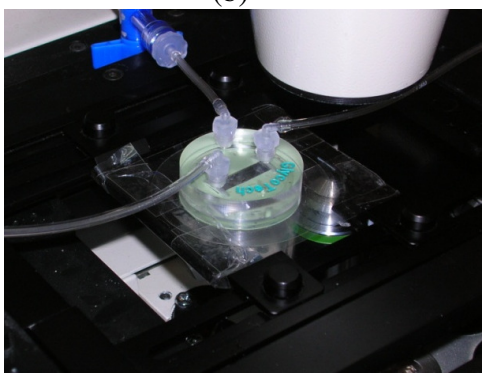

(c)

Fig 37: (a) Schematics of experimental apparatus; 1) Syringe pump, 2) Syringe with suspended particle, 3) Inlet tubing, 4) Parallel plate flow chamber, 5) Outlet tubing, 6) Microscope, 7) Digital camera and 8) Computer, (b) photos of microscope and (c) installed flow chamber

prediction will be proven by the experimental measurement of the number of particle per unit area on the collagen coated substrate and ovarian endothelial cell.

3.2 Micro fluidic chamber set-up for the in-vitro characterization of particle dynamics

A parallel plate flow chamber (Glycotech, Rockville, MD) was used for the in-vitro adhesion experiments. It consists of Plexiglass flow deck with two holes (inlet and outlet). The flow deck is attached to a 35 mm borosilicate cover slip. A silicon gasket was installed between the flow deck and the cover slip to make the flowing region. The flow

chamber was connected to a syringe pump (Harvard apparatus, MA) through plastic tubing with an inner diameter of 0.05 in. The channel is 5 mm in width (w), 20 mm in length (l) and 0.01 in (254μm) in height (h). The aspect ratio of channel (h/w) is about 0.05 which is wide enough not to be disturbed by the wall and to assume 2D Poiseuille's flow in the middle of the flow chamber. After assembling the flow chamber and the pump, the system was placed on the stage of an inverted fluorescent microscope. Experiments were performed at room temperature at 25°C. Images were capture at regions of interested chosen in the middle of the channel along the flow direction. The particle motion was observed using a ×20 dry microscope objective, which gives the area of the image is 0.413×0.413 (mm^2). With such a magnification, fluorescence labeled micrometer or sub-micrometer particles, ranging from 0.75μm to 6.0μm in nominal diameter, were easily observed using fluorescent microscopy (Nikon TE-2000). After counting the number of particle in the area of interest, the total number was normalized by the area of interest. The fluorescent microspheres were injected with certain concentration for designed shear rate. The shear rate of 2D Poiseuille's flow can be easily determined through following formula:

$$S = \frac{6Q}{h^2 w} \tag{13}$$

then, shear rate can be controlled by the flow rate of syringe pump. At the time when the desired number particles are injected, syringe pump is stopped. The image of particle adhesion on the surface was saved to a computer for storage using a Nikon DQC-FS digital camera. The image data were exported as TIF files into ImageJ, a freeware

Table 2 Size and ζ-potential of microsphere

Carboxylated polystyrene					
$d_{Nominal}$ (μm)	0.75	1.00	2.00	4.50	6.00
d_{Actual} (μm)	0.72	0.97	1.83	4.90	6.60
ζ-potential (mV)	-61.67±0.8	-87.28±3.1	-79.15±4.0	-82.19±7.0	-52.42±0.4
Plane silica (SiO_2)					
$d_{Nominal}$ (μm)	1.00	1.50	2.50	3.00	5.00
d_{Actual} (μm)	1.34	1.55	2.63	3.24	4.89
ζ-potential (mV)	-46.25±3.6	-20.01±1.9	-20.56±2.1	-31.95±1.6	-33.54±2.7

software from NIH (http://rsb.info.nih.gov/ij/) for the following image processing and the particle counting within the region of interest.

3.3 Measurement of critical shear rate for spherical particles on a collagen layer

Polystyrene fluorescent microspheres (Fluoresbrite® YG Carboxylate Microspheres, Polysciences, PA) with different sizes, namely 0.75, 1.00, 2.00 , 4.50 and 6.00, 10.00 μm (nominal diameter) and plain silica particle, SiO_2, (Silica Microspheres, Polysciences, PA) with different sizes, namely 1.00, 1.50, 2.50, 3.00 and 5.00 μm (nominal diameter) were purchased. For the smaller sized particle (d < 3 μm), the diameter and number of particles were measured by Multisizer 4 Coulter Counter and size analyzer (Beckman Coulter, CA) with a 20 μm aperture size. Particles were suspended in the balanced electrolyte solution (ISOTON II Diluent, Beckman Coulter Fullerton, CA) and counted. However, since the large size of particles cannot be counted with that small size of aperture, hemocytometer (Hausser, Horsham, PA) was used to characterize the number of larger particle (d > 4.5μm) . The actual size and physico-

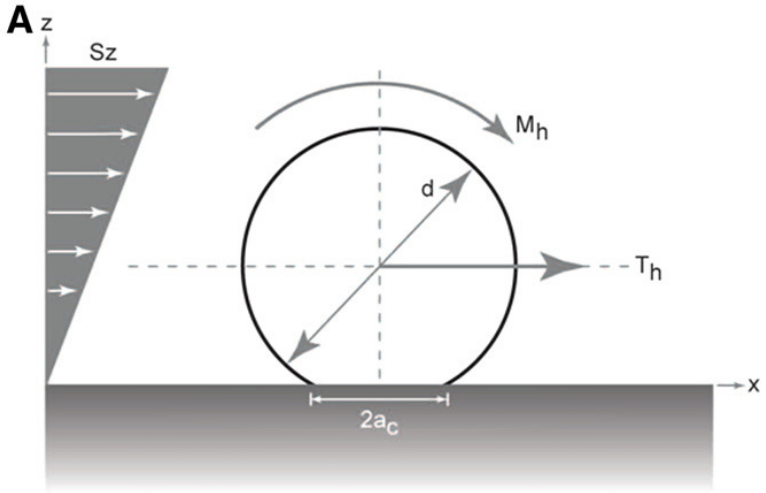

Fig. 38: Sketch of the geometry and forces exerted over a particle adhering to the chamber substrate under flow (from Decuzzi et al., 2010)

chemical properties of the particle are listed in Tab.1. ζ-potential has been measured by ZetaPALS (Brookhaven, NY) to characterize the particle surface charge. Measured ζ-potential values of different types of particle are also listed in Table 2.

Since clean glass cover slip has relatively weak adhesion force with nano/micro particle, the borosilicate glass cover slip was prepared by coating with collagen, which is the main protein of connective tissue, type I solution from rat tail (Sigma-Aldrich Corporation, MO). The solution with a concentration of 4 mg/ml was diluted in DI water to obtain 10μg/cm^2. Sterile cover slips were kept at 4°C overnight.

The critical shear rate is measured to verify the experimental system's reliability including flow chamber, syringe pump and particle. The critical shear rate is defined as the shear rate that 50% of adhered particles are detached from the substrate by hydrodynamic force (Cozen Roberts et al., 1990). By controlling flow rate of syringe pump, the hydrodynamic force is applied on the particle adhered on the substrate in the μ-fluid chamber (Fig. 37). When the non-specific adhering force is balanced or less than hydrodynamic force, the particle can be detached. By measuring the number of particle

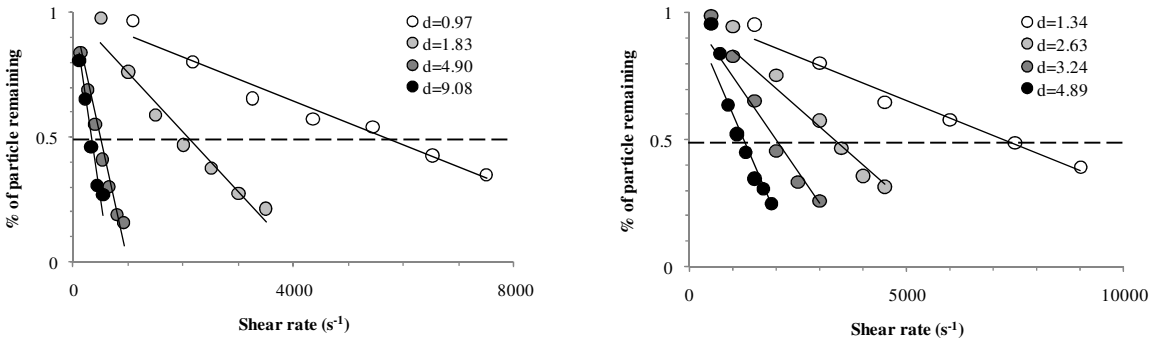

(a) (b)

Fig. 39: The plot of number of particle remaining over shear rate (a) carboxylated polystyrene microsphere and (b) silica (SiO_2) microsphere

remaining on the substrate, the critical shear rate can be measured easily. Briefly, the particles are distributed over the substrate with very low flow rate. In this study, to distribute the particle, initial shear rate set to be 10 (s^{-1}). Averagely about 50-100 particles are distributed depending on the particle size. Once the particle is evenly distributed over the substrate, the shear rate is increased in stepwise manner, also depending on the particle size. As the particle size decreases, the hydrodynamic dislodging force on the particle decreases due to small cross sectional area that are affected by the flow. The difference of stepwise increment of shear rate should be increased to reach higher shear rate to detach the particle. For example, carboxylated polystyrene particle with 1μm in diameter requires the extremely high shear rate to detach 50% of particle adhered and then the maximum shear rate was about S=6000-7000 (s^{-1}). On the other hand, with relatively large particle (d=10μm for carboxylated polystyrene particle), only about S=500-600 (s^{-1}) could be enough to get critical shear rate. The shear rate was increased every 2 minutes and the images have been recorded with .avi file in every 5 second through the computer. The number of particle was normalized with initial number of particle then using linear fit of the remaining fraction of particle, the critical shear rate was determined.

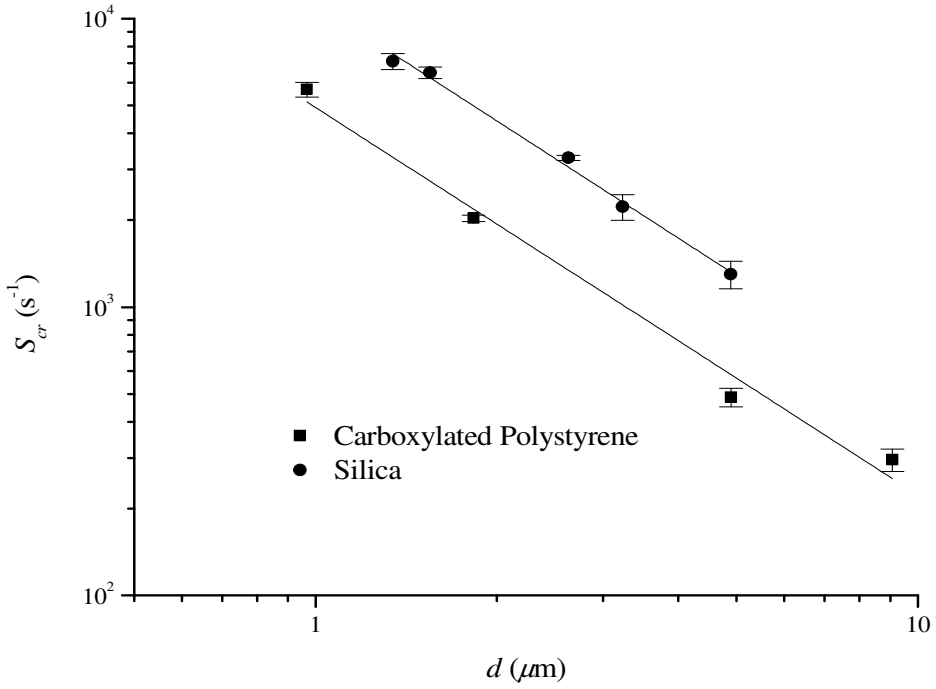

Fig. 40: Variation of the critical shear rate at the wall S_{cr} as a function of the particle effective diameter d measured in flow chamber experiments. The experimental variation of the critical shear stress with the particle diameter

Two types of particle have been used to find the critical shear rate. Silica microsphere (d_{nominal}=1.00, 1.50, 2.50, 3.00 and 5.00) and carboxylated polystyrene microsphere (d_{nominal}=1.00, 2.00, 4.50, 10.00) was used as shown in Table 1. Both of particles show negatively charged surface ζ-potential. Fig. 39 shows the fraction of remaining particle as a function of applied shear rate. Assuming the fraction of particle remaining is linearly decreased with the increase of the shear rate, the critical shear rate of each type of particle for different size can be easily estimated.

In vitro adhesion experiments have been performed to quantify the strength of adhesion of the silica beads to a biological substrate (Collagen, type I solution from rat tail (Sigma-Aldrich Corporation, MO)). In a parallel plate flow chamber, four or five

bead sizes for each types of particle have been tested, namely, 1.0, 2.0, 4.50 and 10.00 μm for carboxylated silica particle, 1.0, 1.5, 2.5, 3.0 and 5.0 μm for silica particle, and the critical shear stress was measured as a function of the bead size. A non-linear regression analysis of the data (Fig. 40) showed the existence of a scaling relationship between the critical shear stress and the particle size as $S_{cr} \propto d^{-1.349}$ (R^2=0.994) for silica particle $S_{cr} \propto d^{-1.343}$ (R^2=0.987) for carboxylated polystyrene particle. This confirms that the strength of adhesion of the spherical beads reduces as their diameter increases, making therefore firm adhesion less likely for the larger particles.

3.4 *In vitro* measurement of particle marginating and adhering on a biological layers

3.4.1 Effect of particle size

3.4.1.1 Mathematical prediction of particle-substrate adhesion

To execute its diagnostic and/or therapeutic mission, an intravascularly injected particle has to approach to the vessel wall which is the target cell and then be firmly adhered. During this process, particle experiences diverse micro environmental conditions, such as, interaction with comparable sized molecule (ex. red blood cell, macrophage, etc), influence of the geometrical and physiological condition of the particle, surface property of the target cell, hydrodynamic/hemodynamic condition in the vessel, etc. The size of blood vessel varies from a few micrometers to centimeter scale, that is, particles are flowing in wide range of Reynolds number which is from turbulent to Stokes flow. The vessel around tumor or diseased cell is relatively small but has irregular size and shape since it is newly created through angiogenesis process. Especially, irregular size and shape of vessel makes particle undergo wide range of hydrodynamic

condition. Most of adhesion process is expected to happen at this complex vessel but to have enhanced efficacy of the particle adhesion. Therefore, the effect of hydrodynamic condition on the dynamics of particle including margination and adhesion should be clarified to understand whole process of particle delivery.

To analyze particle adhesion process to the substrate, very simple mathematical model has been developed by several research groups (McQuarrie, 1963, Piper et al, 1998 and Decuzzi and Ferrari, 2006). At the very proximity of the vessel wall, where particle adhesion is expected to occurs, flow around the particle can be assumed linear shear flow due to its micro/nano scale size and low flow rate through small capillary. In this study, an investigation of non-specific adhesion dynamics of spherical particle will be carried out using simple mathematical modeling of interactions between the particle and the substrate including hydrodynamic interaction to the particle. Even though a lot of research groups are currently investigating non-spherical particle as a drug carrier, it is of interesting to study the behavior of spherical particle since it is still most popular particle shape in terms both of the research and application purpose. Additionally, the most advantageous feature of spherical particle is that it is relatively simple to produce and analyze due to its simple geometry.

To simulate the particle surface interaction, the probability of adhesion developed by Decuzzi and Ferrari (Deccuzi and Ferrari 2006) has been utilized in this study. They developed the probability of adhesion assuming that the receptor-ligand interaction is the main adhesion mechanism. A probability of adhesion can be defined as following to the Decuzzi and Ferrari. They used the probabilistic kinetic formulation of McQuarrie (Mcquarrie, 1963) and Piper et al. (Piper et al., 1998) assuming the limiting case of small surface density of receptor and ligand interaction. In this case, the steady state probability of adhesion (P_a) has a form of

$$P_a = m_r m_l K_a A_C \exp\left[-\frac{\lambda f}{k_B T}\right] \tag{14}$$

where K_a is the association constant at zero load of the ligand–receptor pair; A_c is the area of interaction between the particle and the substrate; f is the force per unit ligand–receptor pair; λ is a characteristic length of the ligand–receptor bond generally of the order of 1Å; and k_B is the Boltzman constant; and T is the temperature.

On the adhered particle in the flow, the particle experiences hydrodynamic drag force, F, and the torque, T, which tend to break the bonding between the particle and substrate. This hydrodynamic interaction has been analytically calculated by Goldman et al. (Goldman et al., 1967[a,b]). The hydrodynamic interaction on the particle attached on the substrate can be expressed as

$$\mathrm{F} = 6\pi a^2 \mu S F^S \text{ and } \mathrm{T} = 4\pi a^3 \mu S T^S \tag{15}$$

where $F^S \approx 1.668$ and $T^S \approx 0.944$ for sphere. Then total dislodging force per unit contact area and unit receptor on the adhered particle is

$$\frac{F_{dis}}{m_r A_C} = \frac{F}{m_r A_C} + \frac{2T}{m_r A_C r_0} \tag{16}$$

where r_0 is radius of intersection of sphere at separation distance h_0. The radius of intersection of sphere can be defined from the expression of area of intersection. The area of interaction A_C can be defined as πr_0^2 where r_0 is the radius of the circular section of the

sphere at separation distance h_0. Since the intersection radius of sphere at a z plane can be given by

$$r(z) = a\sqrt{1 - \left(\frac{z}{a}\right)^2} \tag{17}$$

hence, the area of interaction in this case can be estimated by

$$A_c = \pi {r_0}^2 = \pi a^2 \left(1 - \left(1 - \frac{h_0}{a}\right)^2\right) \text{ and } r_0 = a\sqrt{1 - \left(1 - \frac{h_0}{a}\right)^2} \tag{18}$$

and it also has been assumed that total number of ligand is larger than the total number of receptor (N_l>N_r).

From the definition, f in Eq. (14) can be formulated as

$$f = \frac{F_{dis}}{m_r A_C} \tag{19}$$

Since current experiment is done for the non–specific interaction between the particle and the substrate, overall expression for the probability of adhesion is not exactly what we are looking for. Since the non-specific interaction is considered, all the variables expressed in Eq. (14) cannot be used as it is. Instead of using the previous expression for probability of adhesion, to fit the experimental data, we can parameterize the Eq. (14) as a function of size of particle. By combining equations above, the probability of adhesion can be parameterized and expressed as

$$P_a = \alpha d^{\varepsilon} \exp[-\beta f(d) S] \tag{20}$$

$f(d)$ represent the ratio of dislodging force by the hydrodynamic interaction and contact area between the sphere and substrate. Fitting parameters, α and β are defined as

$$\alpha = \pi m_l m_r K_A^o C,\ \beta = \frac{\lambda \mu}{\mathrm{k_B T} m_r} \tag{21}$$

where, $C=A_c/\pi d^2$.

There are enormous ways to model the effect of size on the ratio of dislodging force to the contact area ($f(d)$). Dr. Decuzzi suggested the following expression to make this model simple.

$$P_a = \alpha d^{\varepsilon} \exp\left[-\beta\left(1 + \lambda d^{\delta}\right) S\right] \tag{22}$$

3.4.1.2 Comparison of mathematical prediction with flow chamber experiment

In vitro flow chamber system is used to characterize the adhesion of particle on the biological substrate. The borosilicate glass cover slip was prepared by coating with collagen, type I and ovarian endothelial cell cultured cover slip was prepared. The number of particle per unit area normalized injected particle volume ($\#_{inj}\frac{4}{3}\pi\left(\frac{d}{2}\right)^3$) as a function of particle size (Fig. 41 (a)) and a function of shear rate (Fig. 41 (b)) is presented. The dotted lines are the power regression lines for each shear rate (S=10, 50, 75 and 90). Regression equations for each shear rate in Fig. 41(a) are $\#/AV = 262.2d^{-1.609}$ ($R^2 = 0.9997$) for S=10, $\#/AV = 51.436\ d^{-2.52}$ ($R^2 = 0.9991$) for S=50, $\#/AV = 38.013\ d^{-2.548}$

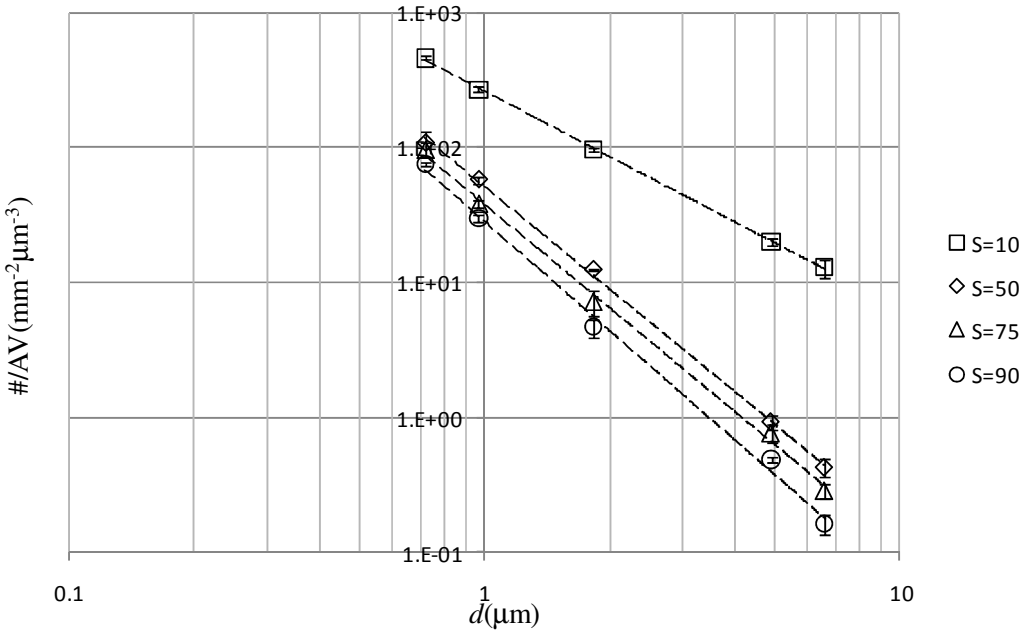

(a)

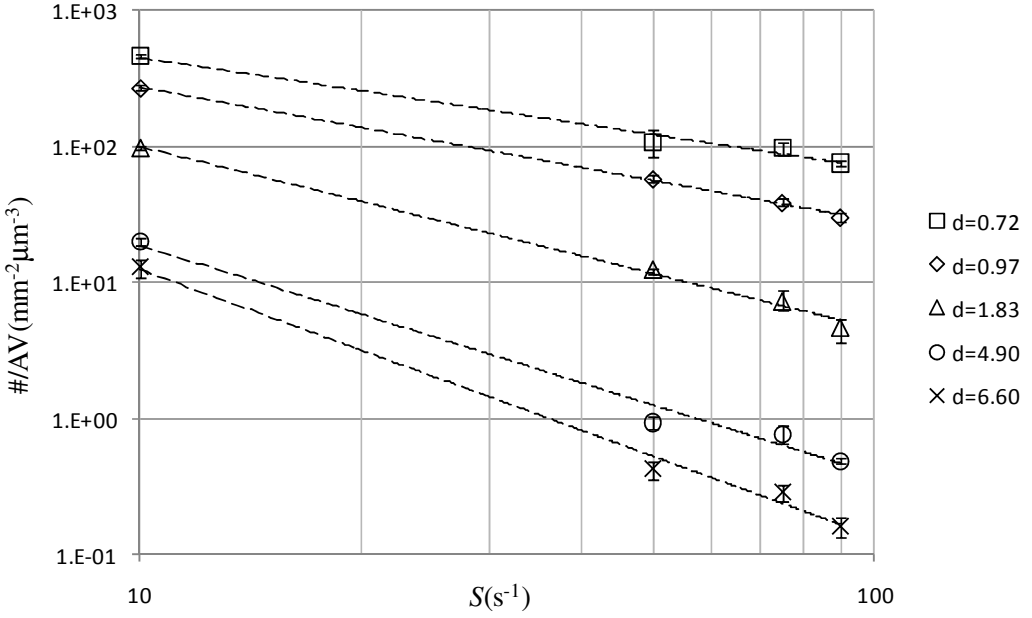

(b)

Fig. 41: Number of particle adhered on the collagen coated substrate per unit area normalized total volume of particle injected as a function of (a) particle diameter and (b) shear rate.

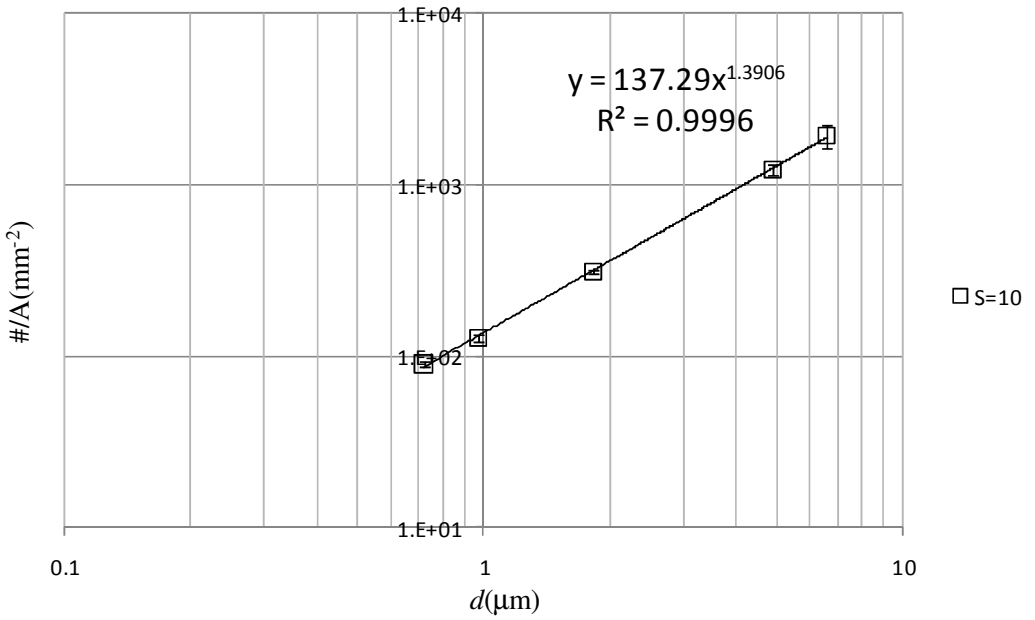

(a)

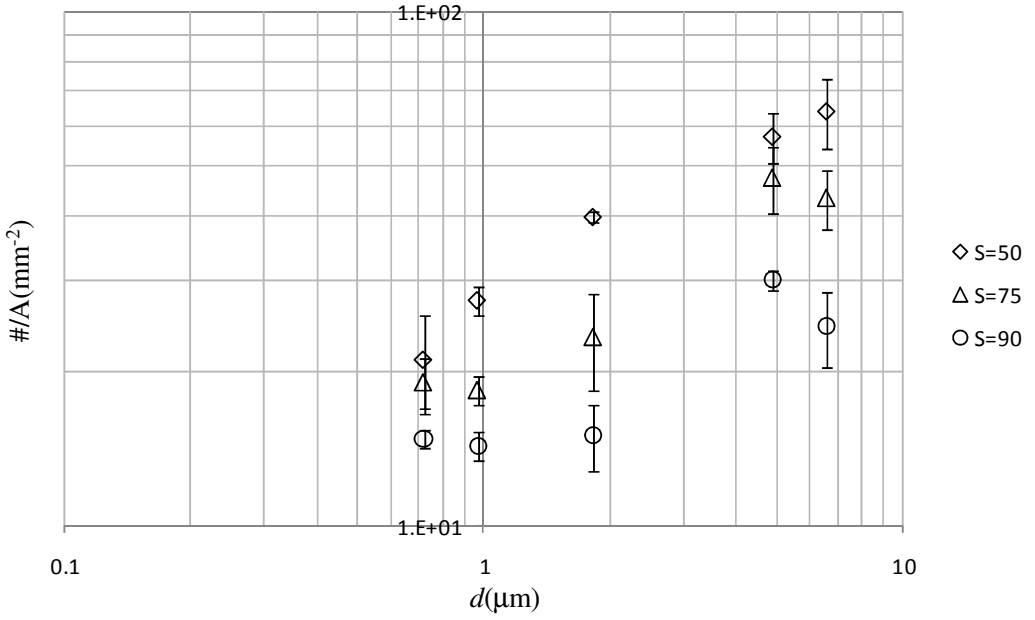

(b)

Fig. 42: Number of particle adhered on the collagen coated substrate per unit area as a function of particle diameter (a) *S*=10 and (b) *S*=50, 75 and 90

(R^2 = 0.9977) for S=75 and $\#/AV = 28.343\ d^{-2.684}$ (R^2 = 0.9966) for S=90, respectively. In Fig. 41(b), the scaling law for each size of particle as a function of shear rate are $\#/A = 2901\ S^{-0.81}$ (R^2 = 0.9867) for d=0.72, $\#/A = 2614.9\ S^{-0.982}$ (R^2 = 0.9988) for d=0.97, $\#/A = 2161.5\ S^{-1.337}$ (R^2 = 0.9951) for d=1.83, $\#/A = 897.02\ S^{-1.68}$ (R^2 = 0.9844) for d=4.90, $\#/A = 1139.4\ S^{-1.963}$ (R^2 = 0.9927) for d=6.60, respectively. The scaling law exponent derived for the #-S are of about -1.609, -2.52, -2.548 and -2.684 for S=10, 50, 75 and 90, respectively. The exponent on scaling law decreases as shear rate increases. In other words, the effect of size is getting stronger for higher shear rate. It seems to be due to the increase of cross sectional area of spherical particle. Two things to be addressed in Fig. 41 are (1) that number of particle adhering normalized by injection particle volume on the collagen coated substrate decreases as increasing shear rate and (2) that number of particle adhering per unit injection volume increases as increasing particle size. For smaller shear rate, hydrodynamic force would be relatively smaller than adhesion force. Thus, the adhesion dominant interaction can be assumed for small shear rate. However, as the shear rate increases, the size is getting more important, because the increased area is affected by hydrodynamic force. This can be used to estimate adhesion strength for each particle size with comparison with numerical prediction.

When running the flow chamber experiment, injection concentration is fixed to be 10^6/ml. Instead of normalizing the number of particle by the injected particle volume, if the number of particle adhering per unit is plotted, an interesting phenomenon is observed. With small shear rate (S=10) in Fig. 42 (a), number of particle adhering per unit area is increasing. Especially, for S=10, the scaling law exponent is 1.391, which agrees to the critical shear rate measurement experiment result. As shown in chapter 3.4.1, scaling low exponent of *in-vitro* and *in-vivo* results is about 1.3~1.4. However, as shear rate increases, for S=75 and S=90, number of particle adhering per unit area

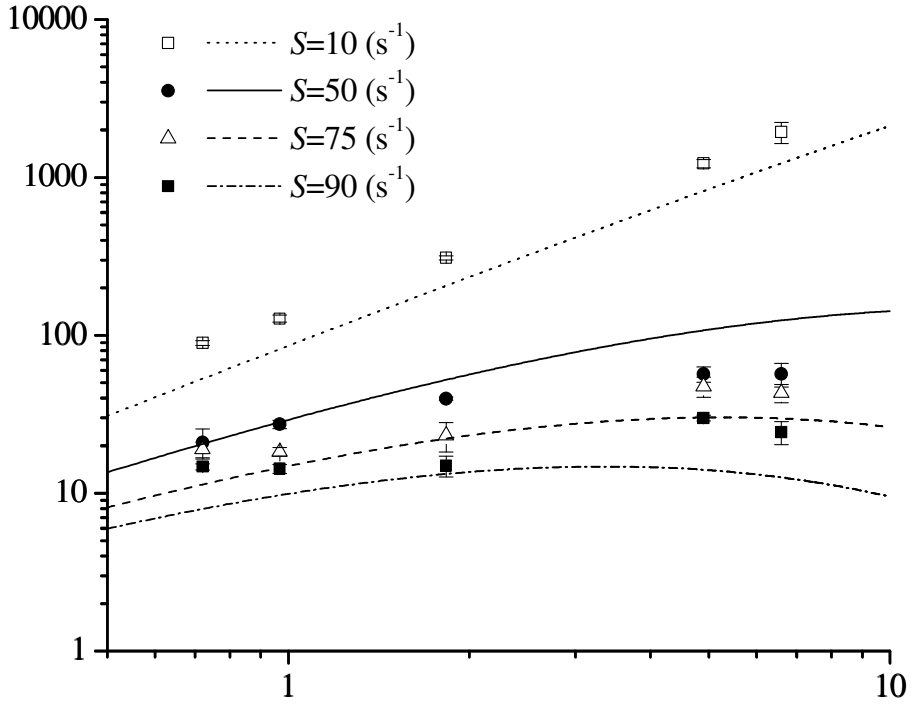

Fig 43: Comparison of mathematical prediction of particle adhesion per unit area to in-vitro micro-fluidic chamber experimental results for spherical particle with different size and different shear rate.

increases from particle diameter 0.72μm to 4.90μm but decreases for 6.60μm. Statistical analysis has been performed for number of particle per unit are between d=4.90 μm and d=6.60 μm ($p < 0.05$) for both of S=75 and S=90. This result has been compared to the mathematical prediction as described in chapter 3.2. The fitting parameters in Eq. (22) can be found by adjusting each parameter to fit to the experimental results.

Before discussing the fitting value of the parameters, it is worth to discuss ahead the physical meaning of each parameter. In Eq. (22), there are five parameters, which are α, β, γ, δ and ε. As shown in Eq. (14), is a measure of adhesion strength between the ligand and receptor. In fact, even though current experimental approach measures non-

specific interaction between the spherical particle and substrate, it is acceptable to assume that the specific adhesion strength associated with ligand-receptor interaction is related to non-specific interaction. Since the adhesion strength term, α, contains particle size as a variable, another variable related to the particle size is ε. By rearranging the term in the exponent, it can be easily verified that the expression in the exponent is linearly proportional to the shear rate and is function of polynomial of particle size (d). Assuming that second order term for size related polynomial is good enough, two more variables, δ and γ is coming out. β is ration of characteristic length of the ligand–receptor bond to the product of thermal energy, receptor density and contact area.

Fig. 43 presents the comparison of mathematical prediction of particle adhesion per unit area to *in-vitro* μ-fluidic chamber experimental results for spherical particle with different size and different shear rate. The mathematical model suggested by Decuzzi and Ferrari shows the maximum at certain particle size (or volume). Similarly, current experimental results show the maximum number of particle adhering per unit area at particle size of d=4.90μm. Assuming that the adhesion mechanism is similar between specific and non-specific interaction, the best fitting parameters can been found by comparison of mathematical model and experimental results. The fitting parameters are listed in Table 3 for current case; non-specific spherical particle interaction with collagen coated glass cover slip. Decuzzi and Ferrari (Decuzzi and Ferrari, 2006) provided physiologically relevant value of receptor density, ligand density and association constant. According to the previous study, m_r=10^{14}, m_l=10^{14} and K_a^o=10^{-10}. Based these values, α is 10^9, which is extremely large value than our fitting parameter α. However, their works focused on the specific interaction, which possibly have much more ligand density on the particle and receptor density on the cell. Since current study is focusing on the non-specific interaction, it can be assumed that effect of ligand-receptor associated

Table 3. Fitting parameters for Eq. (22) for non-specific spherical particle interaction with collagen coated glass cover slip

parameter	value
α	2.95×10^{5}
β	6.64×10^{-4}
γ	0.405
δ	1.57
ε	1.070×10^{4}

interaction is much smaller than specific interaction. Thus, in this case, it is assumed that ligand density and receptor density is two orders of magnitude smaller than specific interaction. It gives α value of

$$\alpha = \pi m_l m_r K_A^o C \approx \pi 10^{12} 10^{12} 10^{-10} C \approx 10^5 \tag{23}$$

assuming $C \approx 10^{-9}$. β also can be estimated based on the values provided in Decuzzi and Ferrari, 2006 in blood flow

$$\beta = \frac{\lambda\mu}{\mathrm{k_B T} m_r} \approx \frac{10^{-10}10^{-3}}{10^{-21}10^{12}} = 10^{-4} \tag{24}$$

With a few reasonable assumptions, it is possible to get physically meaningful parameters and the resulting fitting equation is applicable to current experimental results. Thus, the mathematical model suggested by Decuzzi and Ferrari is also valid for predicting non-specific interaction.

The ovarian endothelial cell has been provided by Dr. Sood to see the effect of size the particle adhesion. The cells are cultured on the collagen coated cover slip for three days to make the substrate fully confluent endothelial cell layer in the 5% CO_2

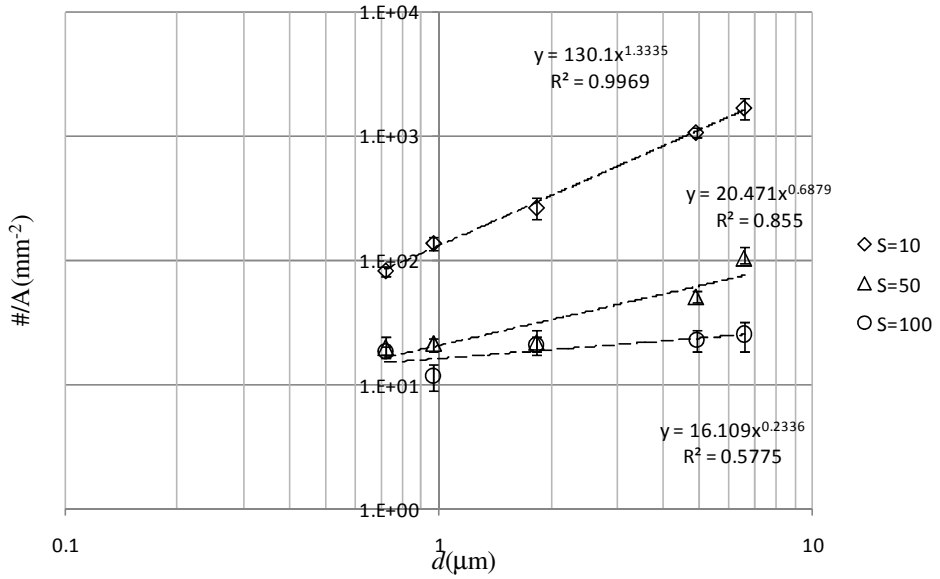

Fig. 44: Number of particle adhered on the ovarian endothelial cell per unit area as a function of particle diameter for S=10, 50 and 100

incubator at 37 °C. Fig. 44 shows the number of particle adhered per unit area on the ovarian endothelial cell. In this case, no maximum number of particle adhered is found in the particle size range considered. Since the endothelial cells are used and the confluency of cultured cell is not always uniform, relatively larger error is observed than collagen coated substrate. However, for small shear rate (S=10s^{-1}), it shows similar power law relationship as $\#/A \propto d^{-1.334}$ (R^2=0.997). As shear rate increases, the exponent of fitting line is decreased, namely, $\#/A \propto d^{-0.688}$ for S=50s^{-1} (R^2=0.855) and $\#/A \propto d^{-0.234}$ for S=100s^{-1} (R^2=0.578).

3.4.2 Effect of particle shape

The experimental study on the margination dynamics of microsphere with different shape has been performed already (Gentile et al., 2008). Commercial spherical silica particle (d=1μm), polysilicon based discoidal (γ_d=0.2, d=1.5μm) and silicon based porous quasi-hemispherical (d=1.6μm) particle has been tested in micro fluid chamber.

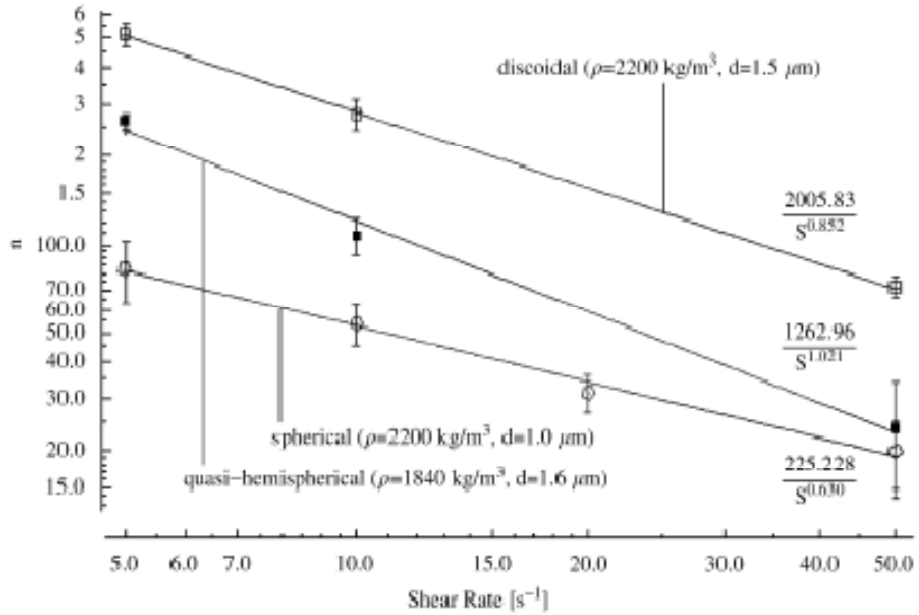

Fig. 45: Comparison among the n-S scaling laws for silica spherical (white pentagons), discoidal polysilicon (white boxes) and 1.6 μm silicon quasi-hemispherical particles (black boxes). (from Gentile et al., 2008)

The corresponding gravitational force on the spherical, discoidal and quasi hemispherical particle is approximately 10nN, 12nN and 16nN, respectively estimated based on the particle size and porosity. The physiological substrate coated with type I collagen was used. The direction of gravity was toward the wall. Definitely, gravitational force on the particle is different depending on the particle shape because of different particle material and porosity. However, as shown in Fig. 45, number of particle adhering on the collagen coated substrate is not proportional to the gravitational force. Interestingly, discoidal particle (γ_d =0.2) adheres most among the compared particle shape and quasi hemisphere adheres less than discoidal particle but more than spherical particle. This experimental result well agreed with the current mathematical prediction. By comparing the mathematical result of Fig. 25-28, discoidal particle (γ_d =0.2) shows the fastest drift velocity toward the wall in case of gravitational force toward the wall and quasi-hemisphere is slower than discoidal particle (γ_d =0.2) but faster than spherical particle,

which means that with the same injection concentration, the possibility of discoidal particle (γ_d =0.2) existing near the wall is higher than quasi-hemispherical particle and spherical particle and accordingly, the possibility of hemispherical particle existing near the wall is lower than discoidal particle (γ_d =0.2) but higher than spherical particle. It has been reported through mathematical prediction that non-spherical particle, especially, discoidal shape adheres on the substrate; (Decuzzi and Ferrari, 2006; oblate ellipsoidal particle with small aspect ratio) because of increased flat area of discoidal particle or quasi-hemispherical particle, both shape can give more chance to adhere. Additionally, non spherical particle is more favorable in terms of particle internalization (Champion et al., 2006). Hence it can be concluded that non-spherical particle, especially discoidal particle with small aspect ratio in terms of margination, is the most favorable shape.

3.5 Comparison with *in vivo* experiments

As an observer, participation in *in vivo* experiment to see the effect of particle size and shape on the biodistribution of nano/micro scale particle gives a great insight and chance to understand the biological response of particle adhesion in the animal. Here, some of *in vivo* data will be introduced to compare with the *in vitro* characterization. The procedure for in-vivo experiment is described in Decuzzi et al. (Decuzzi et al, 2010). Briefly, the animal was prepared as following. The MDA-MB-231 breast cancer cell line was purchased from ATCC (Rockville,MD). 8–10 week old female nu/nu nude mice were maintained in a facility, and all animal procedures were performed in accordance with the regulation in the University of Texas for the Care and Use of Laboratory Animals. MDA-MB-231 cells (serum free DMEM) were injected into the back of nude mice and allowed to establish tumors for 3 weeks. Mice were injected with silica beads

(10^7; low dose, or 10^8; high does in 100 μl saline) and non-spherical particles (10^8 in 100 μl saline) via tail vein (4 mice per group). Four animals were injected with the normal saline as a negative control. Two to six hours after the injection, the mice were sacrificed and the organs (liver, spleen, heart, lungs, kidneys, and brain) and tumors were weighed.

In the classical mechanics, assuming that the spherical particles are significantly smaller than the channel diameter and adhesion is occurring within in close proximity of the vessel walls where a linear shear flow can be assumed, the adhesion force between two particles can been described by the JKR theory. For a spherical particle on a very soft substrate with Young's modulus E and for an interfacial energy of adhesion ϕ, the JKR theory predicts the adhesion force of spherical particle to the substrate with a radius r_0 given by

$$r_0 = \left(\frac{3\pi\phi}{2E}\right)^{1/3} d^{2/3} \tag{25}$$

Assuming particles adhering on the substrate in the linear shear flow with contact radius r_0 (Fig. 38), as the shear rate S increases, contact area of the particle (δr_0^2) would be reduced and then ultimately the particle would be detached from the substrate. As size of particle decreases, the adhesion area would change by $2\pi r_0 \delta r_0$. With the hydrodynamic dislodging force on the spherical particle given by Eq. (15), the total energy between the particle-substrate system, U, would be

$$\delta U = \frac{3}{2}\pi F^S \mu S d^2 \delta r_0 - 2\phi\pi r_0 \delta r_0 \tag{26}$$

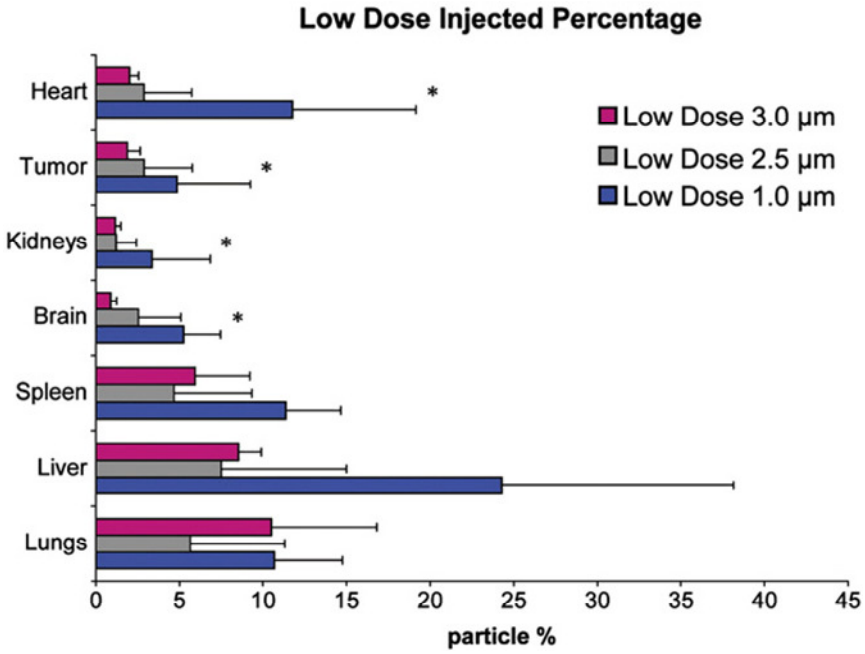

(a)

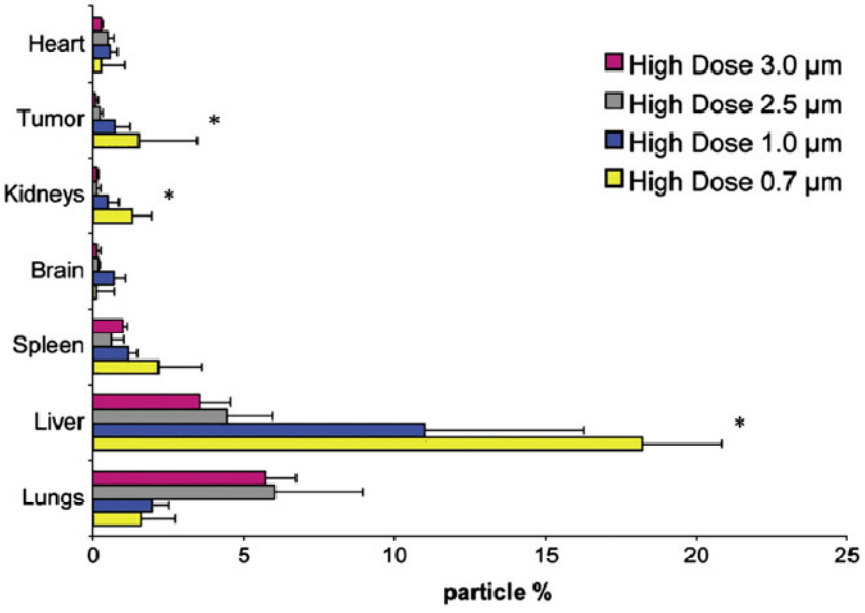

(b)

Fig 46: In-vivo silicon amount referred to the injected dose for the spherical beads, when (a) low dose (10^7 particles/animal) and high dose (10^8 particles/animal) injected. The star symbol identifies groups of data following the relationship (from Decuzzi et al., 2010)

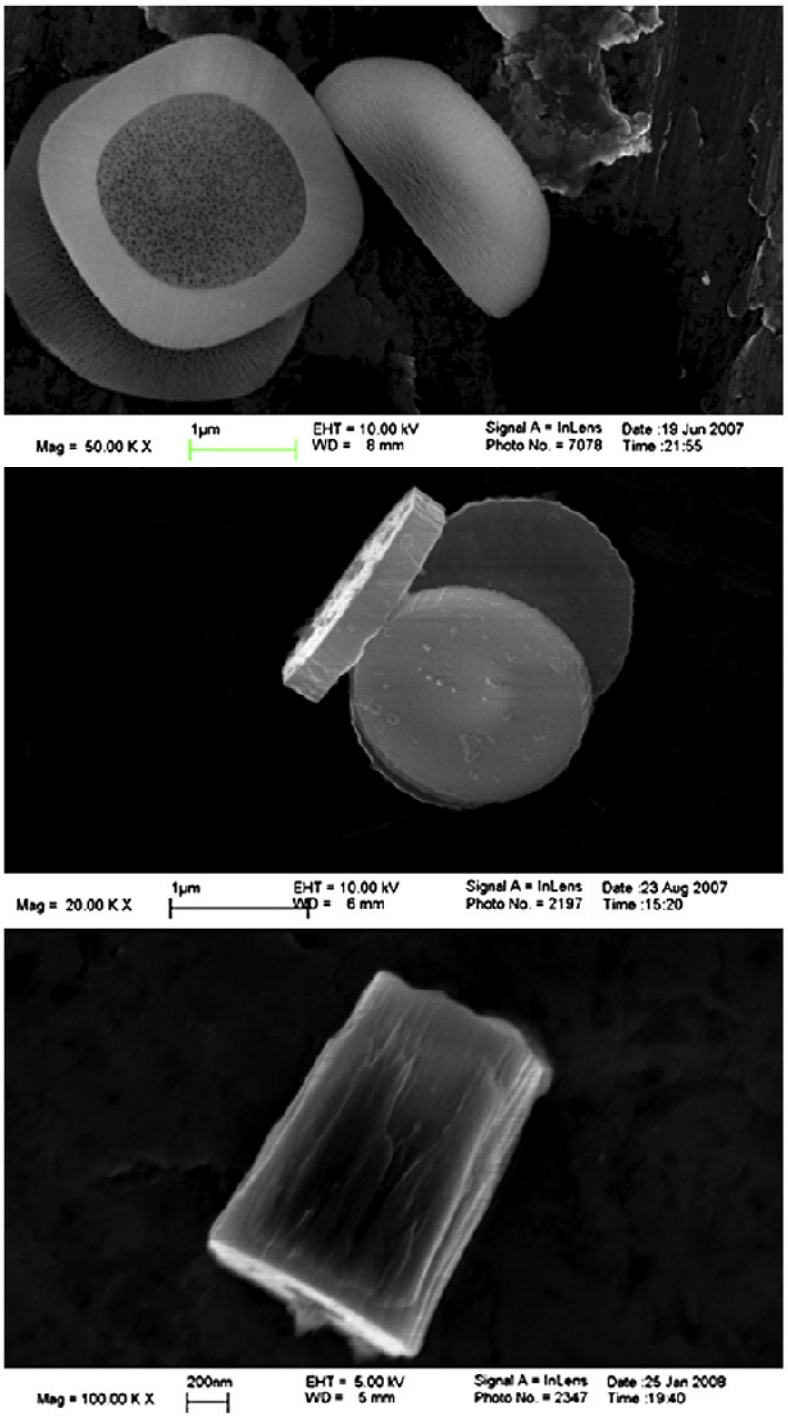

(a)

(b)

(c)

Fig. 47 SEM images of the (a) quasi-hemispherical, (b) discoidal and (c) cylindrical particles used in the in-vivo experiments. (from Decuzzi et al., 2010)

the first term being the work done by the external hydrodynamic force and the second term being associated with a decrease in adhesion energy. Firm adhesion occurs when the hydrodynamic dislodging forces of (Eq. (15)) are smaller compared to the adhesion force. Then the shear rate at which the particles would be detached due to breakage of the balance between the hydrodynamic dislodging force and adhesion force, is

$$S_d = 1.31\left(\frac{\phi^4}{E\mu^3}\right)^{1/3} d^{-4/3} \tag{27}$$

Fig 46 shows the percentage of the relative silicon content in the organs and tumor with different injection concentration. The percentage of Si content in increased as decrease of size of particle. Especially, heart, tumor, kidney and brain follow reasonably the relationship $S \propto d^{-4/3}$; heart (low dose), tumor (low dose and high dose), kidneys (low dose and high dose) and brain (low dose), liver (high dose) and spleen (high dose); . However, RES organs such as, liver, spleen and lungs does not follow the relationship.

To see the effect of shape on the biodistribution, four types of particle, such as, spherical, discoidal, quasi-hemispherical and cylindrical particle, whose volume is about 0.6μm^3, was investigated as shown in Fig 47. The concentration of particle is fixed with the high dose (10^8/100μl). Fig. 48 shows percentage of Si related to the number of particles accumulating in each organ. In the brain, kidney and tumor, since the percentage of Si particle accumulated is very small (less than 1%), there is no statistically significant difference among the different shape of particle. In the spleen, discoidal and quasi-hemispherical particles have no statistically significant difference in terms of percent of silicon content, however, accumulate more than cylindrical particles and the spherical beads. In the liver, the cylindrical particles accumulate; about 2 times more than spherical

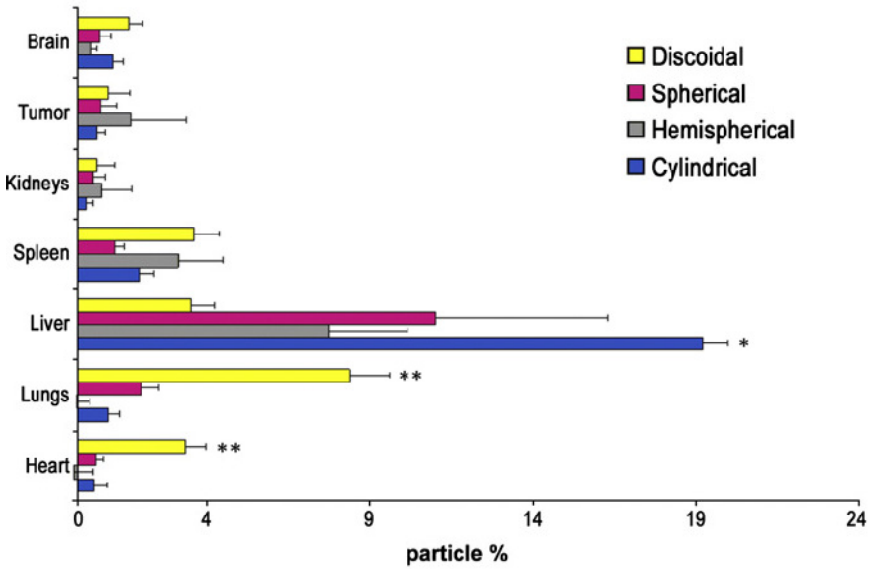

Fig. 48 In-vivo silicon amount referred to the injected dose for the non-spherical particles. This percentage of Si can be directly related to the number of particles accumulating in each organ. High dose injected. The star symbol identifies differences between the discoidal and the other particles with $p<0.001$, as detailed in the text. (from Decuzzi et al., 2010)

and quasi-hemispherical particles, and about 5 times more than the discoidal particles. No statistically significant difference between the spherical particle and quasi hemispherical particle in the terms of percentage of the silicon content in the liver was observed. In the lungs, discoidal particles are the best in terms of accumulation; about 4 times more than the spherical beads and about 8 times more than the cylindrical and quasi-hemispherical particles. Almost no hemispherical particles are observed in the lung. In the heart, the discoidal particles accumulate more than the other three particle types. Again, almost no hemispherical particle was observed.

3.6 Summary

In this chapter, effect of particle size has been discussed and the experimental measurement and compared to the mathematical prediction developed by Decuzzi and

Ferrari (Deccuzi and Ferrari, 2006). Considering very simple case, non-specific spherical particle interaction on collagen coated substrate, fitting parameters in Eq. (22) that are related to the biophysical properties of particle, substrate and flow condition, could be determined. Those variables can be analyzed as the biophysical condition of particle (size, shape and surface property) and the physiological condition of micro environment. Combining of suggested mathematical model and experimental characterization can provide the fundamental background of rational design of nano/micro particle.

Chapter 4: Conclusion

In the present study, predictive mathematical models have been developed for the transport and adhesion dynamics of nano/micro particles in microcirculation in terms of size, shape, shear rate and material properties. Also experimental models for testing dynamics of nano/micro particle in physiological condition have been developed. This confirms that spherical particle would be transported following the streamline; no drift across the streamline in the flow. At low Reynolds numbers, even non-spherical particles do not induce lateral drift. These results are in agreement with the observations of Bretherton (Bretherton, 1962) and would hold even for tortuous capillaries. Consequently, nano sized particle would circulate in the core of blood vessel and is hard to interaction with endothelial cells. However, at this scale, the shape of the particle would still play an important role on particle/cell adhesion (Decuzzi and Ferrari, 2006), cellular uptake (Decuzzi and Ferrari, 2008, Champion and Mitragotri, 2006) and diffusive transport. On the other hand, for micrometer scale particles, since St grows with the square of the particle size (a^2), the contribution of volume forces becomes important. When the St is sufficiently large enough (St>0.1), non-spherical particle moving at the proximity of the vessel wall would marginate with finite net drift velocity.

In the absence of gravitational force, the minimum Stokes number for spontaneous margination is St=0.1. The maximum drift velocity is achieved for $10 < St < 20$, depending on the particle shape (St=10 for cylindrical particle and St=20 for the others except spherical particle). Among the particle shapes considered, discoidal particles with low aspect ratio (γ_d=0.2 and 0.33) exhibit the fastest drift velocity. The presented model has been validated by comparing to other numerical and theoretical studies and the results are in qualitative agreement with experimental analysis available.

Consequently, fine balance between size, shape and particle-to-fluid density ratio with sufficiently large Stokes numbers ($St > 0.1$), even in the absence of gravitational force.

At the very low St ($St<0.1$), margination can only be achieved by applying external forces even for micro-particles. As an external force, gravitational force is considered. For sufficiently small St ($0.1<St<1$), the drift velocity grows with St. In case of non-spherical particle, the optimal shear rate in terms of margination is $St_a=10$ for cylindrical particle and $St_a=20$ for the other shape. Above that, the drift velocity decreases because of high particle inertia. Interestingly, with gravitational force, lateral drifting could be achieved for any capillary orientation for $St>1$. However, it should be considered the risk of excessive non-specific vascular adhesion on the undesired cells.

In cardiovascular applications, it is hard to achieve large St because of its higher viscosity. However, sufficiently large St can be achieved by using large and heavy materials such as, silica, silicon, iron-oxides, gold or combination of those. Otherwise, by fabricating high aspect ratio particles with careful consideration of the obvious restriction of safety, finite drift velocity could be achieved. In pulmonary flow, the smaller viscosity of air compared to blood, it is relatively easier to achieve larger Stokes number. These naturally drifting particles would give more chance for the particles to interact with the walls and circulate as sentinels for their biological targeting.

Ideally, in case of spherical particle, when the particles are transported in the fluid flow, no spontaneous drift across was observed without external force. However, in the actual particle in microcirculation, due to diffusive transport, perturbed flow by complex capillary geometry and external force (or gravitational force), etc, particle adhesion in a vessel would be observed. In the present micro fluidic chamber experiment, the main drifting mechanisms would be the diffusion and the external body force (gravitational force).

The adhesion characteristics of particles have been studied for different particle size and flow condition (shear rate, *S*). The number of particle adhering on the substrate per unit area increases for low shear rate as particle size increases. As shear rate increases, optimal particle size, that is, the particle size which shows maximum number of particle adhering, is observed. When sufficiently large sized particles are used, the hydrodynamic dislodging forces would be too strong for particles to firmly adhere on the wall. In fact, hydrodynamic force on the nano/micro sized particle in the microcirculation is in the range of the order of 10-100 pN which are larger than any non-specific particle-cell interaction. In the current case, the particle diameter that has shown the maximum number of particle adhering with shear rate S=90 is about 5μm, which corresponds to the hydrodynamic dislodging drag force of about 20pN.

The mathematical model and *in vitro* and *in vivo* study have been compared to the present study. The experimental results confirm that scaling law proposed by Decuzzi and Ferrari (Decuzzi et al., 2010) is valid for the present case of particle adhesion dynamics on biological layers. The result from i*n vivo* test also shows the similar scaling law to the present *in vitro* characterization of spherical particle in the organs, such as, heart, kidney, brain, tumor. However, RES organs, such as, liver, spleen and lungs does not follow the scaling law.

In summary, effect of particle size and shape has been studied using theoretical, numerical and experimental approach in the context of rational design of nano/micro particle for the application of delivery as a molecule carrier in the microcirculation. Different particle size and shape has been considered and the effect of geometrical properties on particle margination and adhesion has been studied. Stokes number should be large enough to take advantage of spontaneous drift of non-spherical particle. The discoidal particle with small aspect ratio has been proven to be the best in terms of

margination. The optimal size of spherical particle (4~5μm for non-specific interaction for S=75 and 90) has been found for different flow condition. Besides the current results, there are still many combinations of particulate and micro environmental properties to be further studied.

Appendix A

Range of application for the proposed methodology

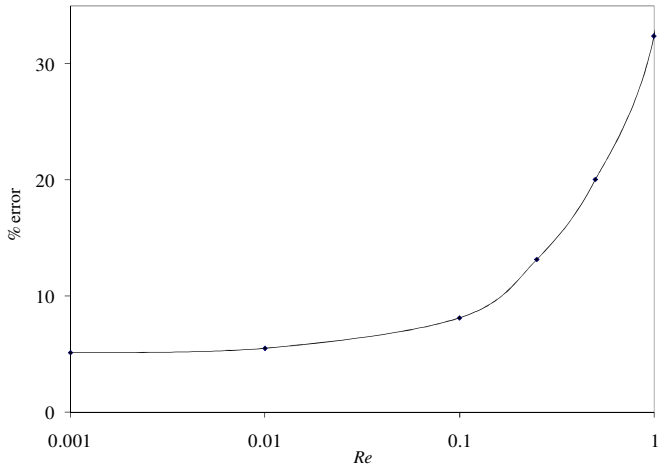

Fig. A1: Percentage error for the drag force: Stokes *vs* Navier-Stokes solution.

The methodology proposed is strictly valid in the limit of vanishing *Re* ($Re \to 0$). However, the differences between Stokes and Navier-Stokes flows become unacceptably large only for Re close and larger than unity. This can be shown, for instance, by considering a spherical particle immersed in a linear shear flow in close proximity to a rigid wall. If the analytical results by Goldman et al (1967) (pure Stokes flow) and the numerical results derived by FLUENT v6.0 for the drag force exerted over the particle are compared, it is derived that the percentage difference grows with Re and becomes larger than 10% only for $Re > 0.1$ (Fig. A1). Consequently, we believe that the methodology employed would generate quite accurate results up to $Re = O(0.1)$.

Particulate systems employed in drug delivery and biomedical imaging are made by a number of materials with a different density: liposome/polymeric materials (ρ_p = 1000 kg/m^3); silicon/silica (ρ_p = 2000 kg/m^3); iron-oxide (ρ_p = 8000 kg/m^3); gold (ρ_p =

20000 kg/m^3). Therefore, when considering pulmonary flow (ρ_{air} = 1 kg/m^3), the resulting Stokes number St (= $(\rho_p/\rho)Re$) would be fairly large, at most O(10^4); whereas, in cardiovascular applications, the smaller relative density of the particle to the fluid would lead to St at most O(1). Therefore we believe that the analysis and the results presented can be used also for cardiovascular applications but in the low St range.

Appendix B

TNF-α in Systemic Vascular Dysfunction: an Atomic Force Microscopy Analysis

B.1 Introduction

As a side work, the effect of TNF-a in vascular dysfynction by measuring elastic modulus of ehdothelial cells from different organs. Along the circulatory system, endothelial cells (ECs) line the walls of blood and lymphatic vessels and finely regulate the exchange of nutrients and waste products between the vascular compartment and the surrounding tissue. The solute exchange is accomplished through two pathways: transcellular and paracellular (Komarova and Malik, 2010). The first pathway is associated with the active transport of macromolecules (plasma proteins) and particulate agents across the endothelial cell layer, mediated by cellular vesicles following a process known as transcytotis. The second pathway is associated with the convective and diffusive transport across the inter-endothelial gaps within adjacent cells. Depending on the organ and vascular district, the proportion of paracellular to transcellular transport varies. In organs of the reticulo-endothelial system (RES), such as the liver, spleen and bone marrow, the discontinuous and highly fenestrated endothelium favors the paracellular transport across vascular openings, that can be as large as several hundreds of nanometers (Michiels, 2003). Differently, the vasculature in non-RES organs is characterized, under physiological conditions, by a continuous endothelium which does not allow the extravasation of solute molecules larger than 3-5 nm (Michiels, 2003).

The integrity of the vessel walls and the regulation of the transvascular transport are of fundamental importance in preserving tissue-fluid homeostasis. Several factors are known to alter the paracellular and transcellular transport and eventually lead to

unbalance homeostasis and major vascular dysfunctions. These include physical factors as the trans-endothelial hydrostatic fluid pressure (Tokuda et al., 2009), and biochemical factors as the pro-angiogenic cytokine VEGF (Vascular Endothelial Growth Factor) (Dvorak, 2006); the pro-inflammatory cytokines TNF-α (Tumor Necrosis Factor -α) (Worrall et al., 1997), histamine (Pober and Sessa, 2007) and thrombin (Komarova et al., 2007); and bacterial toxins, as lipopolysaccharide (LPS) (Wu et al., 2005). All these circulating molecules can recognize counter-molecules (receptors) expressed on the endothelial cells and increase vessel permeability favoring the paracellular pathway. The continuum endothelium in healthy vessels can become hyperpermeable during an inflammatory process, a normal response to external injury and pathogens. During inflammation, TNF-α plays a major role being involved in the activation and maturation of leukocyte and the over-expression of specific adhesion molecules on the endothelium (E-selectin, ICAM-1, VCAM-1), which favor the local recruitment of leukocytes and support healing. A large number of diseases, not associated with any external stimuli or injury, are known to induce high plasma levels of several cytokines including TNF-α. In healthy patients, the plasma level of TNF-α is generally smaller than 1 pg/ml, but its concentration can be abnormally high in the presence of atherosclerosis (Butt and Jaschke , 1995, Feldman et al., 2000, Libby et al., McKellar et al., 2009); during tumorigenesis and tumor growth (Kim et al., 2006); in patients with rheumatoid arthritis (McInnes and Schett, 2007); in women undergoing pre-eclamptic pregnancies (Laskowska et al., 2006); and in obese individuals (Rocha et al., 2009). In incidences of acute trauma, elevated circulating levels of TNF-α have also been reported, including, but not limited to, traumatic brain injury (Harting et al., 2008) and hemorrhagic shock (Roumen et al., 1993, Suter et al., 1992). However, others have reported that soluble forms of membrane receptors (TNFR) rather than TNF-α are initially released following

trauma (based on serum levels one hour after arrival at a trauma center) and may serve as an indirect indicator that TNF-α associates with trauma (Tan et al., 1993). Significantly elevated TNF-α levels have also been linked to the onset of multiple organ failure (MOF) in trauma patients, where elevated cytokine levels at as early as 1-hr post admission to a trauma center are indicative of risk of developing MOF (Roumen et al., 1993).

In this study, three endothelial cell lines originating from different vascular districts, namely coronary (HCAECs), pulmonary (HPMECs) and umbilical (HUVECs), have been analyzed in terms of mechanical properties and cytoskeletal re-organization upon stimulation with TNF-α. In particular, the apparent elastic modulus, the viscoelastic response and the non-specific adhesion forces for the three cell lines have been estimated using atomic force microscopy (AFM). This technique has been successfully used in characterizing the mechanical response of several cell types in different species (Iyer et al., 2009, Mahaffy et al., 2004 and Mathur et al., 2001). In addition, the biological response of the three cell lines to the pro-inflammatory stimulus has been characterized by observing the re-organization of the F-actin filaments within the cytoskeleton, through fluorescence microscopy, and by quantifying the level of membrane expression of adhesion molecules, as ICAM-1, through ELISA. The main objective of the present analysis is to understand how and if the cellular response to TNF-α would depend on the vascular district considered.

B.2 Materials and Methods

Cell culture and TNF-α treatment

Supplies were purchased from the following sources: Human Coronary Artery Endothelial Cells (HCAEC, CC-2585 Lot # EN000307), Endothelial cell basal medium-2 (EBM-2) and the Endothelial cell growth medium (EGM-2) BulletKit (SingleQuots) were

purchased from Lonza (Walkersville, MD). Human Pulmonary Microvascular Endothelial Cells (HPMEC, C-12281 Lot # 9030501) were ordered from PromoCell (Heidelberg, Germany). Human Umbilical Vein Endothelial Cells (HUVEC, Lot # EN000307) were purchased from GlycoTech (Gaithersburg, MD). Tumor necrosis factor-alpha (TNF-α) was purchased from Biosource (Camarillo, MD). Treated cell culture dishes (60 x 15mm) were provided by Corning Incorporated (Corning, NY). Preclined glass microscope slides (3"x 1"x 1.0mm) were obtained from Fisher Scientific (Pittsburgh, PA). Triton X-100 was ordered from ICN Biomedicals, Inc (Aurora, OH, USA). Anti-ICAM antibody was purchased from NeoMarkers (Fremont, CA, USA). Anti-mouse IgG 2b (γ-2b)-peroxidase and 2,2'-azino-bis(3-ethylbenzthiazoline-6-sulphonic acid) (ABTS) were purchased from Roche (Indianapolis, IN, USA). Tween 20 was purchased from Fisher (Pittsburgh, PA, USA). Anti-ICAM-1 fluorescein isothiocynate (anti-ICAM-1-FITC) was purchased from Biosource (Camarillo, MD, USA). Alexa Fluor 555 Phalloidin was obtained from Molecular Probes Invitrogen detection technologies.

In order to investigate the influence of TNF-α on the cell membrane elasticity, HCAEC, HUVEC and HPMEC were seeded in a 60 mm culture dish to 80% confluence, with EBM-2 medium supplemented with an EGM-2 BulletKit and incubated 24 hrs at 37°C in a 5% CO_2 atmosphere. The cells were then treated with 3ml of TNF-α [10ng/ml] for 20h (Danila et al., 2009) to promote an inflammatory response. Culture dishes were later rinsed with EBM-2 media to wash out the TNF-α solution. Data were taken at room temperature in a liquid atmosphere.

ELISA and Immunofluorescence Analysis

ELISA and Immunofluorescence Analysis have been performed by Dr. Conyers group. Cells (4×10^4 cells/well) were grown in EBM media supplemented with an EGM-2 Bullet Kit (Cambrex) at 37 °C in 5% CO_2. ICAM-1 was expressed on the surface of the HCAEC, HUVEC and HPMEC by activating the cells with 10 ng/ml TNF-α for 20 hours, and the extent of ICAM-1 expression was assessed by ELISA. For ELISA, the cells were incubated with TNF-α (10 ng/ml) for 20 hours at 37 °C and 5% CO_2 in a 96-well plate. The next day, the cells were washed with PBS, fixed with Formalin for 20 minutes at room temperature, incubated with 3% BSA and 0.1% Tween 20 for 1 hour and then incubated with anti-ICAM antibody (1:1,000 dilution in PBS, v/v) for 2 hours at 25 °C. The unbound anti-ICAM antibody was removed from the activated HCAEC by washing with PBS and the cells were incubated with anti-mouse IgG 2b (γ-2b)-peroxidase (1:2,000 dilution in PBS, v/v) for 1 hour at room temperature. The excess of secondary antibody was washed away with PBS and then ABTS substrate (100 µl) was added. After 30 minutes of incubation, the absorbance at 405 nm was measured with a Tecan plate reader. Non-activated cells were also subjected to ELISA as controls.

For fluorescence microscopy measurements, cells (4×10^4 cells/chamber) were incubated in 8-chamber tissue culture slides overnight at 37 °C in 5% CO_2. The next day, the cells were activated with TNF-α (10 ng/ml in EBM-2 media) for 20 hours at 37 °C in 5% CO_2. Next, the cells were washed with PBS and fixed with 4% paraformaldehyde for 15 minutes at room temperature. The cells were then washed two more times with PBS and incubated with a solution of 0.1% Triton X-100 in PBS for 5 minutes. The unreacted sites were blocked with 1% BSA for 20 minutes. To stain actin filaments, the cells were then incubated with Alexa Fluor 555 phalloidin (5 units/ml [0.16 µM]) for 30 minutes at room temperature and washed two times with PBS before the chamber partitions were removed and the slides were dried in air. The cells' nuclei were labeled with DAPI and

then the images were captured with an Olympus IX71 inverted microscope equipped with TRITC and DAPI filters for epi-fluorescence measurements.

Atomic force microscopy

A Bioscope II Atomic force microscope (Veeco, Santa Barbara, CA) combined with a fluorescence microscope (Nikon TE-2000, Melville, NY) was used for testing and imaging the cells. The AFM probe consisted in a 5 μm diameter silica particle (colloidal probe) attached at the edge of silicon nitride V-shaped cantilevers (Novascan, Ames, IA) (Fig.1). Data were acquired with the Research NanoScope software version 7.30. A schematic representation of the cantilever tip interacting with a cell membrane and the geometrical features of the colloidal probe are shown in Fig. B1. The relatively large particle size leads to larger contact areas and more evenly distributed contact pressures, which limit the penetration depth upon contact and provides average information (Iyer et al., 2009). The cantilever spring constant was calibrated using thermal tuning and resulting in values from 0.1 to 0.3 N/m with less than ~8% of error (Butt and Jaschke, 1995) in EBM-2 cell culture media (nominal value of 0.32 N/m).

Analysis of the force-distance curve

The force F applied over the cell membrane by the colloidal probe can be expressed as

$$F = kd \tag{1}$$

where, k and d are respectively the spring constant and deflection of the cantilever (Fig. B1). Following the Hertzian theory (Shigley, 1983), the contact radius a at the interface between the cell and the colloidal probe can be expressed as

$$a = \left(\frac{3FR}{4E}\right)^{\frac{1}{3}} = \left(\frac{3kdR_2(1-{\nu_1}^2)}{4E_1}\right)^{\frac{1}{3}} \tag{2}$$

where E is the effective elastic modulus of the system (cell membrane-colloidal probe) defined as

$$\frac{1}{E} = \frac{1-{\nu_1}^2}{E_1} + \frac{1-{\nu_2}^2}{E_2} \tag{3}$$

depending on the elastic moduli and Poisson's ratios of the cell membrane (E_1, ν_1) and colloidal probe (E_2, ν_2); R is the effective radius of the system defined as

$$\frac{1}{R} = \frac{1}{R_1} + \frac{1}{R_2} \tag{4}$$

depending on the radi R_1 and R_2 of the cell membrane and colloidal probe, respectively. Introducing the penetration depth δ (Fig. B1), eq.(2) can be rephrased as $a = \sqrt{R_2\delta}$, and combining eq.(1) and (2), the relationship between the deflection of the cantilever d and the indentation depth δ of the probe is derived as

$$d = \eta\delta^{3/2} \qquad \text{with} \qquad \eta = \frac{4E_1{R_2}^{1/2}}{3k(1-{\nu_1}^2)} \tag{5}$$

The parameters directly measured by operating the AFM are the cantilever beam deflection d (or equivalently the force $F = k\,d$) and the relative vertical scanner position Z. Using simple geometrical considerations (Fig.B1), the parameter Z can be related to the penetration depth δ as

$$\delta = (Z - Z_0) - (d - d_0) \tag{6}$$

where Z_0 is defined as the vertical scanner position where the slope of the F-Z curves change abruptly and d_o is the corresponding cantilever beam deflection (Touhami et al., 2003). By using eq.s (1) and (6), the force-displacement curves F-Z directly acquired through the AFM can be turned into displacement-penetration depth curves (d-δ), and through eq.(5), the parameter η can be derived by fitting the (d-δ) curves. Since, the

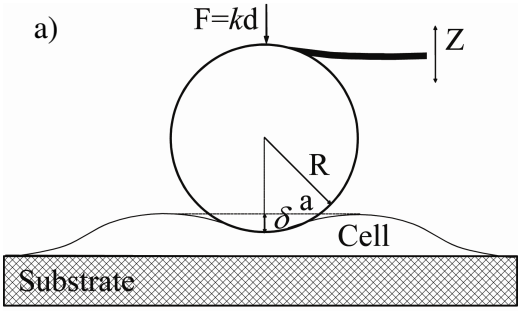

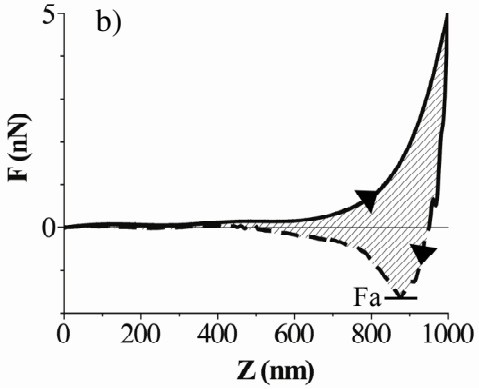

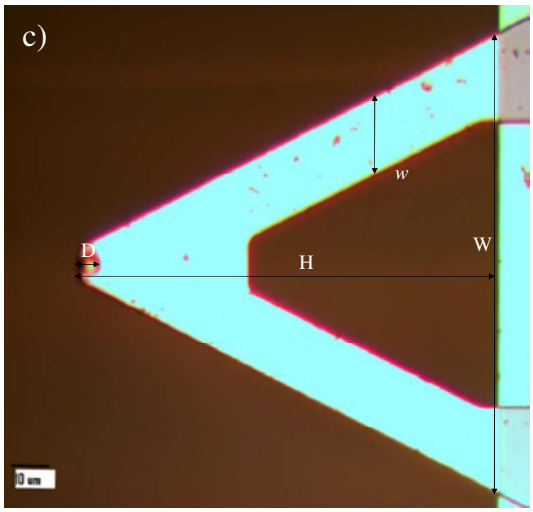

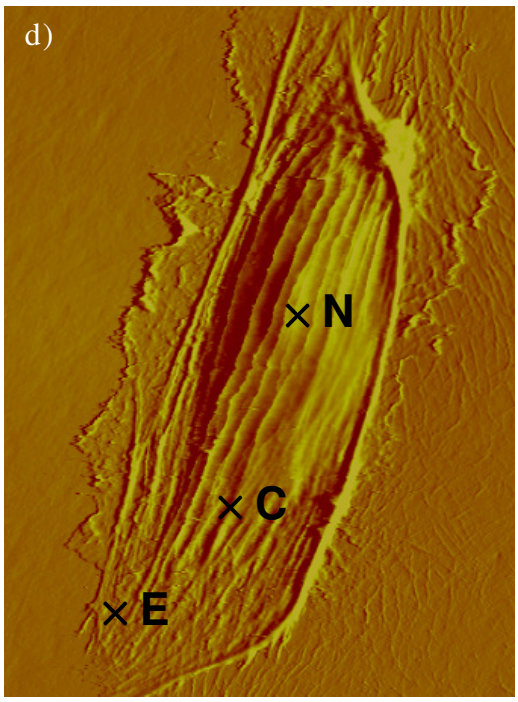

d	5 µm
H	115.0 µm
W	126.9 µm
W	21.2 µm

Fig. B1 Atomic force microscopy for the mechanical characterization of live cells. a) Schematic of the colloidal probe (spherical particle attached at the tip of a cantilever beam) interacting with the cell membrane adhering over a rigid substrate. b) A representative force-displacement curve with a measurable force of adhesion F_a and area ratio A_v. c) Microscopy image and geometrical data for the V-shaped cantilever beam with a colloidal probe of d = 5 µm in diameter; d) AFM micrograph of a HCAEC scanned alive to 120 µm (X-Y) in EBM-2 media at room temperature. Contact mode in liquid (DNP-S f_o=12-24 kHz, k=0.06 N/m) (N: Nucleus; C: Contact area; E: Edge).

a)

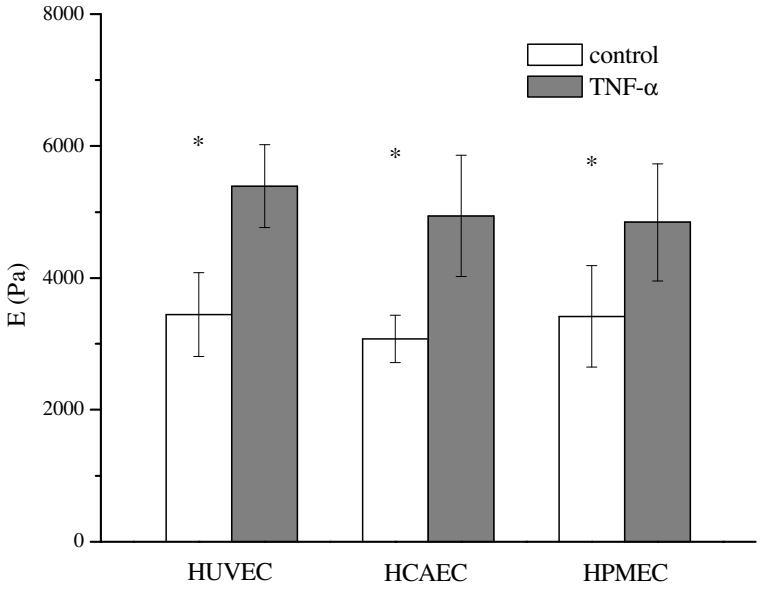

b)

Cell type and Condition		Apparent Elastic Modulus [kPa]
HUVEC	un-stimulated	3.44 ± 0.64
	TNF-α stimulated	5.39 ± 0.63
HCAEC	un-stimulated	3.07 ± 0.36
	TNF-α stimulated	4.94 ± 0.92
HPMEC	un-stimulated	3.42 ± 0.77
	TNF-α stimulated	4.84 ± 0.89

Fig. B2 Apparent elastic modulus for the three different endothelial cell lines. a) Bar chart of the apparent elastic modulus E for the HUVEC, HCAEC and HPMEC under un-stimulated (control) and stimulated (20h with 10 ng/ml TNF-α) conditions. b) Tabular form of the apparent elastic modulus where data are presented as mean±SD (Find = 0.5 nN; vind = 0.25 µm/s; * means $p < 0.01$).

spring constant k of the cantilever, the radius R_2 of the colloidal probe and the Poisson's ratio ν_1 of the cell ($\nu_1=0.5$) are fixed, the elastic modulus E_1 can be readily derived from η. For the measurement of the elastic modulus, three different approaching/retracting velocities (0.25μm/s, 0.5 μm/s and 1.0 μm/s) and three different forces (0.5nN, 1.0nN and 2.0nN) were used. The approaching curves (solid line in Fig. B1b) were considered for calculating the elastic modulus of the cell membrane. The maximum force applied was determined by the trigger mode of the Bioscope-II. The adhesion force at the interface between the cell membrane and the colloidal probe was also measured using the Bioscope-II, fixing the approaching velocity to v_a=1μm/s and using two different retracting velocities (v_r=1μm/s and 40μm/s). The energy losses associated with the viscoelastic deformation of the cell membrane were estimated by dividing the area between the approaching and retracting curves by the area associated with the approaching curve, giving the area ratio A_v. For each group not less than 50 measurements were done for determining the *F-Z* curves.

Statistical Analysis

The Student's t-test was used to compare two groups. One-way ANOVA with repeated measures was used for multiple comparisons, Significance was assumed at a P value ≤ 0.05 or 0.1. The data and errors are expressed as means ± SD.

B.3 Results

Effects of TNF-α stimulation on the apparent elastic modulus

The apparent compressive elastic moduli were calculated by analyzing the force-displacement curves obtained through AFM following the Hertzian contact theory, as described in the Materials and Methods. The same procedures were applied to all three

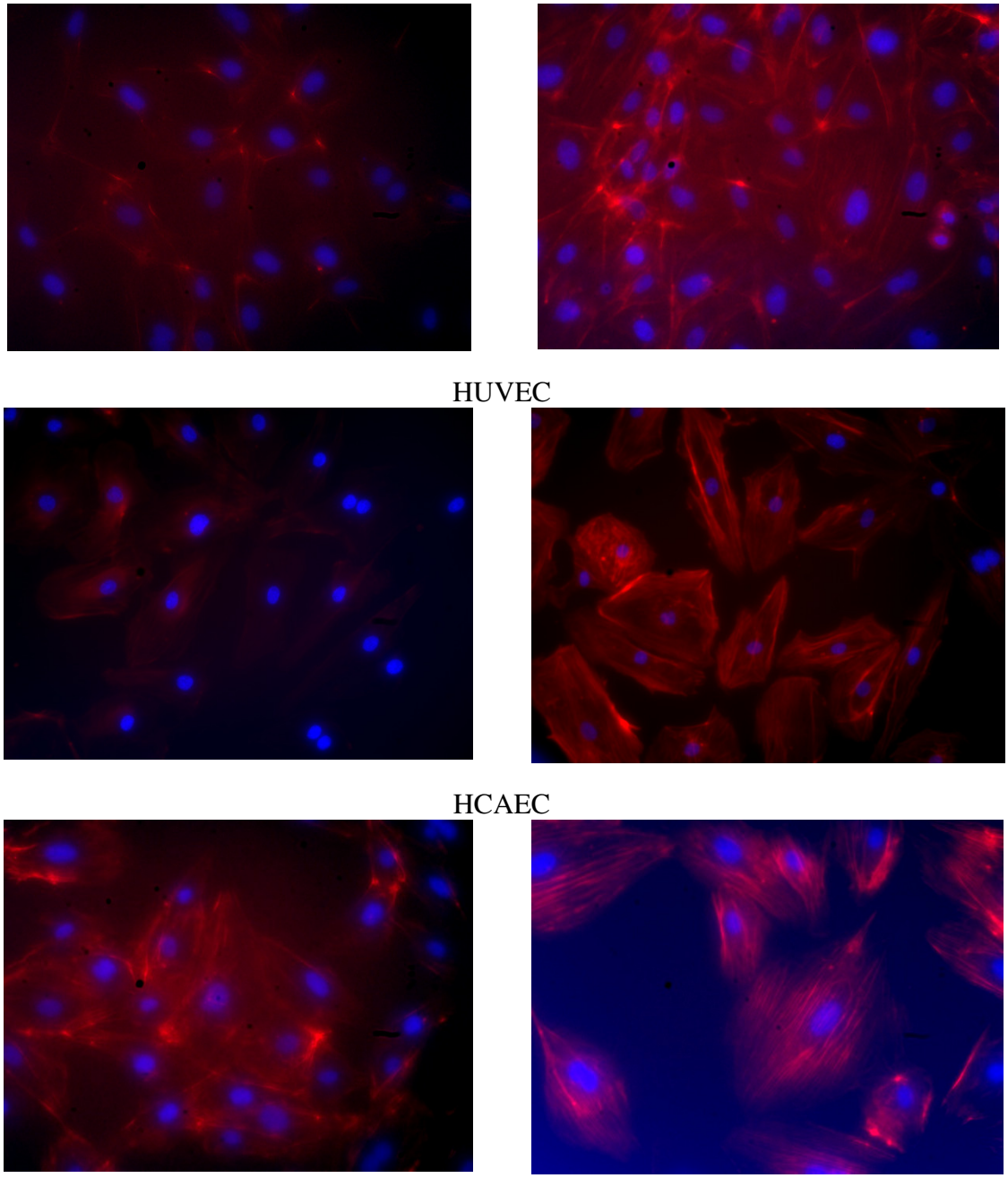

Fig.3 Fluorescence microscopy analysis of F-actin organization. The left column shows the un-stimulated cells (control) and the right column the cells stimulated with 10 ng/ml TNF-α for 20 h. In red are the actin filaments (Alexa Fluor 555 phallodin staining) and in blue the cell nuclei (DAPI staining).

different cell lines in both the un-stimulated (control) and stimulated conditions. A typical force-displacement curve is shown in Fig. B1b, where the dashed line corresponds to the approaching curve and the solid line to the retracting curve. The curves were measured over relatively flat regions of the cell membrane (point C in Fig. B1c), always sufficiently far from the cell nucleus (point N in Fig. B01c) and edge (point E in Fig. B1c). The force-displacement curves were recorded in the same location of the cell, and the apparent elastic modulus were very consistent exhibiting small standard deviations over the multiple measurements. All the force-displacement curves were obtained for an indentation force F_{ind} of 0.5 nN and an approaching/retracting probe velocity v_{ind} of 0.25 μm/sec. For such small values of F_{ind} and v_{ind}, the assumptions of the Hertzian theory are fully satisfied (Mathur et al., 2001): the indentation depth was always smaller than 200 nm (sufficiently smaller than the thickness of the cell) and the viscoelastic response of the cell membrane was negligibly small. The presence of a cell under the probe was monitored in situ through an optical microscope.

The apparent elastic moduli for the three cell lines are presented in the bar chart of Fig. B2, and related table, for both un-stimulated (white bars) and stimulated (dark bars) conditions. It was measured $E = 3.44 \pm 0.64$ kPa for the HUVECs, $E = 3.07 \pm 0.36$ kPa for the HCAECs and $E = 3.42 \pm 0.77$ kPa for the HPMECs in the un-stimulated condition. There was no statistically significant difference between the apparent elastic modulus of the three cell lines ($p < 0.05$), giving an average $E = 3.31 \pm 0.35$ kPa. This result is in good agreement with other analysis available in the literature, conducted on endothelial cells following the same procedures (Mathur et al., 2001). Also, these results confirm that cells performing similar functions (endothelial cells) but located in different organs do exhibit the same apparent elastic modulus and, consequently, similar cytoskeletal organization.

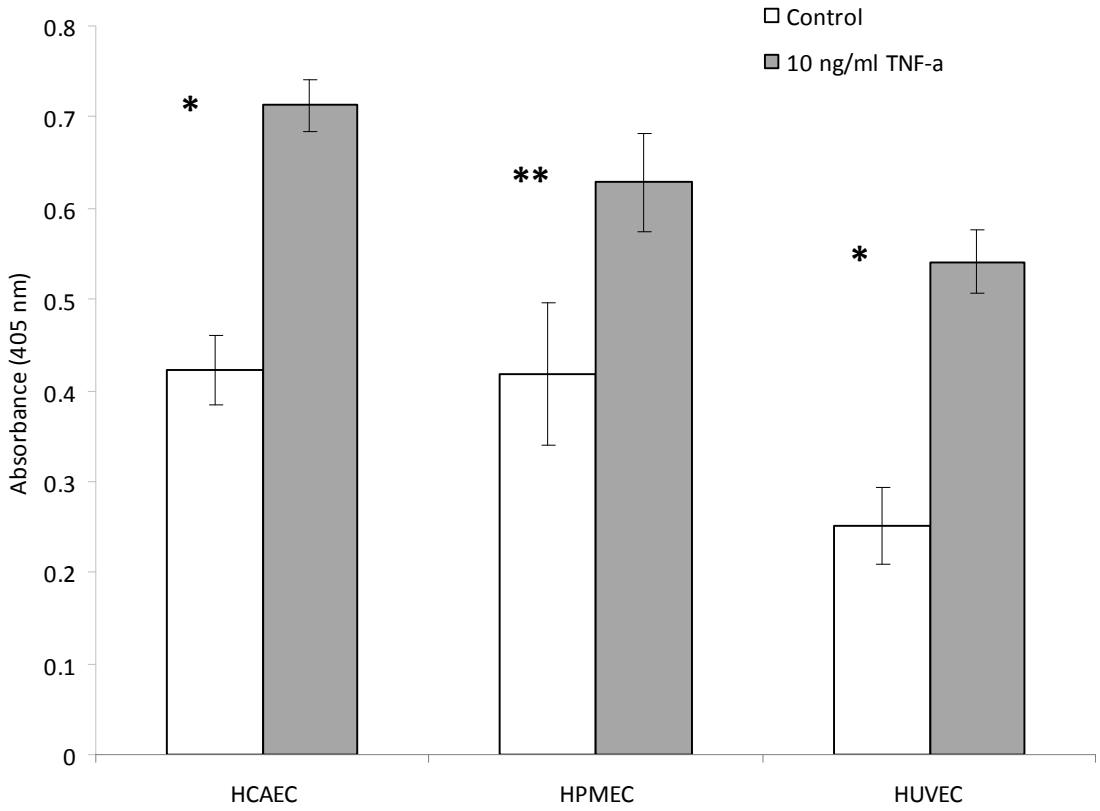

Fig. B4 Expression of adhesive molecules ICAM-1 measured through ELISA test, for un-stimulated cells (white bar) and cells stimulated with 10 ng/ml TNF-α for 20 h (grey bar). (* means $p<0.01$ and ** means $p<0.05$).

About 20 hours after stimulation with TNF-α, force-displacement curves were recorded and analyzed to derive the apparent elastic moduli $E = 5.39 \pm 0.63$ kPa for the HUVECs, 4.72 ± 1.15 kPa for the HCAECs and 4.84 ± 0.89 kPa for the HPMECs. Compared to the un-stimulated cells a statistically significant increase ($p < 0.01$) in the apparent modulus is observed for all cell lines with a ratio (E_s/E_u) between stimulated (E_s) and un-stimulated (E_u) cells of 1.54, 1.42 and 1.56 respectively for HCAECs, HPMECs and HUVECs. In other words, an increase in cell stiffness of about 50% is observed upon stimulation with 10 ng/ml of TNF-α over 20 hours. No statistically

significant difference is observed among the apparent modulus of the stimulated cell lines ($P < 0.1$), with an average $E = 4.98 \pm 0.53$ kPa.

The measurement of the apparent elastic modulus is influenced by the force applied over the cell membrane and by the velocity of the probe. A sensitivity analysis was performed on E by varying the indentation force F_{ind} between 0.5 and 2 nN and the indentation velocity v_{ind} between 0.25 and 0.1 μm/sec. The results of such analysis, summarized in the Appendix B.6, confirmed the importance of reducing F_{ind} and v_{ind} for accurately estimating the compressive modulus. Different methods have been proposed to extract the mechanical properties of cells, such as magnetic (Bausch et al., 1999) and optical (Wei et al., 2008) tweezers, micropipettes (Sato et al., 1990) in addition to atomic force microscopy. Generally, the methods and the procedures affect the final measure giving different mechanical properties for the same cell type. Nonetheless, it is here important to emphasize that the present work aims at a comparative analysis rather than to an absolute measurement of the cellular mechanical properties.

The cellular response to TNF-α stimulation has been also documented by analyzing the reorganization of the actin filaments within the cytoskeleton and the overexpression of the adhesive molecules ICAM-1. The staining of the F-actin filaments with Alexa Fluor 555 phalloidin revealed, in un-stimulated cells, filaments mainly lining the cell edge with a few fine filaments transversing the cell (Fig. B3 – un-stimulated cell). Upon stimulation with TNF-α, the fluorescence intensity associated with the F-actin filaments increased documenting an enhancement in number and thickness of the filaments, more unifroomly distributed across the whole cell (Fig. B3 – stimulated cell). This is in agreement with previous experimental work reporting, upon TNF-α stimulation, a remodeling of the cytoskeleton mediated by F-actin and microtubule reorganization [6, 33, 48]. Also, the level of expression of ICAM-1 was measured

through ELISA demonstrating a statistically significant increase in the surface density of this adhesive molecule (Fig. B4), as expected based on previous analysis (Danila et al., 2009).

Effects of TNF-α stimulation on the force of adhesion and viscoelastic response

In addition to the apparent elastic modulus, the adhesive force at the interface between the colloidal probe and the cell membrane and the viscoelastic response of the cell were recorded. The force of adhesion F_a was estimated as the maximum force measured along the retracting curve (Fig. B1b), following (Attard, 2007); whereas the viscoelastic response was quantified as the ratio between the energy dissipated due to viscoelastic losses (area between the approaching and retracting curves – dashed area in Fig. B1b) and the overall mechanical work performed (area under the approaching curve), following (Attard, 2007).

Since, the AFM probe was not decorated with any ligand molecules, interfacial adhesion was only associated with weak non-specific interactions. This was reflected by the negligibly small values of adhesion forces (<< 1 nN) measured with low indentation forces F_{ind} (= 0.5 nN) and velocities v_{ind} (= 0.25 μm/s). In all the experiments, the retracting curves appeared as continuous with no noticeable abrupt jumps, generally associated with the breakage of specific molecular bonds, thus confirming the non-specific nature of the forces at the probe-cell interface. Therefore, in order to generate appreciable adhesive forces and viscoelastic losses, the indentation force and the retracting velocity were increased up to F_{ind} = 5.0 nN and v_{ret} = 40.0 μm/s, respectively. Fig. B5 shows the force of adhesion F_{adh} and the area ratio A_v, defined as above, for the three different cell lines under un-stimulated (white bars) and stimulated (black bars) conditions.

a)

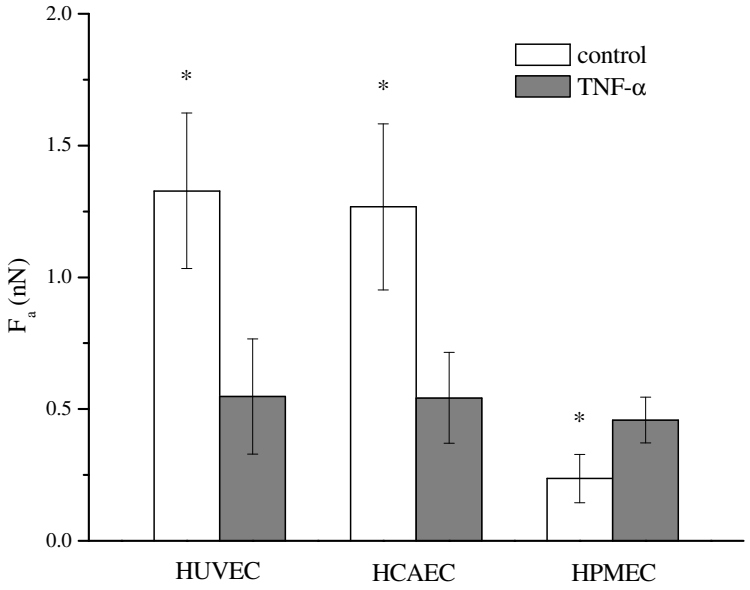
2.0
1.5
1.0
0.5
0.0
F_a (nN)
control
TNF-α
*
*
*
HUVEC
HCAEC
HPMEC

b)

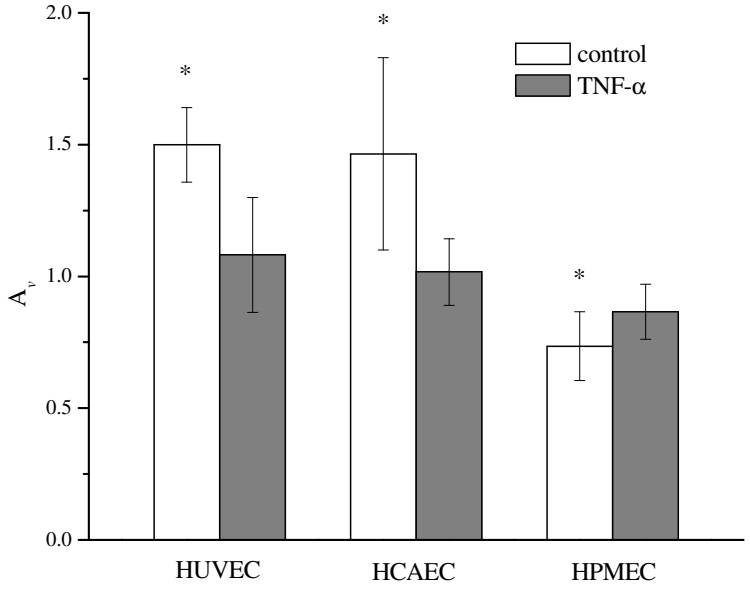
2.0
1.5
1.0
0.5
0.0
A_v
control
TNF-α
*
*
*
HUVEC
HCAEC
HPMEC

c)

Cell type and Condition		Force of Adhesion F_a [nN]	Area ratio A_v
HUVEC	un-stimulated	1.32 ± 0.30 nN	1.50 ± 0.14
	TNF-α stimulated	0.55 ± 0.22 nN	1.08 ± 0.22
HCAEC	un-stimulated	1.26 ± 0.31 nN	1.47 ± 0.37
	TNF-α stimulated	0.54 ± 0.17 nN	1.02 ± 0.13
HPMEC	un-stimulated	0.24 ± 0.09 nN	0.74 ± 0.13
	TNF-α stimulated	0.46 ± 0.09 nN	0.87 ± 0.10

Fig. B5 Adhesion force and viscoelastic response of the three different endothelial cell lines. a) The force of adhesion F_a (a), the area ratio A_v (b) and their tabular form (c) for the three different cell lines (HUVEC, HCAEC and HPMEC) under un-stimulated (control) and stimulated (20h with 10 ng/ml TNF-α) conditions. (F_{ind} = 5 nN; v_{ret} = 40 m/s, and * means $p < 0.01$).

For the un-stimulated HUVECs and HCAECs an adhesion force (area ratio A_v) of, respectively, 1.32±0.30 nN (1.50±0.14) and 1.26±0.31 nN (1.47±0.37) was measured with no statistically significant difference ($P < 0.01$); whereas significantly smaller was the adhesion force (area ratio) estimated for the un-stimulated HPMECs with a value of 0.24±0.10 nN (0.74±0.13). It is interesting to observe that under physiological conditions, the viscoelastic losses associated with the endothelial cells of the pulmonary microvasculature are about 50% smaller than those associated with the umbilical and coronary endothelial cells. Indeed, the lung microvasculature, following the respiratory cycle, is continuously subjected to compression and expansion, and a smaller area ratio A_v would imply lower viscoelastic losses possibly reflecting a natural evolution of the system towards a more energetically efficient operation.

More interestingly, for the stimulated cells, no significant difference was observed among the three cell lines ($P < 0.01$) with a force of adhesion (area ratio A_v) of, respectively, 0.55±0.22 nN (1.08±0.22) for the HUVECs, 0.54±0.17 nN (1.02±0.13) for the HCAECs and 0.46±0.09 nN (0.74±0.13) for the HPMECs. The force of adhesion and viscoaelastic losses for the HUVECs and HCAECs decreased significantly (50%) upon stimulation with TNF-α, whereas an opposite trend was observed for the HPMECs. In the Appendix B.6, a sensitivity analysis is presented elucidating the effect of the retracting velocity on the force of adhesion and viscoelastic losses. It is confirmed that the viscoelastic response of the cell membrane decreases as the retracting velocity reduces.

B.4 Discussion

TNF-α is a pro-inflammatory cytokine secreted primarily by macrophages and endothelial cells during an inflammatory response (Old, 1987). However, it is becoming clear that other cells can as well release in the tissue and eventually in the circulation large amounts of TNF-α, including lymphoid cells, mast cells, cardiac myocytes, adipose tissue, fibroblasts, and neuronal tissue (Old, 1987 and Pennica et al., 1985).

The physiological plasma concentration of TNF-α is smaller than 1 pg/ml. However under pathological conditions, a substantial increase was documented depending on the patient, type and stage of the pathology. In arthritis rheumatoid (RA), TNF-α plasma concentrations were shown as high as 1 ng/ml (Danis et al., 1992). Similar values were measured in patients with early atherosclerosis (1-2 ng/ml (Skoog et al., 2002)). Cancer is another pathology well known to induce large plasma concentrations of TNF-α. For instance in colorectal neoplasia, risk factors were associated with levels of just 2 pg/ml (Kim et al., 2008); in pancreatic adenocarcinoma, this value moved to about 30 pg/ml (Talar-Wojnarowska et al., 2009); in non-small cell lung cancer, a circulating TNF-α of

Table B1 List of the most common pathologies presenting higher levels of circulating TNF-α and corresponding concentration.

Pathology	**Plasma level of TNF-α [pg/ml]**
physiological conditions	< 1.0
arthritis rheumatoid	1000
Atherosclerosis	1000 – 2000
colorectal cancer	2
pancreatic adenocarcinoma	30
non-small cell lung cancer	10
chronic lymphocytic leukemia	20
prostate cancer	4
metastatic prostate cancer	6
breast cancer	5
pre-eclampsia	200
obesity	10
Hemorrhagic shock alone	60
Hemorrhagic shock with subsequent MOF	160

10 pg/ml was measured (Derin et al., 2008); in chronic lymphocytic leukemia, the plasma concentration was of about 20 pg/ml (Ferrajoli et al., 2002); in prostate cancer, it reduced to 4 and 6 pg/ml, with the larger values being associated with metastatic spread (Michalaki et al., 2004), and similar levels were observed in breast cancer (Tesarová et al., 2000). Extraordinarily high levels of circulating TNF-α were also observed in women with pre-eclampsia (Lewis et al., 2009), with concentrations as high as 200 pg/ml. In obese individuals, the plasma concentration of TNF-α released by adipose cells can be as large as 10 pg/ml (Rocha and Libby, 2009); and similarly high levels have been observed

in patients with severe trauma (Harting et al., 2008, Roumen et al., 1993 and Suter et al., 1992). These data are also summarized in Table. B1.

Indeed it is well known that high plasma levels of TNF-α are toxic. A series of clinical trials aimed at using TNF-α as an anticancer therapeutic molecule (Lejeune et al., 2006) identified a maximum tolerable dose after systemic administration of about 500-1000 ng/ml. The plasma levels summarized in Tab.1 are significantly smaller than the maximum tolerable dose. Nonetheless, most of the pathologies cited above and associated with abnormal circulating levels of TNF-α would eventually lead to vascular dysfunctions with failure of the major organs. Patients affected by rheumatoid arthritis are at increased risk of atherosclerosis and early death by heat failure (McKellar et al., 2009); vascular aberrations are clearly documented to be associated with tumor progression (Ferrari, 2010), and pre-eclampsia may lead to illness and death by systemic damage of the endothelium (Lewis et al., 2009).

Based on the above reasoning and the AFM characterization presented, it is then tempting to speculate that relatively low, non physiological concentrations of circulating TNF-α (<1-10 ng/ml, much smaller than the maximum tolerable dose) over a sufficiently long time (from months to years) could be responsible for a progressive systemic increase in vascular permeability, primarily through the paracellular pathway, with an alteration of the fluid-tissue homeostasis. Systemic vascular dysfunction could be the minimum common denominator for several apparently unrelated diseases, as rheumatoid arthritis, atherosclerosis, tumor progression and metastatisation, pre-eclampsia, obesity and trauma.

In conclusions, the AFM characterization performed, although limited to solely three cell lines (HUVEC, HCAEC and HPMEC), represents the first work to the authors' knowledge assessing the mechanical behavior of three different endothelial cells. The

analysis has revealed that (i) under physiological conditions, no significant difference exists in terms of apparent compressive modulus among the three vascular districts with a mean apparent elastic modulus $E = 3.30 \pm 0.35$ kPa; (ii) upon stimulation with TNF-α, the stiffness of the endothelial cells increases by about 50%, with no significant statistical difference among the three vascular districts, reaching a mean apparent elastic modulus $E = 5 \pm 0.5$ kPa; (iii) under physiological conditions, the viscoelastic losses in the pulmonary microvasculature are about 50% lower than in the other two districts considered, for which no significant statistical difference was observed; (iv) upon stimulation with TNF-α, the viscoelastic losses becomes statistically similar in all three vascular districts. These results provide additional information for unraveling the possible correlations between pro-inflammatory cytokines (as TNF-α) and systemic vascular dysfunction.

B.6 Effect of experimental condition

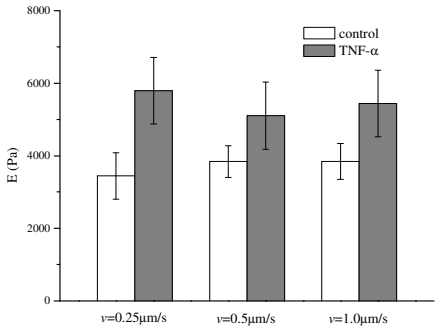

(a) HUVEC (F=0.5nN)

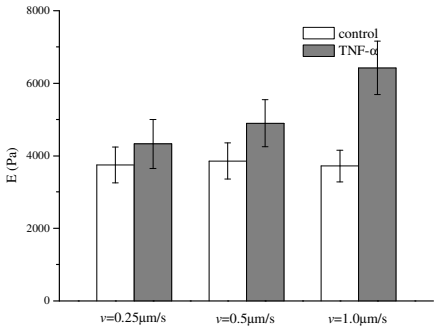

(b) HUVEC (F=1.0nN)

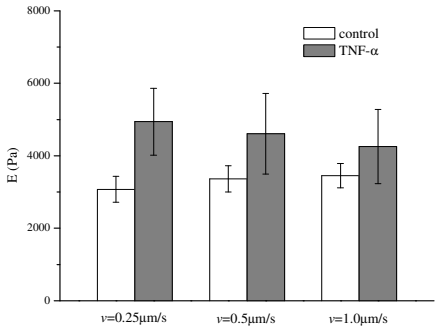

HCAEC (F=0.5nN)

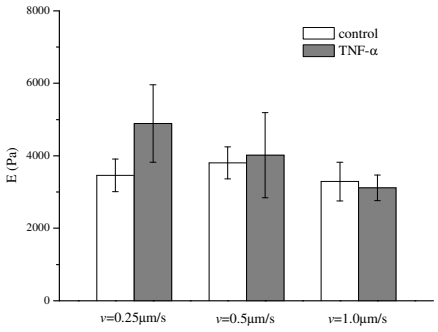

HCAEC (F=1.0nN)

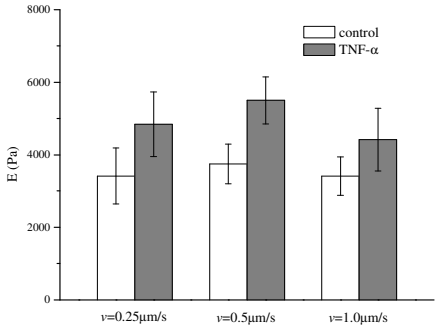

HPMEC (F=0.5nN)

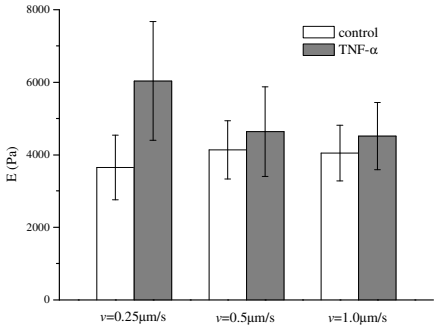

(c) HPMEC (F=1.0nN)

Fig. B6 Effect of the indenting velocity and force on the apparent elastic modulus. (F_{ind}=0.5 and 1.0 nN; v_{ind} = 0.25, 0.5, 1.0 μm/s)

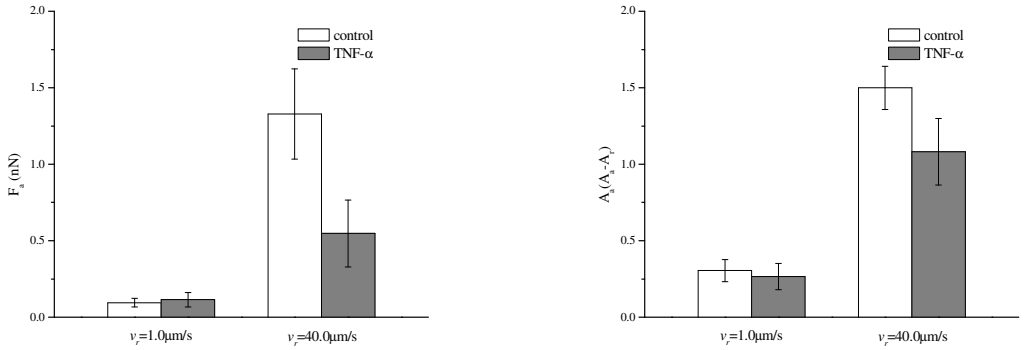

(a) HUVEC

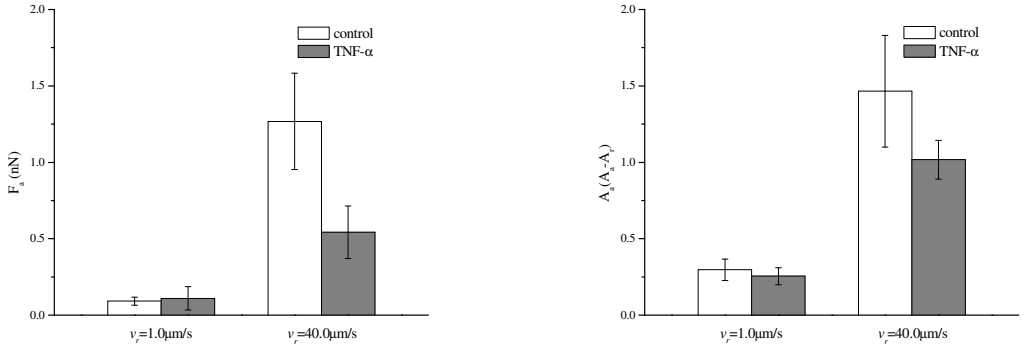

(b) HCAEC

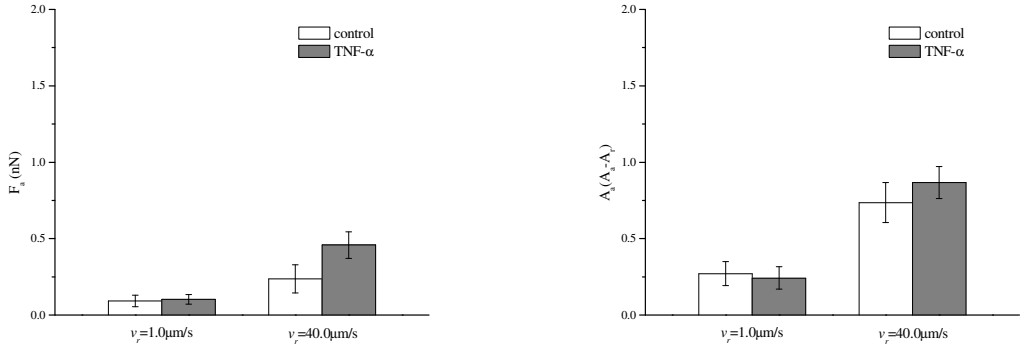

(c) HPMEC

Fig.B7 Effect of the retracting velocity (v_{ret}) on the force of adhesion.
(F_{ind}=5 nN; v_{ret}=1 μm/s and 40 μm/s)

References

Aberts B. et al. 2002, Molecular Biology of the Cell, 4th Ed., Garland Science.

Allen, T.M. 2002, Ligand-targeted therapeutics in anticancer therapy, Nat. Rev. Drug. Discov., 2. 750.

Alon R. Kassner P.D. Carr M.W. Finger E.B. Hemler M.E. Springer T.A. 1995, The integrin VLA-4 supports tethering and rolling in flow on VCAM-1, J Cell Biol., 128(6), 1243-53.

American cancer society, 2010, cancer fact & figures 2010

Arnold R.D. Mager D.E. Slack J.E. Straubinger R.M. 2005, Effect of repetitive administration of Doxorubicin-containing liposomes on plasma pharmacokinetics and drug biodistribution in a rat brain tumor model, Clin Cancer Res., 15(11), 8856-8865.

Ashby P.D. Chen L. and Lieber C.M. 2000, Probing intermolecular forces and potentials with magnetic feedback chemical force microscopy, J. Am. Chem. Soc., 122 (39), 9467-9472.

Attard P. 2007, Measurement and interpretation of elastic and viscoelastic properties with the atomic force microscope, J. Phys.: Condens. Matter., 19, 473201.

Bausch A.R. Möller W. and Sackmann E. 1999, Measurement of local viscoelasticity and forces in living cells by magnetic tweezers, Biophys J., 76, 573-9.

Bazilevs Y., Calo V.M. Hughes T.J.R. and Zhang Y. 2008, Isogeometric fluid-structure interaction: theory, algorithms and computations, Computational Mechanics 43 (1), 3-37.

Bazilevs Y. Calo V.M. Zhang Y. and Hughes T.J.R. 2006, Isogeometric fluid-structure interaction analysis with applications to arterial blood flow, Computational Mechanics, 38(4-5), 310–322.

Binnig G. Quate C. F. and Gerber C. 1986, Atomic Force Microscope, Phys. Rev. Lett., 56(9), 930-933.

Bozkurt B. Mann D.L. and Deswal A. 2009, Biomarkers of inflammation in heart failure, Heart Fail Rev.

Bretherton F.P. 1962, The motion of rigid particles in a shear flow at low Reynolds number, Journal of Fluid Mechanics, 14, 284-304.

Broday D. Fichman M. Shapiro M. and Gutfinger C. 1998, Motion of spheroidal particles in vertical shear flows, Phys. Fluids, 10(1), 86-100.

Butt H.J. and Jaschke M. 1995, Calculation of thermal noise in atomic force microscopy, Nanotechnology, 6, 1-7.

Calo V.M. Brasher N.F. Bazilevs Y. and Hughes T.J.R. 2008, Multiphysics model for blood flow and drug transport with application to patient-specific coronary artery flow, Computational Mechanics, 43 (1), 161-177.

Champion J.A. and Mitragotri S. 2006, Role of target geometry in phagocytosis, PNAS, 103(13), 4930-4934.

Champion J.A. and Katare Y.K. and Mitragotri S. 2007, Making polymeric micro- and nanoparticles of complex shapes, PNAS, 104(29), 11901-11904.

Charoenphol P. Huang R.B. and Eniola-Adefeso O. 2010, Potential role of size and hemodynamics in the efficacy of vascular-targeted spherical drug carriers, Biomaterials, 31(6), 1392-402.

Chen S. Alon R. Fuhlbrigge R.C. and Springer T.A. 1997, Rolling and transient tethering of leukocytes on antibodies reveal specializations of selectins, PNAS. 94(7), 3172-7.

Chiappini C, Tasciotti E, Fakhoury JR, Fine D, Pullan L, Wang YC, Fu L, Liu X, Ferrari M. 2010, Tailored porous silicon microparticles: fabrication and properties, Chemphyschem. 11(5), 1029-35.

Choi T. and Lee S. 2010, Holographic analysis of three-dimensional inertial migration of spherical particles in micro-scale pipe flow, Microfluidics and Nanofluidics, online first.

Cozens-Roberts C. Quinn J.A. and Lauffenburger D.A. 1990a, Receptor-mediated cell attachment and detachment kinetics 1. Probabilistic model and analysis, Biophys J., 58, 841-856.

Cozens-Roberts C. Quinn J.A. and Lauffenburger D.A. 1990b, Receptor-mediated cell attachment and detachment kinetics 2. Experimental model studies with the radial-flow detachment assay, Biophys J., 58, 107-125.

Danila D. Partha R. Elrod D.B. Lackey M. Casscells S.W. and Conyers J.L. 2009, Antibody-labeled liposomes for CT imaging of atherosclerotic plaques: in vitro investigation of an anti-ICAM antibody-labeled liposome containing iohexol for molecular imaging of atherosclerotic plaques via computed tomography. Tex Heart Inst J. 36(5), 393-403.

Danis V.A. Franic G.M. Rathjen D.A. Laurent R.M. and Brooks P.M. Circulating cytokine levels in patients with rheumatoid arthritis: results of a double blind trial with sulphasalazine. Ann Rheum Dis., 51(8), 946-50.

Decuzzi P. Gentile F. Granaldi A. Curcio A. Causa F. Indolfi C. Netti P. and Ferrari M. 2007, Flow chamber analysis of size effects in the adhesion of spherical particles, Int J Nanomedicine, 2(4), 689-696.

Decuzzi P. Godin B. Tanaka T. Lee S.Y. Chiappini C. Liu X. and Ferrari M. 2010, Size and shape effects in the biodistribution of intravascularly injected particles, J Control Release, 141(3), 320-7.

Decuzzi P. and Ferrari M. 2006, The adhesive strength of non-spherical particles mediated by specific interaction, Biomaterials, 27, 5307–5314.

Decuzzi P. and Ferrari M. 2008, Design maps for nanoparticles targeting the diseased microvasculature, Biomaterials, 29, 377-384.

Derin D. Soydinç H.O. Guney N. Tas F. Camlica H. Duranyildiz D. Yasasever V. Topuz E. 2008, Serum levels of apoptosis biomarkers, survivin and TNF-alpha in nonsmall cell lung cancer. Lung Cancer., 59(2), 240-5.

Feldman A.M. Combes A. Wagner D. Kadakomi T. Kubota T. Li Y.Y. McTiernan C. 2000, The role of tumor necrosis factor in the pathophysiology of heart failure. J. Am Coll Cardiol. 35(3), 537-44.

Ferrajoli A. Keating M.J. Manshouri T. Giles F.J. Dey A. Estrov Z. Koller C.A. Kurzrock R. Thomas D.A. Faderl S. Lerner S. O'Brien S. and Albitar M. 2002, The clinical significance of tumor necrosis factor-alpha plasma level in patients having chronic lymphocytic leukemia. Blood., 100(4), 1215-9.

Ferrari M. 2010, Frontiers in Cancer Nanomedicine: Directing Mass Transport through Biological Barriers. Trends in Biotechnology. in press.

Ferrari M. 2005, Cancer nanotechnology: opportunities and challenges, Nat Rev Cancer, 5, 161-171.

Ferrari M. 2008, Nanogeometry: Beyond Drug Delivery, Nat Nanotech., 3(3), 131-132.

Ferrari M. 2008, The mathematical engines of nanomedicine., Small, 4(1):20-5.

Fluent, Inc., 2003. FLUENT 6.1 User's Guide.

Fukumura D. Jain R.K. 2008, Imaging angiogenesis and the microenvironment. APMIS., 116(7-8), 695-715.

Gavze E. and Shapiro M. 1997, Particles in a shear flow near a solid wall: Effect of nonsphericity on forces and velocities, Int. J. Multiphase Flow, 23(1), 155-182

Gavze E. and Shapiro M. 1998, Motion of inertial spheroidal particles in a shear flow near a solid wall with special application to aerosol transport in microgravity, J. Fluid Mech., 371, 59-79

Gentile F. Curcio A. Indolfi C. Ferrari M. and Decuzzi P. 2008, The margination propensity of spherical particles for vascular targeting in the microcirculation., J Nanobiotechnology, 15, 6-9.

Gentile F. Chiappini C. Fine D. Bhavane R.C. Peluccio M.S. Ming-Cheng Cheng M. Liu X. Ferrari M. and Decuzzi P. 2008, The effect of shape on the margination

dynamics of non-neutrally buoyant particles in two-dimensional shear flows, J. of Biomech., 41(10), 2312-2318

Godin B. Driessen W.H. Proneth B. Lee S.Y. Srinivasan S. Rumbaut R. Arap W. Pasqualini R. Ferrari M. Decuzzi P. An Integrated Approach for the Rational Design of NanoVectors for Biomedical Imaging and Therapy, in press

Goldman A.J. Cox R.G. and Brenner H. 1967a, Slow viscous motion of a sphere parallel to a plane wall-I Motion through a quiescent fluid, Chem Eng Sci., 22, 637-651.

Goldman A.J. Cox R.G. and Brenner H. 1967b, Slow viscous motion of a sphere parallel to a plane wall-II Couette flow, Chem Eng Sci., 22, 653-660.

Gratton S.E. Ropp P.A. Pohlhaus P.D. Luft J.C. Madden V.J. Napier M.E. and DeSimone J.M. 2008, The effect of particle design on cellular internalization pathways, PNAS, 105, 11613.

Hajitou A. Trepel M. Lilley C.E. Soghomonyan S. Alauddin M.M. Marini F.C. 3rd. Restel B.H. Ozawa M.G. Moya C.A. Rangel R. Sun Y. Zaoui K. Schmidt M. von Kalle C. Weitzman M.D. Gelovani J.G. Pasqualini R. and Arap W. 2006, A hybrid vector for ligand-directed tumor targeting and molecular imaging, Cell, 125, 385.

Harting M.T. Jimenez F. Adams S.D. Mercer D.W. Cox C.S. 2008, Acute, regional inflammatory response after traumatic brain injury: Implications for cellular therapy, Surgery, 144(5), 803-13.

Hashizume H. Baluk P. Morikawa S. JMcLean.W. Thurston G. Roberge S. Jain R.K. and McDonald D.M. 2000, Openings between Defective Endothelial Cells Explain Tumor Vessel Leakiness. American Journal of Pathology, 156(4), 1363-1380.

Heron M., 2010, Deaths: Leading Causes for 2006, National Vital Statistics Reports, 58(14)

Hildebrandt H.A. Gossl M. Mannheima D. Versari D. Herrmann J. Spendlove D. Bajanowski T. Malyar N.M. Erbel R. Lermanb L.O. and Lermana A. 2008, Differential distribution of vasa vasorum in different vascular beds in humans, Atherosclerosis, 199, 47–54.

Hogg A.J. 1994, Inertial migration of a non-neutrally buoyant particle in a two-dimensional shear flow. J. Fluid Mech., 272, 285-318.

Iyer S. Gaikwad R.M. Subba-Rao V. Woodworth C.D. Sokolov I. 2009, Atomic force microscopy detects differences in the surface brush of normal and cancerous cells, Nat. Nanotech., 4, 389-393.

Jain R.K. 2001, Delivery of molecular and cellular medicine to solid tumors, Advanced Drug Delivery Reviews., 46, 149-151.

Jeffery G.B. 1922, The Motion of Ellipsoidal Particles Immersed in a Viscous Fluid, Proceedings of the Royal Society of London. Series A, 102(715), 161-179.

Joseph D.D. and Ocando D. 2002, Slip velocity and lift, J. Fluid Mech., 454, 263-286.

Kim J.A. Montagnani M. Koh K.K. and Quon M.J. 2006, Reciprocal relationships between insulin resistance and endothelial dysfunction: molecular and pathophysiological mechanisms. Circulation. 113(15), 1888-904.

Kim P. Puoris'haag M. Côté D. Lin CP. And Yun S.H. 2008, In vivo confocal and multiphoton microendoscopy, J Biomed Opt. 13(1), 010501.

Kim S. Keku T.O. Martin C. Galanko J. Woosley J.T. Schroeder J.C. Satia J.A. Halabi S. and Sandler R.S. 2008, Circulating levels of inflammatory cytokines and risk of colorectal adenomas, Cancer Res., 68(1), 323-8.

Komarova Y.A., Malik A.B. 2010, Regulation of Endothelial Permeability via Paracellular and Transcellular Transport Pathways. Annual Review of Physiology.,12, 463-493.

Komarova Y.A. Mehta D. Malik A.B. 2007, Dual regulation of endothelial junctional permeability. Sci STKE.

Laskowska M. Leszczyńska-Gorzelak B. Laskowska K. and Oleszczuk J. Evaluation of maternal and umbilical serum TNF-alpha levels in pre-eclamptic pregnancies in the intrauterine normal and growth-restricted fetus. J Matern Fetal Neonatal Med., 19(6), 347-51.

LaVan D.A. McGuire T. and Langer R. 2003, Small-scale systems for in vivo drug delivery, Nat. Biotech., 21(10), 1184-1191.

Lee S.Y. Ferrari M. and Decuzzi P. 2009, Design of Bio-Mimetic Particles with Enhanced Vascular Interaction, J. Biomech., 42(12), 1885-90.

Lee S.Y. Ferrari M. and Decuzzi P. 2009, Shaping nano-/micro-particles for enhanced vascular interaction in laminar flows, Nanotechnology.20(49), 495101.

Lejeune F.J. Liénard D. Matter M. and Rüegg C. 2006, Efficiency of recombinant human TNF in human cancer therapy. Cancer Immun., 22, 6.

Levy-Nissenbaum E. Radovic-Moreno A.F. Wang A.Z. Langer R. and Farokhzad O.C. 2008, Nanotechnology and aptamers: applications in drug delivery. Trends Biotechnol., 26, 442-449.

Lewis D.F. Canzoneri B.J. Wang Y. 2009, Maternal Circulating TNF-α Levels are Highly Correlated with IL-10 Levels, but not IL-6 and IL-8 Levels, in Women with Pre-Eclampsia. American Journal of Reproductive Immunology, 62, 269 – 274.

Li R. Wu R. Zhao L. Wu M. Yang L. and Zou H. 2010, P-glycoprotein antibody functionalized carbon nanotube overcomes the multidrug resistance of human leukemia cells, ACS Nano, 4(3), 1399-408.

Libby P. Aikawa M. Jain M.K. 2006, Vascular endothelium and atherosclerosis, Handb. Exp. Pharmacol. 176, 285–306.

Mahaffy R.E. Park S. Gerde E. Käs J. and Shih C.K. 2004, Quantitative analysis of the viscoelastic properties of thin regions of fibroblasts using atomic force microscopy, Biophys J., 86(3), 1777-93.

Mahmood M. Karmakar A. Fejleh A. Mocan T. Iancu C. Mocan L. Iancu D.T. Xu Y. Dervishi E. Li Z. Biris A.R. Agarwal R. Ali N. Galanzha E.I. Biris A.S. and Zharov V.P. Synergistic enhancement of cancer therapy using a combination of carbon nanotubes and anti-tumor drug, Nanomedicine (Lond), 8, 883-93.

Matas J.P. Morris J.F. and Guazzelli E. 2004, Inertial migration of rigid spherical particles in Poiseuille flow, J. Fluid Mech., 515, 171–195.

Mathur A.B. Collinsworth A.M. Reichert W.M. Kraus W.E. and Truskey G.A. 2001, Endothelial, cardiac muscle and skeletal muscle exhibit different viscous and elastic properties as determined by atomic force microscopy, J Biomech., 34(12), 1545-53.

McInnes I.B. and Schett G. 2007, Cytokines in the pathogenesis of rheumatoid arthritis, Nat Rev Immunol. 7(6), 429-42.

McKellar G.E. McCarey D.W. Sattar N. and McInnes I.B. 2009, Role for TNF in atherosclerosis. Lessons from autoimmune disease. Nat Rev Cardiol., 6(6), 410-7.

McLaughlin, J.B. 1991, Inertial migration of a small sphere in linear shear flows. J. Fluid Mech., 224, 261-274.

Michalaki V. Syrigos K. Charles P. and Waxman J. 2004, Serum levels of IL-6 and TNF-alpha correlate with clinicopathological features and patient survival in patients with prostate cancer, Br J Cancer, 90(12), 2312-6.

Michiels C. 2003, Endothelial cell functions. J Cell Physiol. 196(3), 430-43.

Misra S. Woodrum D.A. Homburger J. Elkouri S. Mandrekar J.N. Barocas V. Glockner J.F. Rajan D.K. and Mukhopadhyay D. 2006, Assessment of Wall Shear Stress Changes in Arteries and Veins of Arteriovenous Polytetrafluoroethylene Grafts Using Magnetic Resonance Imaging, Cardiovasc Intervent Radiol, 29, 624–629.

Mitragotri S. and Lahann J. 2009, Physical approaches to biomaterial design, Nat Mater,. 8(1), 15-23.

Netti P.A. Berk D.A. Swartz M.A. Grodzinsky A.J. and Jain R.K. 2000, Role of Extracellular Matrix Assembly in Interstitial Transport in Solid Tumors, Cancer Research. 60, 2497- 2503.

Old L.J. 1985, Tumor necrosis factor (TNF), Science, 230(4726), 630-2.

Patil V.R.S. Campbell C.J. Yun Y.H. Slack S.M. and Goetz D.J. 2001, Particle diameter influences adhesion under flow, Biophys J., 80, 1733-1743

Pennica D. Nedwin G.E. Hayflick J.S. Seeburg P.H. Derynck R. Palladino M.A. Kohr W.J. Aggarwal B.B. and Goeddel D.V. 1984, Human tumour necrosis factor: precursor structure, expression and homology to lymphotoxin, Nature, 312(5996), 724-9.

Pober J.S. Sessa W.C. 2007, Evolving functions of endothelial cells in inflammation, Nat. Rev. Immunol., 7, 803–15.

Prabhu S. 2004, Computational modeling in stent-based drug delivery, Business Briefing: Medical Device Manufacturing & Technology.

Reneman R.S. and Hoeks A.P.G. 2008, Wall shear stress as measured in vivo: consequences for the design of the arterial system, Med Biol Eng Comput, 46(5), 499-507.

Rocha V.Z. and Libby P. Obesity, inflammation, and atherosclerosis, Nat Rev Cardiol., 6(6), 399-409.

Rolland J.P. Maynor B.W. Maynor L.E. Exner A.E. Denison G.M. and DeSimone J.M. 2005, Direct fabrication and harvesting of monodisperse, shape-specific nanobiomaterials, J. Am. Chem. Soc., 127, 10096

Roumen R.M. Hendriks T. van der Ven-Jongekrijg J. Nieuwenhuijzen G.A. Sauerwein R.W. van der Meer J.W. and Goris R.J. Cytokine patterns in patients after major vascular surgery, hemorrhagic shock, and severe blunt trauma. Relation with subsequent adult respiratory distress syndrome and multiple organ failure, Ann Surg, 218(6), 769-76.

Sakamoto J. Annapragada A. Decuzzi P, and Ferrari M. 2007, Antibiological barrier nanovector technology for cancer applications, Expert Opin Drug Deliv., 4(4), 359-69

Sato M. Theret D.P. Wheeler L.T. Ohshima N. and Nerem R.M. 1990, Application of the micropipette technique to the measurement of cultured porcine aortic endothelial cell viscoelastic properties, J Biomech Eng., 112(3), 263-8.

Serge G. and Silberberg A. 1961, Radial Particle Displacements in Poiseuille. Flow of Suspensions, Nature, 189(4760), 209-210.

Shigley J. 1983, Mechanical engineering design, New York: McGraw-Hill.

Skoog T. Dichtl W. Boquist S. Skoglund-Andersson C. Karpe F. Tang R. Bond M.G. de Faire U. Nilsson J. Eriksson P. and Hamsten A. 2002, Plasma tumour necrosis factor-alpha and early carotid atherosclerosis in healthy middle-aged men. Eur Heart J. 23(5), 376-83.

Springer T.A. 1990, Adhesion receptors of the immune system, Nature 346, 425–434.

Stroeva P.V. Hoskinsb P.R. and Eassona W.J. 2007, Distribution of wall shear rate throughout the arterial tree: A case study, Atherosclerosis, 191, 276–280

Suter P.M. Suter S. Giradin E. Roux-Lombard P. Grau G.E. and Dayer J.M. 1992, High bronchoalveolar levels of tumour necrosis factor and its inhibitors, interleukin-1, interferon and elastase, in patients with adult respiratory distress syndrome after trauma, shock or sepsis, Am Rev Resp Dis., 1451016–1022.

Talar-Wojnarowska R. Gasiorowska A. Smolarz B. Romanowicz-Makowska H. Kulig A. and Malecka-Panas E. 2009, Tumor necrosis factor alpha and interferon gamma genes polymorphisms and serum levels in pancreatic adenocarcinoma, Neoplasma, 56(1), 56-62.

Tan L.R. Waxman K. Scannell G. Ioli G. and Granger G.A. 1993, Trauma Causes Early Release of Soluble Receptors for Tumor Necrosis Factor, The Journal of Trauma., 34(5), 634-638.

Tasciotti, E. Liu X. Bhavane R. Plant K. Leonard A.D. Price B.K. Cheng M.M. Decuzzi P. Tour J.M. Robertson F. and Ferrari M. 2008, Mesoporous silicon particles as a multistage delivery system for imaging and therapeutic applications, Nat Nanotech, 3, 151-157.

Taylor C.A. Cheng C.P. Espinosa L.A. Tang B.T. Parker D. and Herfkens R.J. 2002, In Vivo Quantification of Blood Flow and Wall Shear Stress in the Human Abdominal Aorta During Lower Limb Exercise,Annals of Biomedical Engineering, 30, 402–408.

Tesarová P. Kvasnicka J. Umlaufová A. Homolková H. Jirsa M. and Tesar V. 2000, Soluble TNF and IL-2 receptors in patients with breast cancer, Med Sci Monit., 6(4), 661-7.

Tokuda S. Miyazaki H. Nakajima K. Yamada T. Marunaka Y. 2009, Hydrostatic pressure regulates tight junctions, actin cytoskeleton and transcellular ion transport, Biochem Biophys Res Commun. 390(4), 1315-21.

Touhami A. Nysten B. Dufrene Y.F. 2003, Nanoscale mapping of the elasticity of microbial cells by atomic force microscopy, Langmuir, 19, 4539-4543.

Wei M.T. Zaorski A. Yalcin H.C. Wang J. Ghadiali S.N. Chiou A. Ou-Yang H.D. 2008, A comparative study of living cell micromechanical properties by oscillatory optical tweezers, Opt Express., 16(12), 8594-603.

Wojcikiewcz E.P. Zhang X. and Moy V. 2003, Force and compliance measurement on living cells using atomic force microscopy (AFM), Biol. Proced. 6(1), 1-9.

Worrall N.K. Chang K. LeJeune W.S. Misko T.P. Sullivan P.M. Ferguson T.B. Jr, and Williamson J.R. 1997, TNF-alpha causes reversible in vivo systemic vascular

barrier dysfunction via NO-dependent and -independent mechanisms, Am J Physiol. 273, H2565-74.

Wu S.W. and Aird W.C. 2005, Thrombin, TNF-alpha, and LPS exert overlapping but nonidentical effects on gene expression in endothelial cells and vascular smooth muscle cells, Am. J. Physiol. Heart Circ. Physiol., 289, H873–H885

Yang B.H. Wang J. Joseph D.D. Hu H.H. Pan T.W. and Glowinski R. 2005, Migration of a sphere in tube flow, J. Fluid Mech., 540, 109–131

Vita

Sei-Young Lee was born in Seoul, Korea, in July 1975, the son of Haksang Lee and Jisook Kim. After completing his work at Banpo High School, Seoul, Korea, in February 1994, he entered Yonsei University in Seoul, Korea. He received the degree of Bachelor of Science and Master of Science from Yonsei University in February 1999 and February 2001, respectively, under supervision of Dr. H.H.Cho. During this period, he studied convective heat transfer and fluid mechanics for the application of gas turbine blade cooling system. After graduation, he served for Republic of Korea, Navy as engineering officer from 2002 to 2005. In August 2005, he entered the doctoral program in Mechanical Engineering Department at The University of Texas at Austin. During his study, he was under supervision of Dr. M. Ferrari.

Permanent address: 221-301 Humansia APT, Nanhyang-Dong, Kwanak-Gu, Seoul, Korea.

e-mail address: lee_seiyoung@yahoo.co.kr

This dissertation was typed by Lee, Sei Young.